Development of a Precision Hot Embossing Machine with In-Process Sensing

by

Maia R. Bageant

B.S., Massachusetts Institute of Technology (2011)

Submitted to the Department of Mechanical Engineering
in partial fulfillment of the requirements for the degree of

Master of Science in Mechanical Engineering

at the

MASSACHUSETTS INSTITUTE OF TECHNOLOGY

June 2013

Author .....
Department of Mechanical Engineering
June 3, 2013

Certified by .....
David Hardt
Ralph E. and Eloise F. Cross Professor of Mechanical Engineering
Thesis Supervisor

Accepted by .....
David Hardt
Ralph E. and Eloise F. Cross Professor of Mechanical Engineering
Graduate Officer

Development of a Precision Hot Embossing Machine with In-Process Sensing

by

Maia R. Bageant

Submitted to the Department of Mechanical Engineering
on June 3, 2013, in partial fulfillment of the
requirements for the degree of
Master of Science in Mechanical Engineering

Abstract

Microfluidic technologies show great promise in simplifying and speeding biological, medical, and fluidic tasks, but transitioning these technologies from a laboratory environment to a production environment has proven difficult. This work focuses on hot embossing as a process suitable to produce these devices. In this work, a precision micro-embossing machine capable of maintaining precise setpoints in force and temperature input as well as displaying highly linear, repeatable motion and force application is developed and characterized. Additionally, this equipment is then outfitted with additional sensors that allow for three measurements relevant to process physics and product quality to be captured: initial substrate geometry; substrate bulk deformation; and glass transition temperature of the material. These measurements can be captured in-process without modifying the production cycle. The end goal is to incorporate this precision micro-embossing machine into a micro-factory cell and to implement closed-loop cycle-to-cycle process control.

Thesis Supervisor: David Hardt
Title: Ralph E. and Eloise F. Cross Professor of Mechanical Engineering

Acknowledgments

The work completed in this thesis could never have happened without the support of many.

I would like to thank my research colleagues; Melinda Hale, Joseph Petrzelka, and Caitlin Reyda were tremendous sources of support and feedback in the early development of the project, and the other newer members of the Hardt Lab provided a helping hand upon their later arrival. In addition, undergraduate researcher Spencer Wilson provided much appreciated support during fabrication of the machine.

I would also like to acknowledge my family, who always supported my work, no matter how obscure my end purpose seemed, and who imparted in me from a young age the curiosity and drive to pursue these studies. My friends at home and across the country also helped keep my head up and my nose to the grindstone, and I must thank them too.

And of course I must acknowledge the terrific help and guidance from my advisor, Professor Hardt. From the very beginning of this project he has guided its course with an expansive understanding of its context and meaning. But he has also never feared to dive into the finer details of the work and metaphorically dirty his hands beside his students. Without his patience, dedication, and wisdom this project would never have succeeded.

Finally, this research is part of a 10-year program sponsored by the Singapore-MIT Alliance Manufacturing Systems and Technology Programme, and without their financial and academic generosity this work would not have been possible.

Contents

List of Figures

List of Tables

Chapter 1

Introduction

1.1 Microfluidic Devices

Microfluidic technologies are a recent development that show great promise in simplifying and facilitating various fluidic tasks such as biological assays, polymerase chain reaction (PCR), cell sorting, and more. As detailed by George Whitesides [1], "[i]t is the science and technology of systems that process or manipulate small (10^{-9} to 10^{-18} litres) amounts of fluids, using channels with dimensions of tens to hundreds of micrometers." An example of one of these devices is shown in Figure 1-1, in which complex networks of channels used to route fluid are demonstrated. At this scale, individual cells and even large molecules can be manipulated using droplet mechanics and electromagnetic fields. Very small quantities of potentially expensive reactants are required to complete procedures with volumes of this order of magnitude. Additionally, the size and cost of a microfluidic device is intentionally minimal, circumventing the expense and bulk of full lab test setups. In sum, these devices are an attractive product, in particular for the medical field, and an area of active research development.

Typically, laboratory-scale fabrication of microfluidic device designs is done by casting a two-part soft polymer, polydimethyl siloxane (PDMS), onto a featured surface, typically patterned using conventional photolithography techniques. PDMS is capable of conforming to even nanoscale features, making it ideal for replicating a

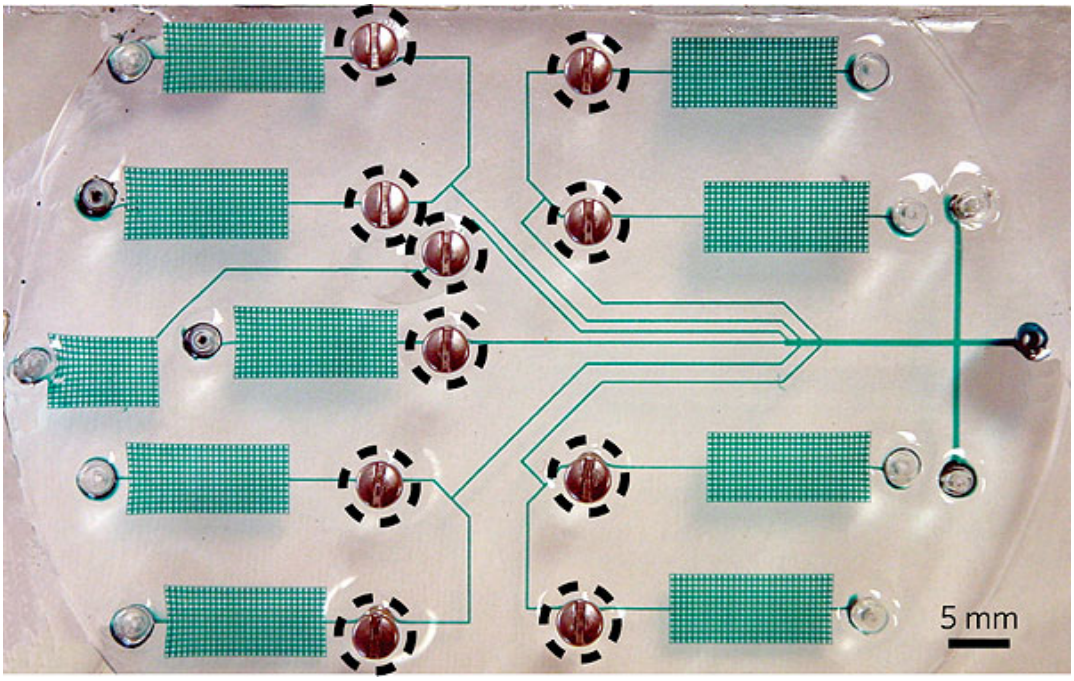

Figure 1-1: Example of a Microfluidic Device: This diagnostic device performs sandwich immunoassays. The tiny screws act as manual valves, and the assays are done in the complex networks of channels. [1]

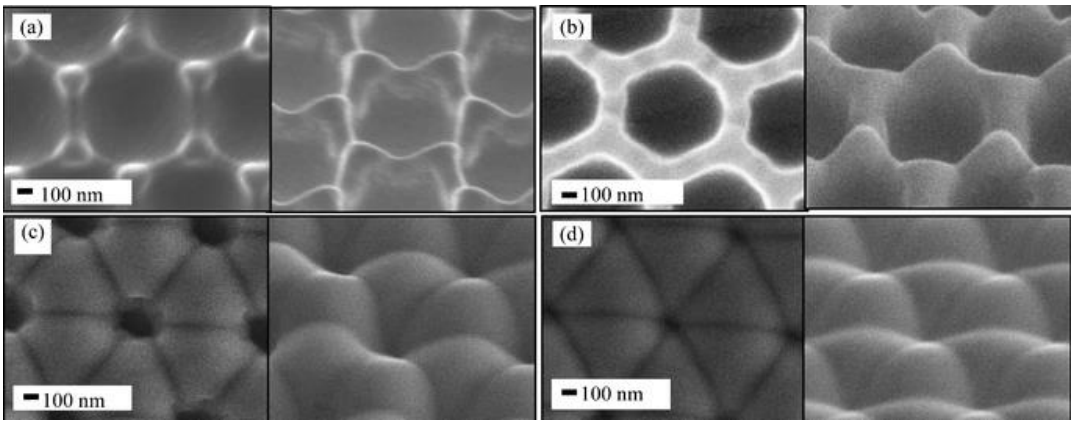

Figure 1-2: Nanoscale features in PDMS: This figure shows images of molds created by casting PDMS onto self-assembled polystyrene structures, and then again casting PDMS into the resulting negative. Note the feature replication down to the scale of 100nm. [17]

finely textured master; in Figure 1-2, an example of the level of fidelity of replication is shown. The PDMS, which now forms three of the four walls of the enclosed channel, is then often plasma treated to change its surface energy and bonded to a glass backplane, thus sealing and completing a device [2].

However, PDMS has several disadvantages as an engineering material; though temperature resistant, it tends to become brittle with age or long-term exposure to heat. It has poor dimensional stability and has a tendency to absorb certain solvents such as hexanes as well as small biologically interesting molecules such as estrogen [3]. And finally, the two-part casting process does not easily lend itself to automated mass manufacture. To this end, investigating alternative materials and means of fabricating these devices from them is a topic of interest.

The next logical step for high-volume production of these devices, then, is to move to hard thermoplastics conventionally used for mass production of low-cost components and products, such as cyclic oleifin polymers (COPs) or polymethylmethacrylate (PMMA). However, the best method to use these materials to produce microfluidic devices is still under investigation.

1.2 Fabrication of Microfluidic Devices

There exist several methods currently practiced in the state of the art to fabricate microfluidic devices out of hard polymers. The option to utilize serial material removal processes such as directly micromachining or laser engraving channels into substrates is one possibility. In micromachining, a tool tip is used to remove material by shearing it away. Diamond turning is capable of producing molds with features sizes of 10μm and surface roughnesses of 1μm but is not well suited for smaller geometries. Additionally, for repeated geometries over a large area, micromachining is a very slow process [2].

Direct laser ablation is another choice, in which a focused laser beam causes the polymer to selectively vaporize in the area of focus. Using photolithography techniques, micro and nanopatterns with very high resolution can be obtained. However,

melting occurs in the areas bordering the resulting cavity, and many polymers suitable for microfluidic device production are not suitable for laser ablation. In addition, this process is low-throughput, as it is also a serial process [2].

Another possibility is to use injection molding to create devices. The hard thermoplastics used in injection molding are preferable for mass manufacturing due to their dimensional stability, temperature resistance, and low cost. There are some difficulties associated with using injection molding to replicate such small features, however; because of their microscale size, if the mold temperature is lower than the melting point of the polymer, the polymer can thicken or solidify and fail to fill microscale features in the mold, especially those of high aspect ratios. By using heated molds and careful process optimization, injection molding can result in acceptable levels of feature replication on the microscale, which is of the greatest interest to microfluidic device developers [4]. However, the tooling and production capital costs associated with injection molding capability, in particular with molds containing microscale features, is high compared to other processes. This means that for a very large quantity of devices, injection molding is economical; however, it is an undesirable option for the purpose of producing smaller volumes of devices, or for situations in which the microfluidic device design may be revised (thus requiring a new mold insert, or possibly an entirely new mold, to be fabricated) [5].

Nanoimprint lithography is another technique currently proposed. In this technique, a patterned mold is first pressed into a resist on a backing substrate to impart micro- or nano-structures; the resist is developed; and then a material removal technique such as reactive ion etching is used to remove any residual resist. Success has been reported in utilizing this technique to pattern large areas, but it has yet to be demonstrated as a manufacturing scale technique [2].

Ultraviolet imprinting is another available technique. In this technique, a fluid polymer is allowed to flow into the shape of a mold, and then is exposed to ultraviolet light to harden and cure it. UV imprinting requires a mold transparent to ultraviolet light, such as one made of quartz or certain polymers [6]. However, the mechanical and manufacturing demands of nanoimprint lithography can be similar

to that of conventional lithography, making it a relatively expensive process for the production of what are intended to be low-cost devices [7].

1.3 Hot Embossing

Hot embossing is a process that addresses the high-flexibility, low-cost, medium-volume niche. It is a parallel process like injection molding; however, the equipment and tooling demands are simpler and lower-cost. The cycle time required to produce one part is generally longer due to the need to individually heat each blank substrate, but embossing results in a similar level of fidelity in feature replication as injection molding, with the potential to mold higher aspect ratio features [4]. Plus, because the polymer is only superficially flowed into the mold microstructures, only small residual stresses are produced in the part, making hot embossing both less damaging to molding tools, capable of forming more complex or delicate structures, and suitable for producing optical components such as waveguides [5]. Additionally, producing stamping tools is on par with producing inserts for plastic injection molding, and setup time to exchange tools and adjust machine parameters is shorter, as embossing machines are simple and require few modifications [5].

Thus, the hot embossing process provides a fabrication technique addressing the needs of devices designers who might need to rapidly iterate designs as they port a soft-polymer device to a hard-polymer form; of researchers who might want to produce a limited but consequential number of devices for a large-scale study; or of producers looking for options requiring low capital investment [5]. But, hot embossing is not limited to these environments; the process capabilities are similar or beyond those of injection molding, and the capital equipment required for production is lower cost and suitable for parallelization: hot embossing is a completely feasible process to be employed on a mass production scale. However, perhaps due to a widespread lack of understanding of the process physics and especially of commercially equipment suitable for industrial microembossing, and the process remains a path less frequently tread for industrial production of microfluidic devices. The work completed in this re-

search project seeks to demonstrate that the hot embossing process is in fact an equal or superior industrial scale process to injection molding for certain device designs.

In the hot embossing process, a hard, amorphous polymer is heated until it passes its glass transition temperature, becoming soft and malleable. A patterned tool is then pressed into the polymer, creating regions of high pressure that induce flow of the polymer. This flow is dependent on the viscoplastic properties of the polymer (determined by the material and the temperature), the induced pressures, and the rate at which the stamp is driven into the substrate. After sufficient formation has occurred, the polymer may then be cooled while still engaging the tool, freezing its molecular structure in place, as shown in Figure 1-3. Finally, the tool is withdrawn from the imprinted polymer in a step called demolding. The physical process of hot embossing is further detailed in Chapter 2.

1.4 Equipment Needs and State of the Art

Traditionally, hot embossing had not been applied to precision applications such as the fabrication of microfluidic devices. There exist, then, few available off-the-shelf solutions intended to perform precision hot embossing.

Industrial hot embossing machines do exist, but are primarily targeted at creating macroscale embossed patterns in various materials, including leather, foils, and polymers [24]. But, these machine shop floor products are not intended for use in creating products with microscale precision.

Laminating machines are another tool co-opted for use in hot embossing. Laminating machines essentially apply heat and pressure to flat materials passed between two rollers. In work performed by Jeon and Kamm, successful embossing was performed using a laminator—but required an entire hour to be completed [8].

More specialized solutions from industry are available, such as those from EV Group. The EVG 750 consists of a fully automated system with cassettes for unformed substrates, temperature capabilities up to 220°C and the ability to emboss areas of 20cm^2 by applying up to 360kN of force [7]. A lower-end model, the semi-automated

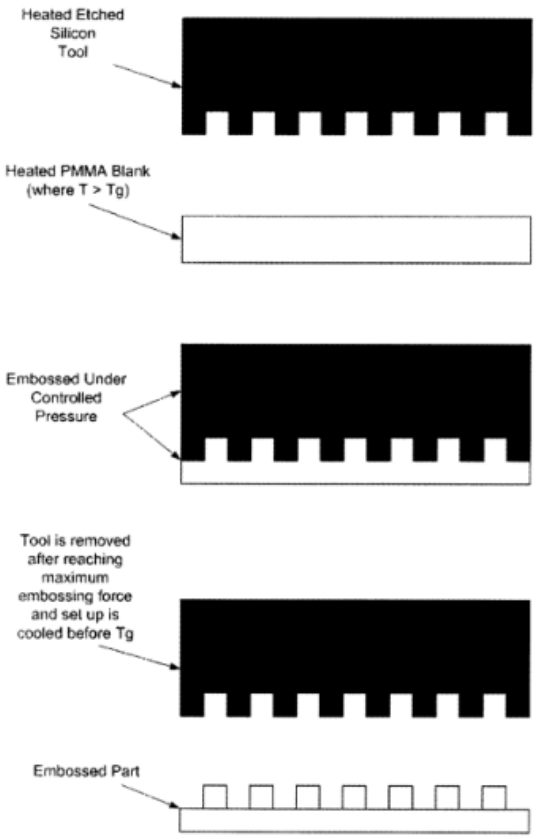

Figure 1-3: Schematic of the Hot Embossing Process: In step 1, a blank substrate is pressed against a rigid patterned tool; in step 2, the substrate flows and conforms to the tool; and in step 3, the substrate is removed from the tool, retaining permanent features in the negative of the tool [20].

EVG 520HE, features a maximum force application of some 60kN and is capable of embossing an area 20cm on the diagonal. It does also feature an ultraviolet light source and a vacuum chamber, as well as a loading and unloading mechanism [7]. Both devices outperform more primitive presses, demonstrating the levels of precision and control in forming that are required to produce high quality microfluidic devices [25]. To purchase and install such equipment at the EVG520HE is on the order of some $200,000, a significant investment [26].

Thus, though low-cost but imprecise options and high-cost but high-quality options are available, no existing solution has yet offered a low-cost, "right size" option with sufficient precision for microscale polymer embossing. This serves as a barrier for the adoption of hot embossing both on the medium-volume scale by groups such as microfluidics research labs or startup companies developing their first devices and on the industrial scale in which parallel production could be used to create high throughput.

1.5 Project Motivation

To this end, this research project set out to develop the application of the hot embossing process to polymer microscale fabrication in the context of production-scale manufacturing. In order to accomplish this goal, there were numerous considerations that needed to be addressed.

First, there was the lack of existing precision fabrication equipment targeted to this purpose, making the study of the embossing process difficult. Over the course of this research effort, several generations of equipment had been developed by researchers preceding the author. The first two generations were focused on developing process knowledge in an experimental fashion rather than on implementing the process in a manufacturing environment. Though all input parameters could be well controlled, the cycle time to produce a single part was on the order of 30 minutes [18]. Once process knowledge was established, the next generations of hardware could focus on using that knowledge to design precision fabrication equipment with a focus on low

cost, low cycle time, and an appropriate level of precision and parameter control [13].

It was determined that in order to properly study hot embossing as a manufacturing process, first a suitable testbed system would need to be developed [27]. The testbed, deemed the "micro-factory," or "μFac," would consist of several completely automated modules that could be scheduled to produce and measure microfluidic devices. The automated modules, combined with an commercial pick-and-place robot to perform materials handling, would remove operator-induced variation from the equation. And, if machine variation could be reduced to a minimum, the testbed would then serve as a suitable platform to investigate natural process variation, produce statistical models of the hot embossing process, and implement closed-loop cycle-to-cycle control of the process based on finished product function.

The contributions of this thesis are then aimed toward accomplishing this goal. The first contribution is to develop automated precision embossing equipment that reduces machine variation to a minimum, building on lessons learned from previous generations of equipment. The second contribution is to utilize this equipment to make relevant and interesting measurements of process phenomena that are indicators of quality as well as physical confirmations of process physics models.

Chapter 2

Process Physics of Hot Embossing

2.1 The Hot Embossing Process

The hot embossing process in one in which permanent plastic deformation is imparted to a polymer substrate using a heated featured stamp. In the process used in this research, the substrate is first heated above its glass transition, facilitating plastic flow at low levels of applied pressure. This heating is performed while lightly pressing the tool into the substrate in order to maintain contact and increase the efficiency of the heating process. Once the substrate has reached its forming temperature, a higher force is applied, creating pressures sufficient for viscoplastic flow of the substrate. The substrate flows around and conforms to rigid features on a tool, replicating them on the micro- and even nano-scale, down to 25nm [28]. Once sufficient feature replication has been accomplished, the substrate is cooled to below its glass transition temperature, solidifying its molecular structure and returning its mechanical properties to glassy. Finally, the substrate is demolded from the tool, and features are permanently formed into the surface of the substrate. This process is demonstrated in Figure 2-1 using the force and temperature profiles undergone by the substrate.

This process typically completes three walls of the four-walled channel. To finish the device, a roof must also be added. For the purposes of this research, it was found that biocompatible pressure adhesive tape manufactured by Tesa Tape Inc. was sufficient to provide a fourth wall. After forming is complete, tape is applied

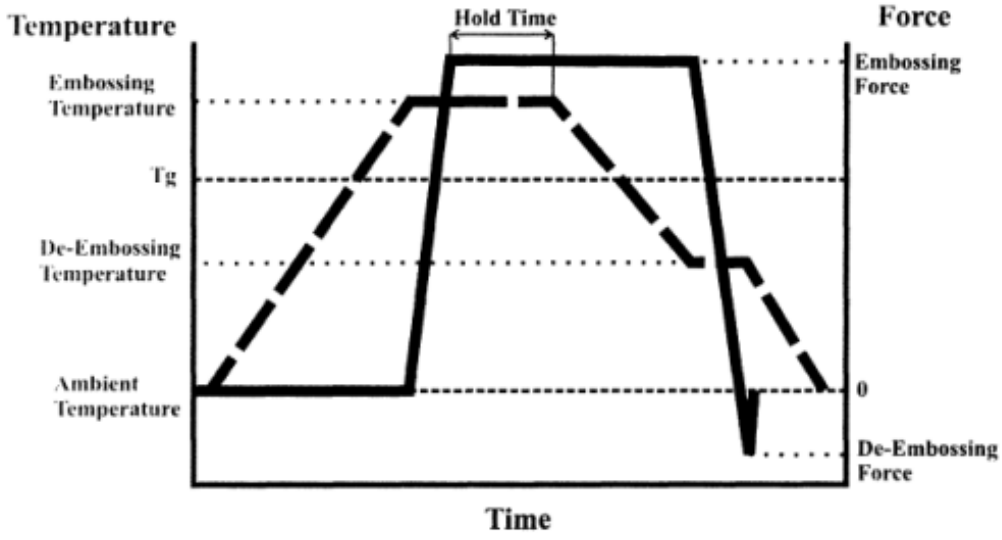

Figure 2-1: Ideal Forming Cycle for Hot Embossing: This diagram indicates typical levels of force and temperature (the selected input parameters) during a forming cycle for PMMA substrates [18].

using a compliant roller, and trimmed using an automated device[1]. The microfluidic device is then complete and ready for quality inspection, testing, and use.

The material that was the focus of this experimentation is polymethylmethacrylate (PMMA), a brittle, glassy polymer with high optical clarity. PMMA has a typical glass transition temperature of approximately 105°C [10], but this can vary from 85°C to 165°C depending on its the specific molecular composition [29]. At this temperature, its mechanical properties suddenly transform, and it changes from being a primarily elastic material to what is better described as an elastic-viscoplastic material; and then, as it reaches its melting temperature of approximately 250°C [9], it becomes a viscous liquid.

The embossing process takes place in the elastic-viscoplastic regime between the glass transition and melting temperature. Figure 2-2 shows experimental compression data in this region; a large amount of permanent deformation with low, nearly-constant levels of stress is apparent. For amorphous, glassy polymers, as the tem-

[1]The work to develop the taping process, including the development of the automated tape application and trimming device, as well as work to develop an automatic testing device, is currently being developed by Caitlin Reyda, and is scheduled to be completed by September 2013.

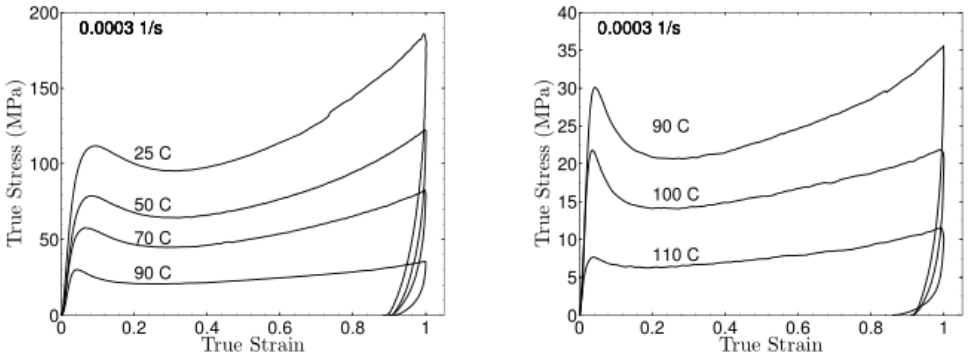

Figure 2-2: Experimental Compression Data for PMMA at Various Temperatures: In this experimental data, the dramatic change in flow stress as the temperature is increased from ambient to above glass transition (110°C) is clear. The 110°C curve displays remarkably plastic behavior, showing very little increase in stress with large strains. This particular test was performed at a fixed strain rate, but the behavior is also rate dependent [12].

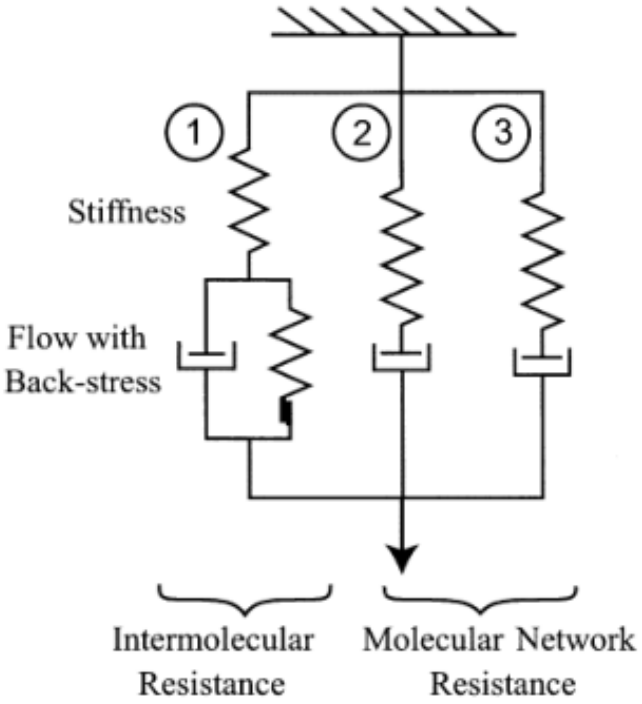

Figure 2-3: Mechanical Elements Model of PMMA: A mechanical elements model representing the 3 micromechanisms that control the material properties of amorophous polymers such as PMMA. Each micromechanism is numbered for referencing in the text [12].

perature increases, their molecules experience greater mobility and ability to twist and rotate, cross-linking between polymer chains weakens, and the shear modulus decreases. At the glass transition temperature, this change becomes suddenly and drastically accentuated, as shown in by the change in the shape of the curves in Figure 2-2. At this point the material can be considered elastic-perfectly viscoplastic, and its behavior can be modeled using the mechanical elements shown in Figure 2-3.

This model is intended to cover the behavior of a polymer throughout the temperature range from below its glass transition to above it. To accomplish this, the contribution of each component varies with the temperature regime. The first micromechanism indicated in the diagram is indicated with numeral 1. A nonlinear spring models the elastic resistance to molecular bond stretching; the dashpot models thermally-activated plastic flow due to polymer deformation mechanisms such as molecular chain rotation and slippage between cross-linkage locations; and the nonlinear spring in parallel with the dashpot models an energy storage property generated by any elastic instabilities caused by viscoplastic flow. The second and third mechanisms, denoted by numerals 2 and 3, also consist of nonlinear springs representing energy stored in stretching molecular chains between cross-link sites. The dashpots again model thermally-activated plastic flow and slippage between cross-link sites. These mechanisms are duplicated to facilitate modeling complex observed behavior [12]. Above glass transition temperature, mechanism 2 has a negligible contribution to material behavior, and mechanisms 1 and 3 control the material properties. The combined effects of these two micromechanisms appear as an elastic curve that transforms into nearly linear creep over large strains, with a small amount of springback during unloading, as shown in Figure 2-4 [12].

The practical application of this understanding is essentially that under the correct conditions, large amounts of plastic flow can be induced in the polymer. During the forming stage of the embossing process, then, a constant high-stress stress state is induced, forcing creep that results in permanent plastic deformation and flow outward on unconstrained surfaces, including into the tool cavities. This flow is dependent on the strain rate (as modeled by the dashpots), the induced stress, and the temperature

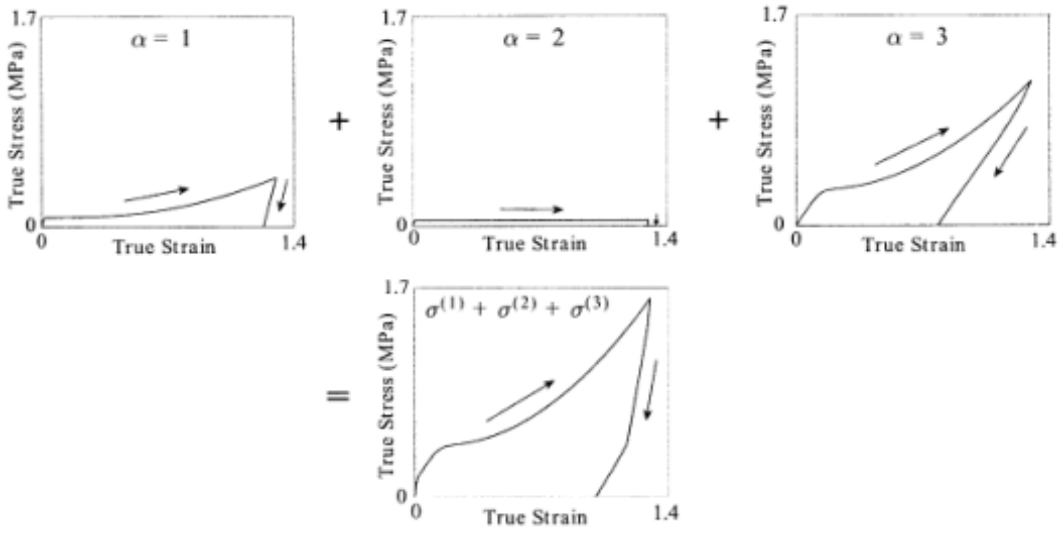

Figure 2-4: Stress-Strain Contributions of Individual PMMA Micromechanisms: The contributions of micromechanisms 1 through 3 for temperatures above the glass transition temperature show that both mechanisms 1 and 3 have nonlinear combined elastic and plastic behavior. The contribution of micromechanism 2 is reduced to being essentially negligible in this regime [12].

relative to glass transition (which determines the constants of the nonlinear springs and the dashpots—that is, the material properties). The net result is that as these inputs are adjusted to increase the amount of flow, the initially flat substrate flows up into the cavities on the rigid forming tool, forming a front or shoulder that more and more closely replicates the tool as increasing amounts of plastic deformation are induced. Experimental data showing the profile of this front is shown in Figure 2-5.

That is, in order for the embossing process to be successful, the inputs that control the physics of the process and therefore must be controlled are the strain rate, the induced stress (as controlled by force applied over the fixed area of the stamping tool), and the temperature.

2.2 The Demolding Process

A note should be made here that though the demolding process, if performed at any temperature sufficiently below the glass transition temperature, should have little effect on part formation, it is still important, primarily because loads on the mold

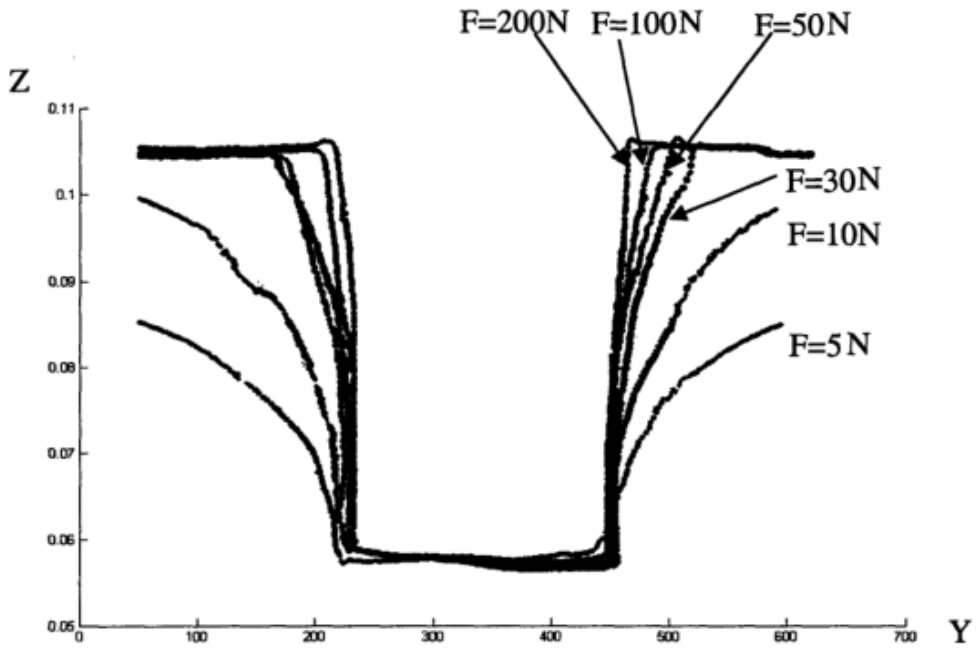

Figure 2-5: Experimental Embossing Formation Results for PMMA at Varying Force Levels: Experimental profiles for a channel measuring 500μm by 50μm (axes not to scale) are shown. As the force level is increased, the shoulder fills up into the corners of the tool features, better replicating the sharp stepped profile of the tool; at all force levels, the bottom of the channel is well-formed. [10].

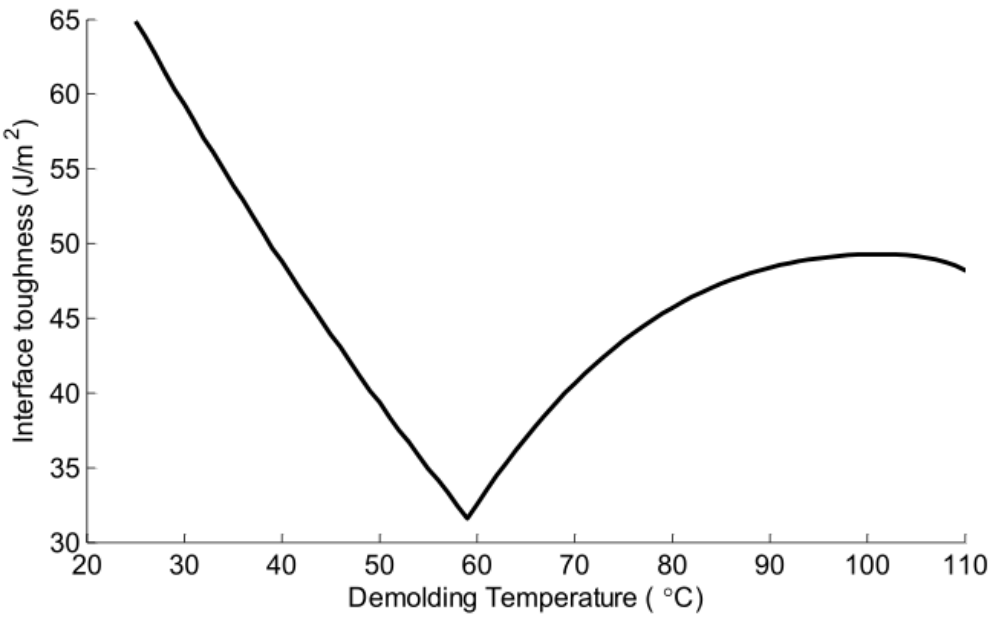

Figure 2-6: Demolding Energy as a Function of Part Temperature: Mechanical interfacial energy dominates at low temperatures, and decreases approximately linearly as temperature increases; adhesion interfacial energy dominates at high temperatures, and increases nonlinearly as temperature increases. The optimal demolding temperature is taken to be at the minimum of these energies. [18].

during demolding are high and potentially damaging due to two mechanisms. The first is the mechanism of adhesion, which can be chemical and mechanical in nature; during forming and thermal contraction, the polymer substrate comes into intimate contact with the tool (replicating features down to 10nm), and tends to mold onto and snag on any surface roughness on the tool [18, 19]. The second is the mechanism of thermally-induced mechanical stresses; simply because the polymer has a much larger coefficient of thermal expansion than the metallic tool, as the temperature is decreased, it contracts with greater and greater stresses on the tool, potentially damaging itself or the tool. These two mechanisms are opposing with temperature, and a point at which the effects are both are minimized can be found, as shown in Figure 2-6. As computed by Dirckx, the optimal demolding temperature for PMMA is approximately 60°C.

2.3 Input Parameters and Sources of Variation

In order to control the process on a practical level, the input parameters selected were induced stress, in the form of force applied over a fixed area; and temperature. In the context of this thesis work, strain rate is indirectly determined by the force setpoint and the amount of time over which forming occurs, both of which are controlled variables. A second valid set of inputs would be to control temperature and strain rate.

With the goal of this project being to study hot embossing as a process suitable for manufacturing, it is of primary interest to be able to minimize the variations in the process. In general, variations in any of the input parameters will cause some variation to the degree to which the final product is formed. That is, any change to the force setpoint, the temperature, or the forming time will affect the process physics in such a way as to change how far the flow front advances into the features of the tool.

Additionally, material variations in the PMMA sheets from which blank substrates are prepared have been found to be vast. Not only is likely some variation in glass transition temperature, due to its dependence on the precise molecular weight of the polymer, but there is significant variation in geometry. The thickness of these sheets and the resulting blanks has been shown to be wildly inconsistent from the 1.5mm nominal thickness, ranging from 1.1mm to 1.8mm. The major consequence of this fact is that the effective temperature throughout the blank substrate may be different, though the surface temperature to the forming depth has been experimentally measured to be unaffected by differences in blank geometry.

There is also some inherent variation in any production machine, as well as in any operator interactions with that machine. This is true also in this case, though through thoughtful machine design and a shift to automated processes, equipment and human variations have been minimized. Given an understanding of the relative contributions of each source of variation, development of process control can proceed.

Chapter 3

Project History and Objectives

3.1 Historical Designs

Given the goals of the project and the limitations on commercially available equipment as detailed in Chapter 1, it became clear early in the projects history that customized equipment would need to be constructed.

The first generation of equipment was developed by Ganesan and installed on an Instron 5869 load frame. It consisted of a pair of copper platens, made large to ensure temperature uniformity and heated using cartridge heaters; temperature control was achieved using Chromalox 2110 controllers. Active cooling was accomplished using tap water. The Instron load frame allowed for a variety of load profiles to be imparted to the substrate, as it had a positioning resolution of 0.0625μm and a 50kN capacity [13]. The heating and cooling rates as well as the demolding temperature, however, were not well-controlled, and the machine required some 15 minutes to heat and 5 minutes to cool due to the large thermal mass of the copper platens [13]. A plot showing a temperature profile from this machine is visible in Figure 3-1.

To attempt to improve on input parameter control and to further the goal of studying the embossing process in a manufacturing environment, the second generation of equipment focused primarily on redesigning the platens. Dirckx reduced the thermal mass of the copper platens, and switched to using a mixture of heated and room-temperature Paratherm MR oil. This provided the capability to impart both

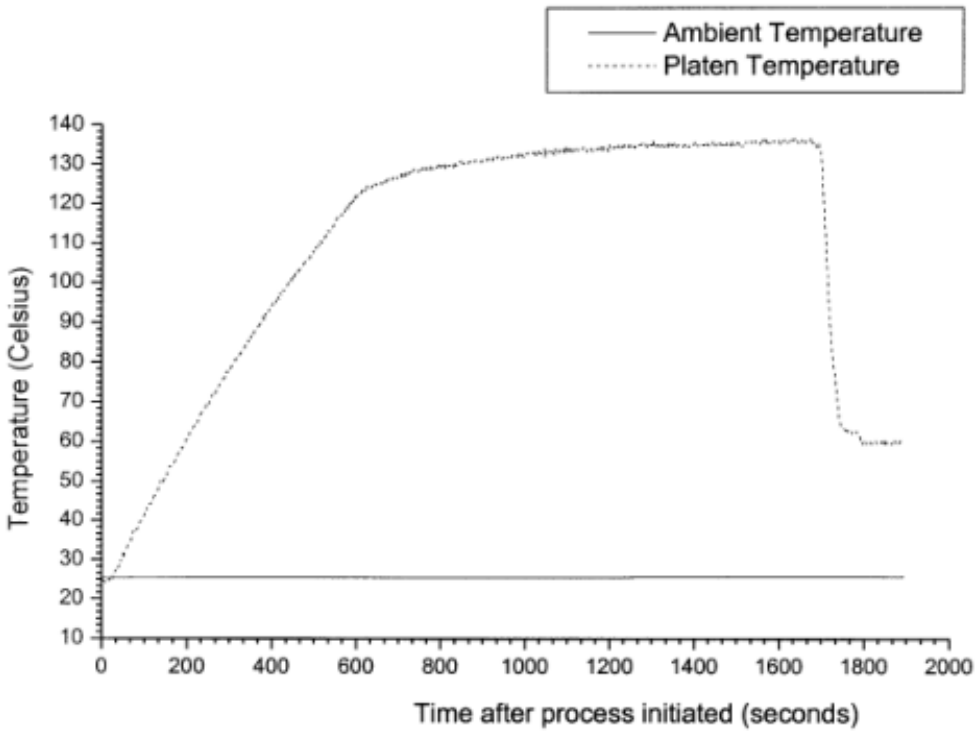

Figure 3-1: Temperature Profile for Generation 1 Machine: Though the temperature uniformity is good, some five minutes are required to get close to forming temperature [20].

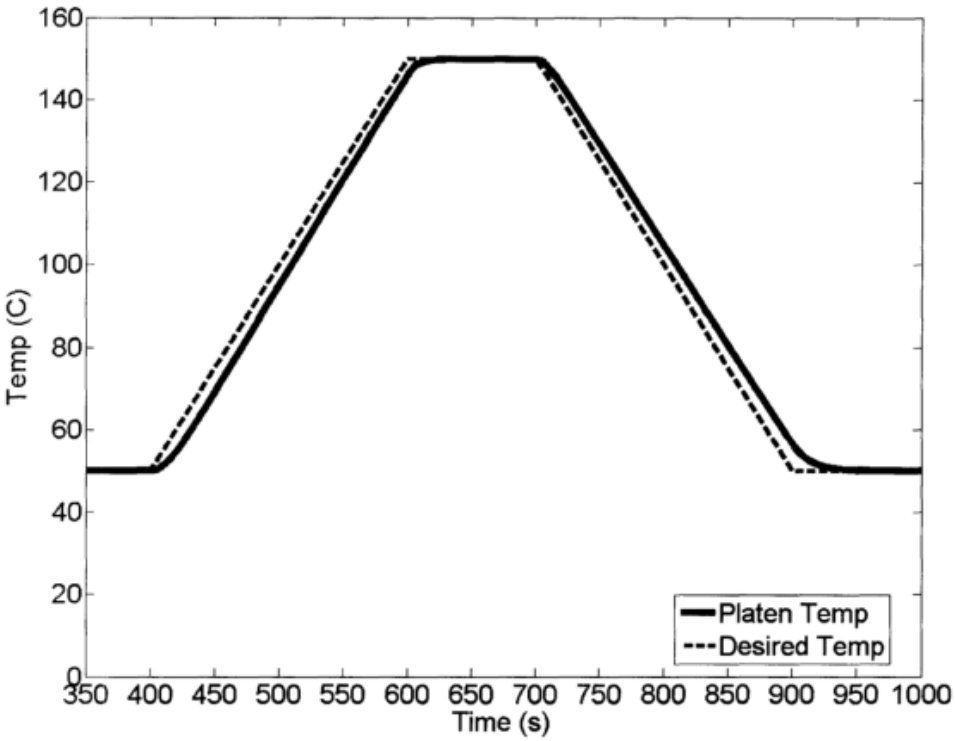

Figure 3-2: Temperature Profile for Generation 2 Machine: The Generation 2 machine showed an excellent ability to match temperature setpoints, but takes approximately 2 minutes to heat and cool, requiring the cycle time to be on the order of 5 minutes [18].

arbitrary force and displacement profiles as well as temperature profiles. The cycle time was improved to approximately 5 minutes, requiring approximately 2 minutes for heating and 2 minutes for cooling [13]. A sample experimental temperature profile for this system is shown in Figure 3-2.

The third generation of equipment, developed by Hale, broke away from the Instron load frame and attempted to develop a manufacturing-focused, fast, compact, and capable machine based on process knowledge developed from predecessors work. The machine featured a curved cantilever spine supporting a double-acting air cylinder with a 9.8kN capacity. Cooling was accomplished by bringing a large copper mass with cooled water flowing through it in contact with the lower platen, serving as a heat sink; by distancing the mass from the platen, the platen could be heated rapidly. This heat sink was guided by ceramic pins, preventing any thermal leak to the ma-

chine structure. Heating was accomplished using 1in by 3in Watlow Ultramic series ceramic heaters, which displayed a high power output as well as exceptional temperature uniformity. These heaters were installed in pockets in the aluminum forming platens and were controlled by Watlow SD6C series PID heater controllers. A load cell installed in the line of compression on the device was capable of measuring forces up to the 9.8kN capacity, and thermocouples built into the heaters measured temperature. Force control was established using a proportional valve controller on the cylinder, which responded to output signals from the load cell and from a LabVIEW software controller [13]. This equipment successfully achieved the desired cycle time of approximately 2 minutes, needing 1 minute for heating, 30 seconds for forming, and 45 seconds for cooling.

Though this equipment made strides in applying process physics knowledge to designing right-size equipment appropriate for manufacturing environments, some additional concerns arose. First was the observation that though FEA models predicted that the thin polymer substrates should be a uniform temperature throughout, cooling from only one side actually imparted some thermal gradient and caused macroscale warping throughout the finished product. The temperature asymmetry caused by cooling from only one side is visible in Figure 3-3. Second was the observation that there was thermal leakage into the machine structure over time, causing machine transients and increasing machine variation. Finally, the double-acting cylinder proved to be a less than ideal force source, due to its stiction and a minimum force requirement for motion that made controlled force application difficult. After evaluation of the operation of the machine, it was determined that another generation of equipment needed to be developed in order to successfully study process control in the context of manufacturing.

3.2 Microfactory Project Objectives

Overall, the stated goal of the microfactory project is to study the hot embossing process as applied to microfluidics devices, in a manufacturing-oriented environment.

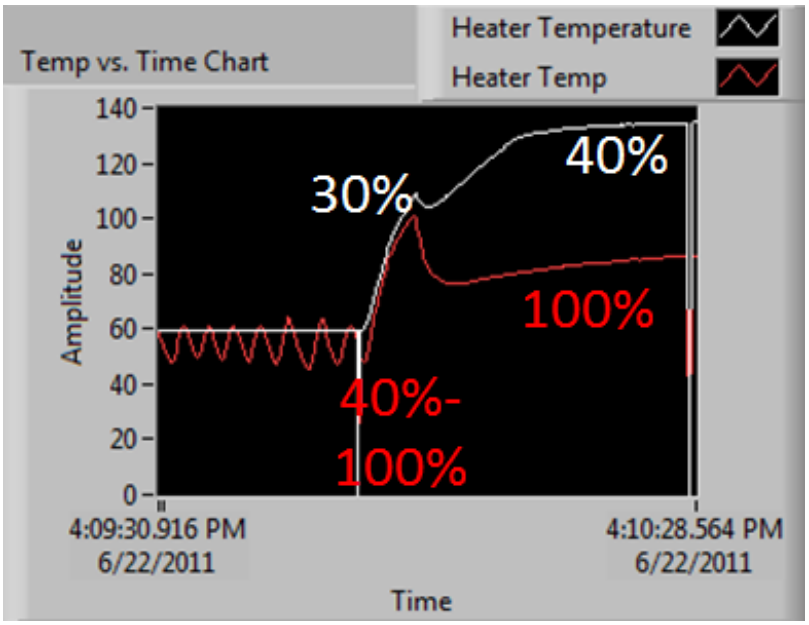

Figure 3-3: Asymmetric Temperature Profiles in Generation 3 Hardware: In this plot, the top (white) and bottom (red) temperature profiles for the generation 3 equipment can be observed; the numbers overlaid on the graph indicate the power output of each heater at that point in time. The initial heating rate of the top and bottom heaters are approximately the same, but when contact between the part and tool is initiated (noted by the peak approximately in the center of the plot), the bottom temperature diverges from the top. Due to the fact that the flow of coolant is never shut off, the bottom heater, exposed to the cooling block, struggles to maintain the setpoint temperature of 140°C, even at 100% power.

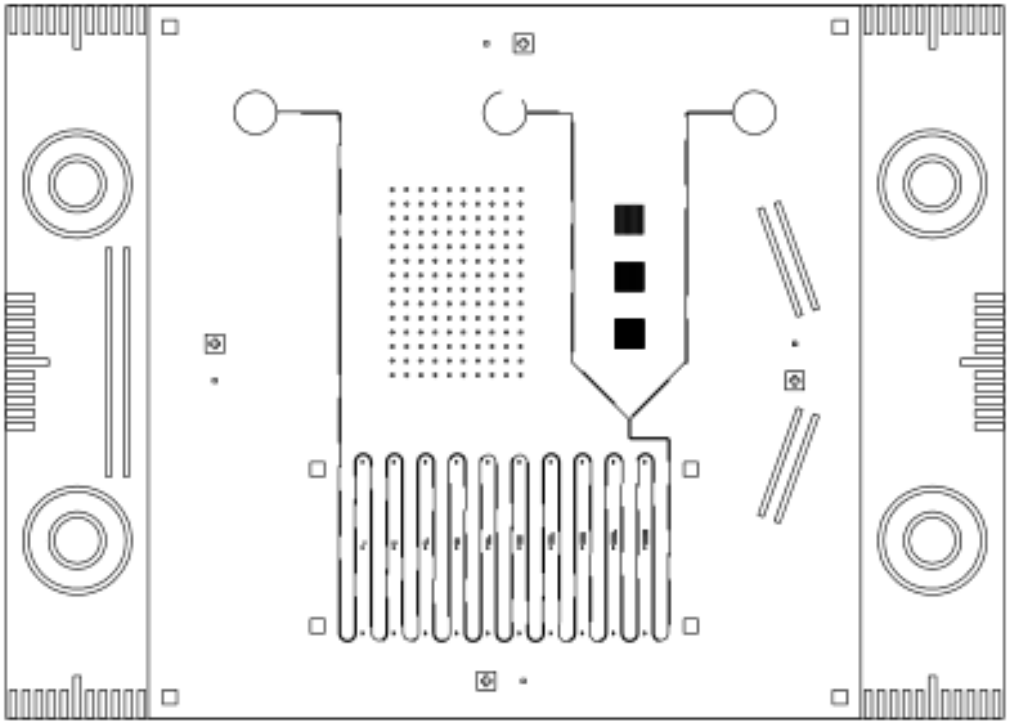

Figure 3-4: Test Micromixer Device: Fluid is input into the two rightmost ports, and exits in the leftmost port. The channels are 50μm wide. Additional test and metrology features are distributed throughout the design, including a grid of squares 20μm in size.

To accomplish this goal, the first step was to develop a testbed factory cell capable of minimizing equipment- and operator-induced variation. The work presented in this thesis contributes to this goal by developing precision hot embossing equipment serving as a suitable basis for further project developing.

Because the goal of this project is to study the hot embossing process instead of any one particular microfluidic design, a test micromixer design was chosen. In this design, two streams of fluid flow together and meet, and then proceed through a long serpentine channel; eventually these two streams become fully mixed by the process of diffusion in this long channel. The characteristic dimensions of this test device are channels 40μm deep and 50μm tall, giving an aspect ratio of 0.8. The finished devices are relatively small in size, occupying an approximately 2.5cm by 2.5cm embossed area. The mask used to create this test pattern is shown in Figure 3-4.

To complete the device, it must be sealed on the top. Again, because the goal of this project is to study the hot embossing process, any suitably quick and simple sealing process was deemed appropriate to the project goals. Pressure adhesive tape manufactured by Tesa Tape Inc. proved to be a superior choice due to its ease of use. The thick backing gives the tape rigidity, prevent it from collapsing into the channels. The adhesive is compatible with some biological applications, and has a thickness small enough to avoid filling the channel.[1] The fact that the tape presents a nonuniform fourth wall (consisting of adhesive instead of PMMA) to the fluid flow is not a major concern for the purpose of developing the hot embossing process, but could be problematic for some applications.

Using this tape gives an interesting option for measuring part formation. Because the shoulders of the channel profile are the last part to form, and flow upward in a front of decreasing curvature with increasing fidelity to the tool (see Figure 2-5), these are the chief measure of part quality—that is, how closely the tool pattern was replicated on the finished product. When the tape is applied to the top surface, a change in the index of refraction occurs where the adhesive bonds to the PMMA, creating an optically visible shadow, shown in Figure 3-5. By imaging each device and measuring the width between these lines, the width of the shoulders can be extrapolated, and the profile inferred, based on the fact that the bottom of the channel forms correctly even under very low applied forces. This has proven a much faster and more holistic measurement than individually assessing each profile using confocal microscopy, scanning electron microscopy, or other tools. In addition, by performing a functional test and flowing fluid through the device, the point at which the two input fluid streams are fully mixed serves as another holistic measure of quality (as it is dependent on flow rate), and can indicate problems at the inlet or outlet ports that are not visible in the channel width measurement. An image showing the two streams gradually mixing is shown in Figure 3-6.

By quantifying these measurements, a numerical output of quality can be made.

[1] Due to the fact that the tape is under development by Tesa and is proprietary, further details will not be published in this work, per their request.

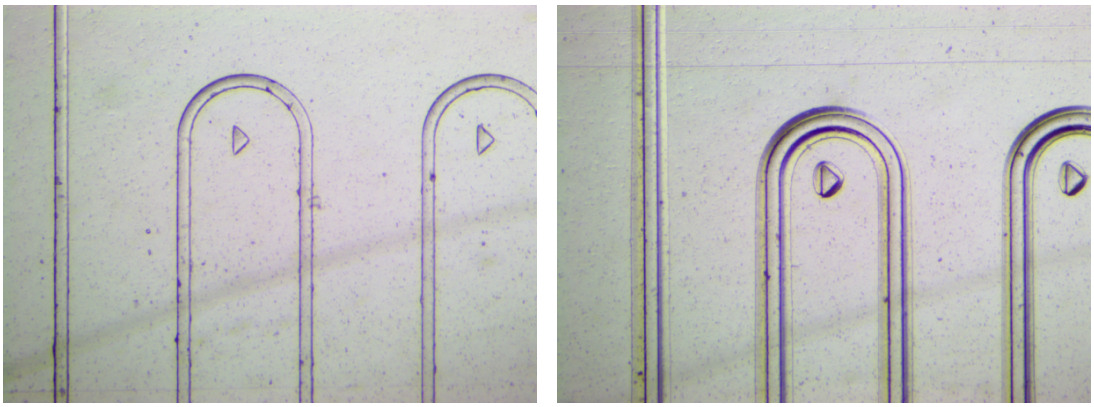

Figure 3-5: Well-Formed and Poorly-Formed Channels with Tape Applied: Images of (left) a well-formed device with sharp corners, and (right) a poorly formed device with rounded corners. The line of tape contact marking the channel width is visible by a change in index of refraction [14].

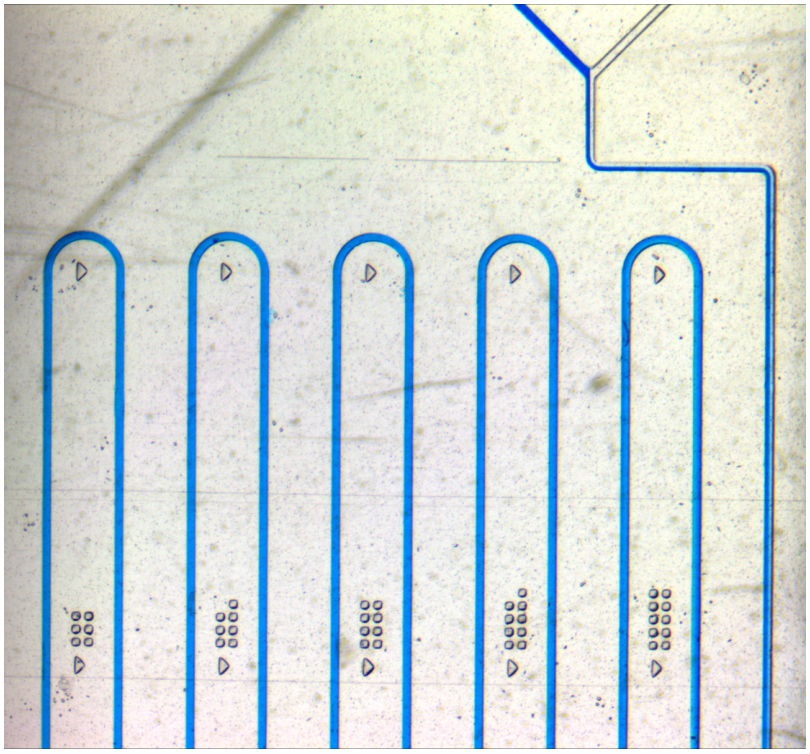

Figure 3-6: Fluid Flowing through Test Device: The two fluids (blue and clear) enter unmixed, and the color becomes uniform as it passes through the device [14]. The degree of mixing depends only on how long the two streams have been adjacent, as it is a diffusion process; so the mixing point is a measure of flow velocity, which is controlled by the channel profile.

Given sufficiently precise embossing equipment and materials handling, any variation measured using these means could then be accounted for by adjusting the embossing forming parameters. Successfully implementing this closed-loop cycle-to-cycle automated feedback control of the process is the central goal of the microfactory project.

Chapter 4

Design of Precision Equipment

4.1 Motivation and Design Specifications

The overarching goal of this project is to develop an experimental testbed "micro-factory" on which closed-loop control of the hot embossing process, as applied to fabrication microfluidic devices, could be investigated. However, in order for this effort to be successful, the first step was to develop a platform with sufficient precision, repeatability, and reliability to allow for it to be abstracted out of the process control efforts.

To this end, several key needs were identified.

1. The equipment needed to move precisely. Only one degree of freedom is required to complete the embossing process. However, to minimize equipment variations, this linear motion needed to be as repeatable as possible.

2. Precise and repeatable control of the applied force was necessary.

3. The substrate needed to be repeatably and accurately registered with the tool, to allow for existing substrate features to align with tool features.

4. The active thermal mass of the system needed to be minimized in order to allow for diminished energy waste as well as faster heating and cooling cycles.

5. A symmetric thermal profile between the upper and lower surfaces of the substrate was required in order to prevent residual stresses and any resulting macroscale warping of the substrate.

The previous generation of precision equipment had addressed some of these concerns, but also had discovered problems that called for another design revision [13]. In the following sections, the design work involved in developing solutions to each of these needs is detailed, as well as the final solution to each design problem.

4.2 Design

4.2.1 Precision Linear Motion

The first need was for precision and repeatability in the forming motion of the machine. In the work done by Hale, the necessity of separating imprecise force sources from precision linear motion became clear. The double-acting air cylinder used in that equipment, while providing a surfeit of forming force, did not have very controllable or repeatable motion.

The guiding design principle was then to decouple any parasitic motions of the force source from the linear motion of the platens. A precision linear guide of some design was required to accomplish this task. The guide needed to have a range of motion sufficiently large to allow for a gap into which blanks could be loaded into the machine; based on manual ease of use and the existing end effector on the commercial robot arm, this gap was quantified to need to be approximately 0.4in.

The first concept that was developed was to use a parallel flexure design to constrain all undesirable degrees of freedom. Since flexures exhibit nearly perfectly repeatable elastic behavior, they are a desirable mechanical element for applications where precise motion is required [30]. The flexure concept was based on a stage mounted on a set of mirrored parallel flexures; the symmetry of the setup would reduce or eliminate planar parasitic errors. However, two major design challenges existed for the flexure. First, the parasitic errors due to in-plane rotation ("rocking

the cradle") were significant. If force application were even slightly off center, the parallelism of the flexure would be severely compromised, in particular along the direction axially parallel to the blades. Limitations on in-house fabrication capabilities restricted the flexure design to a minimum thickness of approximately 0.050in. Given this fixed constraint, the solution was to make the blades of the flexures wider and thus more resistant to torsion. Using sequential finite element simulations, it was determined that the flexures were required to be 25mm wide to rein any torsional errors in to 1μm under a 10N torsional load.

The second problem was that a 0.4in range of motion was required. Most materials suitable for flexures begin to yield at only a few percent strain; aluminum, a preeminent choice, yields at approximately 0.2% strain [31]. To prevent stresses in the flexure from causing it to yield with a safety factor of 2, finite element simulations, as shown in Figure 4-2, indicated that the blades needed to be at least 100mm long, giving the flexure a total footprint of 258mm by 25mm, which was large, but still smaller than the previous generation. Diagrams detailing the completed flexural bearing design are shown in Figure 4-1.

Unfortunately, by making the blades longer to increase the range of motion of the flexure, their torsional stiffness was decreased, and they also needed to become wider to compensate. This increased the bending stiffness of the blades, reducing their range of motion, and so on. In the end, the flexural design was rejected because of this trade-off; it was believed that other solutions likely existed that would not require a compromise on performance and compactness.

The next design concept to be investigated was to use an air bushing as a linear guide. In an air bushing, a permeable medium allows air to flow into a bushing; a precision shaft rides in the bushing, with a thin gap between the surface of the shaft and the inner walls of the bushing. A cushion of high-pressure air forms in this gap, creating an extremely stiff and low-friction bearing. The air bushing investigated for the design, a 2in diameter New Way Air Bearings air bushing, had a radial stiffness of 110N/μm and a pitch stiffness of 23Nm/rad [23]. This means that under an estimated radial cross load of 100N, the air bearing would deviate less than 1μm from its radial

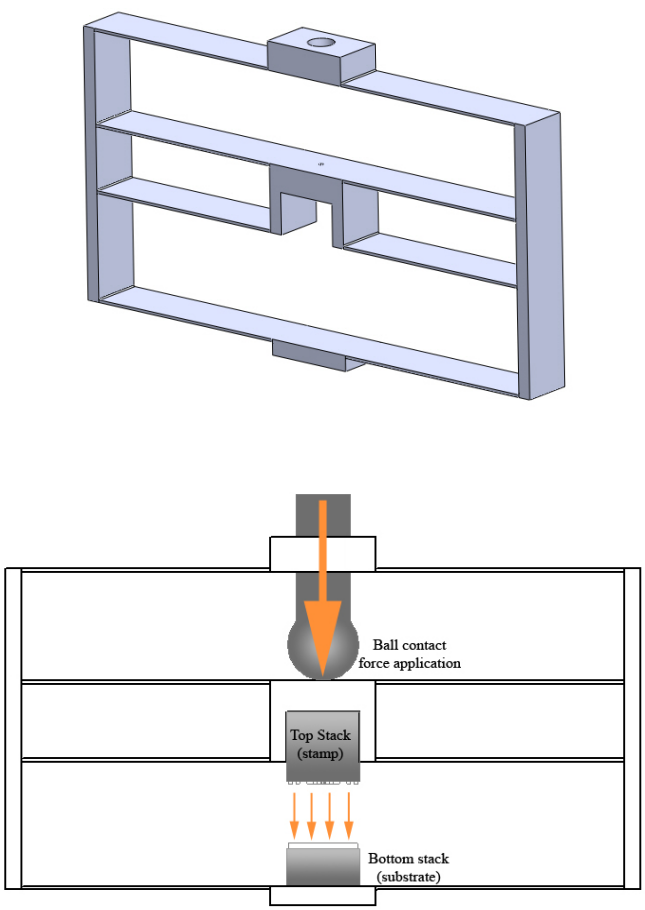

Figure 4-1: Flexural Bearing Design: Shown here are the flexure design (top) and a schematic of how this design would be incorporated into a forming machine (bottom). In this design, the tool was intended to be mounted facing downward on the center stage, and the facing platen mounted on the base at the bottom of the flexure. A shaft passing through the opening at the top would apply a force to the top of the stage during forming.

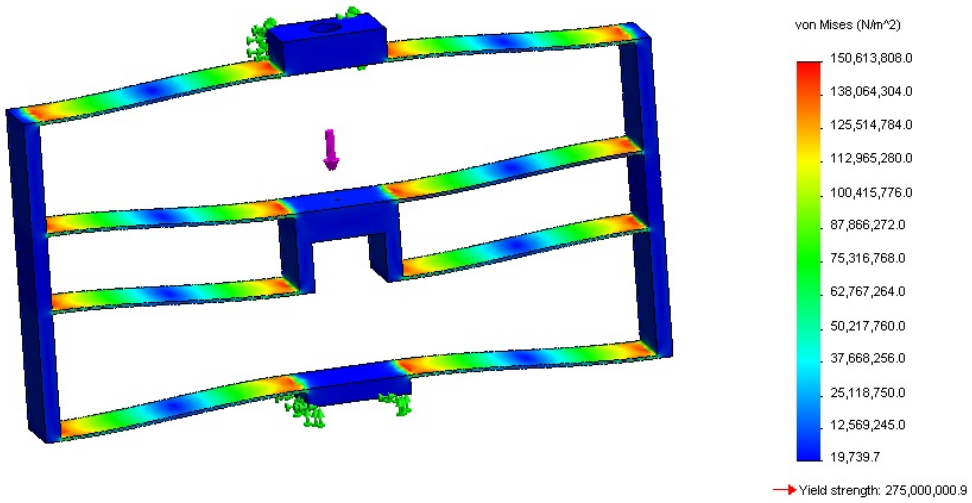

Figure 4-2: Simulation of Stresses under 12mm Z-Displacement: To ensure a safety factor of approximately 2, the length of each flexure blade was required to be approximately 100mm.

path. Under a pitch cross load of 20N at the point of application (a worst-case scenario that a clever coupling mechanism could minimze), the deviation of the top surface of the lower platen (designed to be 176mm from the point of application) can be computed as:

$$\frac{(F_{cross-load})(r^2)}{K_{radial}} = \delta. \tag{4.1}$$

Substituting in known values, the deviation is calculated to be 6.734µm along an arc of radius 176mm. In contrast, finite element simulations indicated that the flexural bearing deviated 5.5µm under a 10N load parallel to the blades, and 12.0µm under a 10N load perpendicular to the blades, as shown in Figure 4-3. In addition, simulations indicated that the stiffness in the parallel direction decreases as the stage translates down, due to a buckling effect on the blades; the simulation then shows error in the best-case scenario. Thus, the worst case scenario for the air bushing presented at minimum a 100% improvement over the best-case scenario of the flexural bearing.

The air bushing was also compact and simple in construction, making its implementation straightforward. Based on its clear superiority, the air bushing was selected as the optimal design choice for a guide for the linear motion.

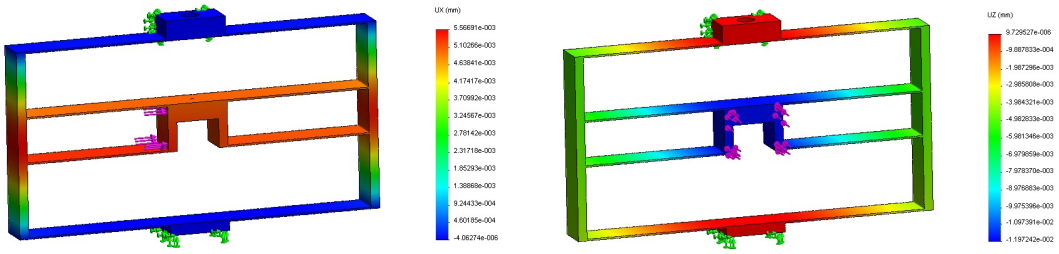

Figure 4-3: Finite Element Simulations of Planar Stiffness of Flexural Bearing. Under 10N in-plane loads, the flexural bearing deformed 5.56µm parallel to the blades (left) and 12.0µm perpendicular to the blades (right). Under combined downward and cross loading, the planar stiffness decreases due to buckling effects, and the error becomes worse.

The major design challenge presented by the air busing was the fact that it did not constrain axial rotation of the shaft, which was highly undesirable. The immediate solution was to use a clamped blade flexure to control this motion. By orienting the widest dimension of the blade tangential to the axial rotation, the resistance to rotary motion was increased from nearly zero to 3.3×10^5N/m, as estimated by the finite element simulation shown in Figure 4-3. Spring steel with a thickness of 0.01in was chosen for its ability to withstand large strains, making it capable of traversing the required 0.4in gap at a blade length of 1.64in. The downside of using a flexure in this application was that by making the flexure compact, the small angle approximation that determines the linearity of its motion was violated, and at the extreme ends of its orbit, it deviates from the linear stiffness curve expected for this type of element. The solution was simply to linearize the system around the point at which the tool contacts the substrate, and to neglect to model the nonlinear extremes.

4.2.2 Precise and Repeatable Force Actuation

Once a linear guide mechanism was chosen, a force source also needed to be chosen. The first concept was to continue to use the pneumatic cylinders from the previous generation of hardware. By placing a spherical contact on the end of the cylinder shaft, the motion transmitted to the linear guide could be constrained to be perfectly linear—all other cross-motions would just result in slip of the contact point around

the contact surface.

However, the pneumatic cylinder presented other problems. Both double-acting and spring return cylinders exhibit a suite of nonlinear behaviors such as stiction and dead zones. Highly granular force control becomes difficult, and successfully applying linear control techniques becomes a difficult battle. After review, it was decided that these pneumatic cylinders were not appropriate for this precision application, and an alternative was sought.

Electromagnetic actuators such as voice coils were also briefly considered. These were soon rejected, primarily due to their low power density compared to pneumatic devices. Without a mechanical element such as a lead screw to multiply force, an enormous actuator would be required. Incorporating such a mechanical element, however, reintroduces some of the nonlinear problems associated with the pneumatic cylinders, such as backlash and stiction. Pneumatic actuators were decided to be superior.

The final design for the pneumatic actuator was an expandable pneumatic bellows, also known as an air spring, and sold commercially as Firestone AirStroke, and shown in Figure 4-4. These devices are most widely recognized as being used in kneeling buses as a means to gently lower the front entrance of the bus to allow for easier boarding, as well as in trucks for shock absorption. It consists of a rubber annulus capped at each end with a steel plate. The annulus was specially designed with reinforcing ribs to make its motion as purely vertical as possible. Because the motion was purely elastic stretching and relaxing as the bladder was inflated and deflated, the continuum of force control was excellent, and had exhibited perfectly linear behavior, as shown in Figure 4-5. The model selected was the Firestone AirStroke W01-M58-6155, with a maximum force exertion of 6.5kN and a maximum stroke of 50mm [21].

Though the pneumatic actuator was designed to exhibit completely vertical motion with little parasitic error, any errors in vertical motion, combined with possible offset errors generated by assembly, could create cross-loading forces on the linear guide, decreasing accuracy and repeatability. To address this problem, a means of coupling the actuator to the linearly guided shaft needed to be developed that trans-

Figure 4-4: Firestone AirStroke Pneumatic Actuator: The actuator consists of a specially shaped and reinforced rubber cylinder between two metal plates, which have fixtures for mounting.

mitted only the desired vertical force and rejected any cross-loading forces. The design solution was to use passive contact between the top surface of the actuator and the bottom surface of the shaft riding in the air bushing, in which the shaft merely rests on the top plate of the air bearing and maintains contact through its own weight. The upper bound on the radial and pitch cross-loading forces is the fact that these forces can only be transmitted by friction between the two machined surfaces of the guided shaft and the actuator cap; once the upper bound of static friction is exceeded, the frictional force is reduced to sliding friction, and minimal cross-forces are transmitted.

One last consideration remained. All of these components needed structural support, and this support needed to be designed such that it did not detract from the precision motion when loaded with a maximum force of 2kN. Though the previous generation of hardware had selected the C-frame as showing acceptably small levels of deviation [13], the goal of this thesis work was again to improve on that performance if possible. A symmetric design was then preferred; an O-frame structure was the first logical choice. When loaded, it deforms symmetrically: the legs stretch in

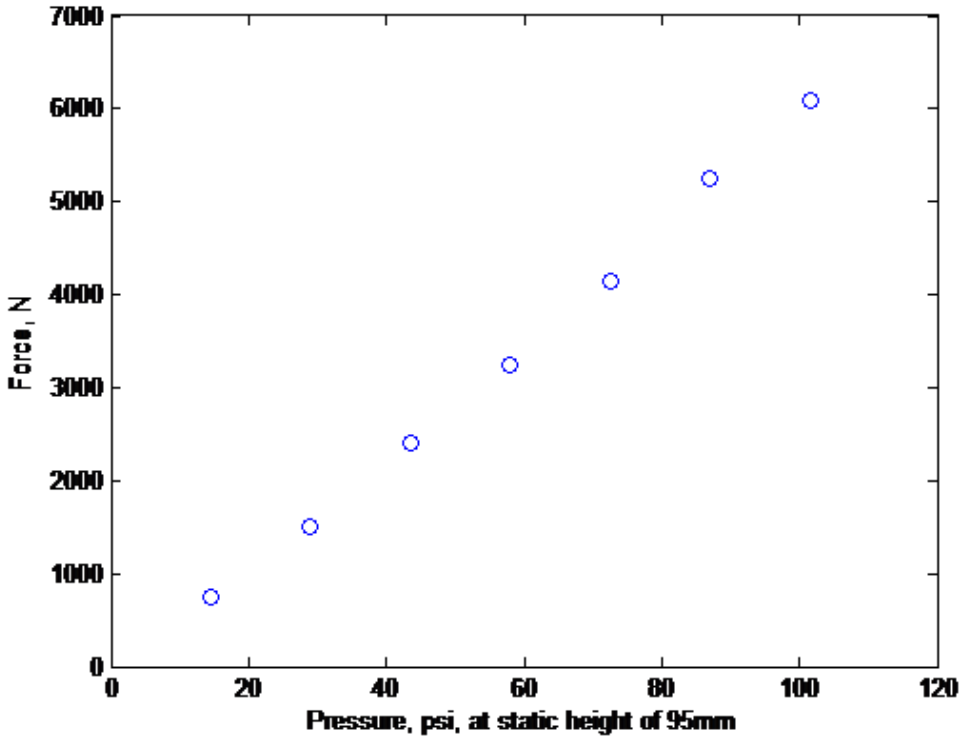

Figure 4-5: Linearity of Output Force with Pressure: Extracted from the curves provided by Firestone, at a fixed height of 95mm (the approximate height of the actuator when the platens are in contact), increasing pressure generates a highly linear increase in force [21].

a tensile fasion, and the top and bottom crossbeams bend symmetrically in 3-point bending about the point of load application. By making the structure of 1in thick aluminum plates, the structure became highly rigid. The bending of the top plate under maximum load was shown in finite element simulations to be limited to 10μm, and the bending occurs in such a way that objects situated in the center of the top crossbar are essentially translated upward but not deformed (a simple obstacle to overcome, merely by utilizing closed-loop force control).

This stiction-free actuator, combined with the extremely low friction air bushing and elastic guide flexure, produces smooth and perfectly controllable linear motion. The degree of repeatability of this motion is believed to be on the level of only a few microns, as no variation was measurable using a dial gauge resolving down to 6μm.

4.2.3 Precision Substrate Registration

The other key area necessitating mechanical design innovation was in the placement of unformed blank substrates onto the platen. In previous generations of hardware, a 3-point kinematic alignment system was demonstrated to allow repeatable placement to 25μm when combined with an industrial pick-and-place robotic arm [15]. A pair of small tabs separate from the pins applies a downward force on formed substrates during demolding. This system was carried over to the new generation of hardware, in the form of dowel pins potted into CNC machined bores in the lower platen, and appears in Figure 4-7.

In addition, due to the fact that the blank substrates have pre-existing inlet ports, a need to be able to accurately register the blank substrates with existing tool features existed. To this end, a planar flexure allowing translational motion in X and Y as well as rotational motion about the normal Z axis was designed. Due to strong coupling between each axis, this flexure serves best as a manual as-needed calibration element, and the six thumb screws included allow its planar position to be fixed in place once the proper location is determined. The planar flexure backs against a precision flat plate and transfers load to it and thus to the machine structure, allowing it to withstand the full range of forming loads. A diagram of the flexure explaining its

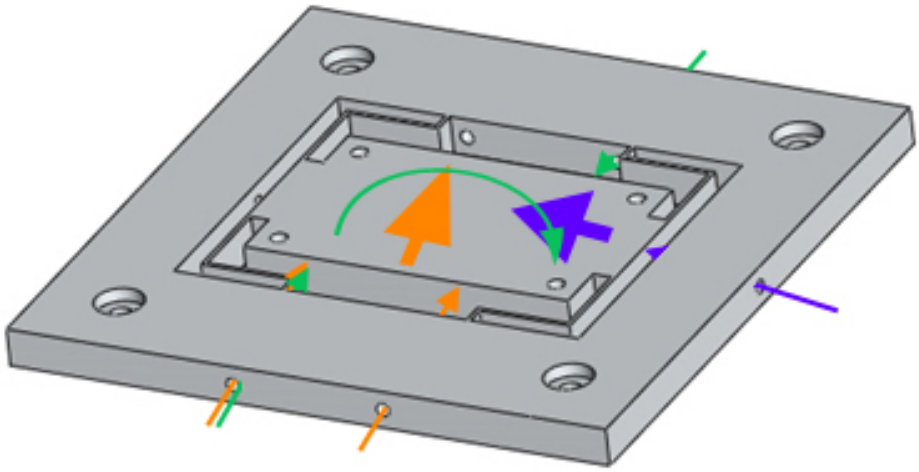

Figure 4-6: Planar Adjustment Flexure: A solid model of the planar flexure allowing position calibration between the tool and the substrate. The holes visible on the vertical walls are threaded for thumb screws, which are used to manually adjust its planar position and angle. By adjusting sets of screws parallel to a direction of motion (orange or blue), the flexure may be translated; by adjusting two diagonally opposing screws (green), the flexure may be rotated.

operation is shown in Figure 4-6.

4.2.4 Thermal Design

In the previous generation of hardware and in industry models, the rate of heating and cooling places a limit on the minimum cycle time. It has been determined experimentally that in order to form a quality part, at proper forming temperatures and pressures, approximately 30 to 60 seconds of forming time are required. However, to bring a machine's active thermal mass to the forming temperature and then cool to the demolding temperature, anywhere from a few minutes to more than ten minutes may be required. For example, the large copper platens utilized by Ganesan to ensure equal temperature distribution required approximately 15 minutes to reach forming temperature (though it closely approached it in 5 minutes), and additional 10 minutes to cool to demolding temperature after forming [20].

The design of the precision equipment detailed in this thesis sought to address this concern by minimizing the active thermal mass. This consisted of two key design

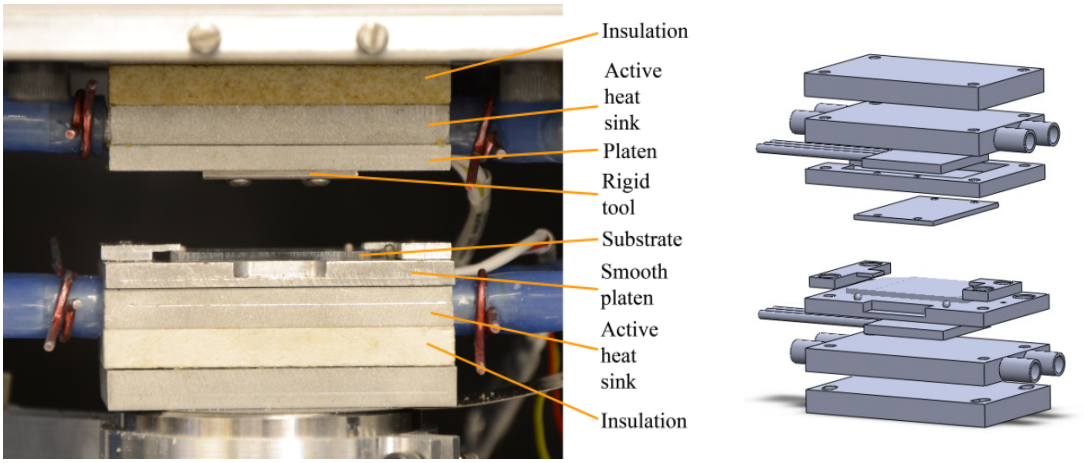

Figure 4-7: Final Design for the Thermal Stack: A photograph of the completed thermal stack (left) has key components labeled; an exploded view of the stack (right) shows internal components not visible in the final assembled version.

features: one was that the active thermal mass needed to be separated from the large machine structure, which would act as a large capacity heat sink. The second was that the active thermal mass itself needed to have as little heat capacity as possible to allow for it to be rapidly heated or cooled.

To separate the active mass from the machine structure and prevent heat loss, Glastherm HT fiberglass-reinforced mineral insulation was used. With a compressive strength at forming temperature of some 186MPa, it is sufficiently rigid to prevent excessive deformation. A thermal conductivity of 0.27W/mK prevents more than a few degrees of temperature rise in the adjacent machine structure, even after long periods of operation [32]. During one forming cycle, the unrealistic worst-case scenario is that one aluminum structural element of mass 0.032kg absorbs all 150W generated by the heater, which is conducted through a 0.25in block of the insulation, with no losses to radiative or convective heat. Given a commanded temperature step from 60°C to 130°C, the resulting rise in the structural element is given by:

$$\left(\frac{h_{conduction} L \Delta T_{command}}{m C_p}\right)(t_{heat}) = \Delta T_{structure} \tag{4.2}$$

Substituting known values, this number is found to be 0.371°C. Additionally, because the system is then cooled actively to return to the demolding and idling

temperature of 60°C, the net effect is that the steady-state operating temperature of the machine structure oscillates by no more than this amount per production cycle, and that there is not a cumulative increase over long periods of operation.

However, the insulation, unlike machined metal, presents an irregular surface; to ensure parallelism in the thermal stack, a layer of epoxy was cast in-place on top of the lower insulation block to create a planarizing layer.

To minimize the active thermal mass, the forming platens were made just large enough to accommodate the flat-profile Ultramic 150W ceramic heaters. The heaters are ensconced in pockets milled on the underside of each platen, in a design revision inspired by work done by Hale [13]. The platen thickness was able to be reduced to 4mm, providing a ceiling with a thickness of only 1.5mm separating the heater from the substrate. This ceiling does not span the entire width of the tool, meaning that two ridges on either end support the ceiling under loading by the flat tool surface, and that the ceiling is not required to support the full forming loads.

Another important goal was to make the thermal mass of the top and bottom thermal stack as symmetric as possible. Through experimentation, the fact that the formed substrates were sensitive to residual thermal stresses was discovered. Previous generations of equipment only cooled the devices from one side, creating residual stresses by thermal means [13]. These stresses caused macroscale warping and curving across the area of the device. To avoid this effect, the heating and cooling mechanisms were made identical on the top and bottom forming surfaces as much as possible.

Different structural designs were required for the top and bottom thermal stack; for example, pockets needed to be cleared in the bottom platen to allow clearance for the bolts holding the tool to the top platen's face to descend, while the top platen presents a flat face. The final design of the lower platen gives an active thermal mass of 16,359mm^3, which includes the demolding tabs, the lower platen, and the lower cooling block (see Figure 4-7). The final design of the top platen, including the upper platen, the cooling block, and the tool, gives an active thermal mass of 16,387mm^3. The thermal masses of these two stacks then differ by only approximately 0.1%. Given that each aluminum thermal mass is heated using a 150W heater, at 100%

output power, assuming no losses to radiation or convection, and with a commanded temperature step of 60°C, the minimum amount of time required to heat a single platen to forming temperature can be computed using the relationship:

$$\frac{V\rho C_p}{Q_{heater}}\Delta T = t. \tag{4.3}$$

Substituting known values, the minimum time is found to be 17 seconds. In practice, a longer time is required, as some energy is lost to radiation, some is dissipated electronically, some is absorbed into air and leftover coolant contained in the cooling block, and a small portion is leaked into the machine structure.

The Ultramic ceramic heaters exhibit excellent uniformity of heating which, combined with the high thermal conductivity of the aluminum platen, provide a sufficiently even heating surface for forming. The AlN material of the heaters has a thermal conductivity of 150W/mK, comparable to the 180W/mK of aluminum; the temperature range across the area of the heater's surface varies by less than 2°C [22]. Cooling blocks through which a U-bend channel runs were made just large enough to provide sufficient flow for cooling, and to be large enough to facilitate ease of machining. The initial finite element analysis shown in Figure 4-8 demonstrated that aluminum had sufficient thermal conductivity to create an even temperature distribution compared to copper, so it was chosen over copper for machinability. The analysis also confirmed that a simple external U-bend design was sufficient to create appropriately symmetric and well-distributed temperature profiles. Water at 20°C is used as a coolant. To further minimize the active thermal mass, at the start of each heating cycle, a jet of air is passed through the open-tank cooling system to push any water out of the cooling blocks. This jet is then shut off to further facilitate heating.

An important detail to note is that temperature is not measured directly at the forming surface, as the thermocouples are embedded in the ceramic heaters. However, experiments performed by placing thermocouples on the surface of blanks and changing the temperature demonstrated that the high thermal conductivity of the aluminum platens, combined with the low thermal mass, mean that the surfaces of

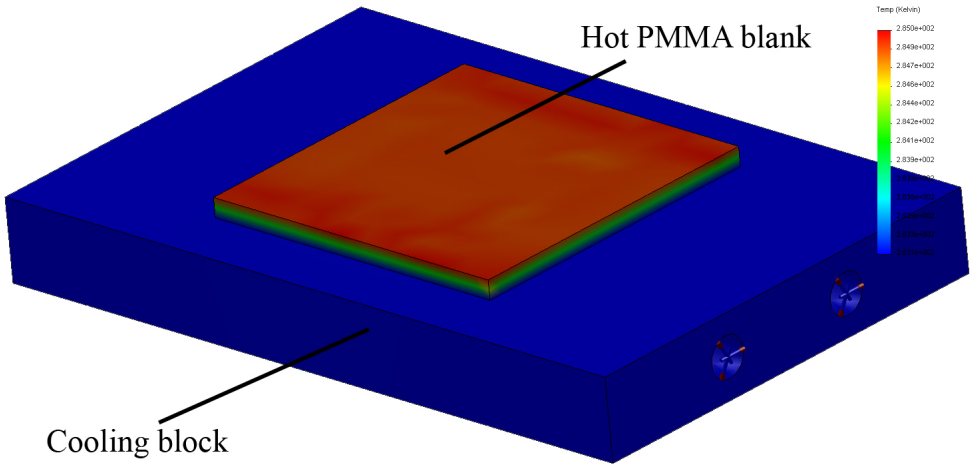

Figure 4-8: Finite Element Simulation of Cooling Peformance for Aluminum: finite element models of the cooling block showed that within 30 seconds, the block and a heated piece of PMMA placed on top both achieve a uniform temperature distribution. The scale bar ranges from 283K to 285K.

the plastic substrate differ from the temperatures measured in the heaters by less than 5°C during rapid temperature changes, and take only a few seconds to achieve thermal equilibrium.

4.3 Completed Hardware Design

Figure 4-9 shows a model indicating key components of the completed hardware; Figure 4-10 is a photograph of the completed hardware.

Inside the O-frame structure, the actuator is mounted to the base via a pair of aluminum spacer bars to allow clearance for an air hose to be attached. A mounting plate with a button is fastened to the top, and a donut-shaped load cell rests centered on this button. A precision-ground steel shaft rests on top of this load cell, and is guided in its vertical motion by an air bushing secured to the wall of the O-frame. A blade flexure is clamped between the top surface of the shaft and the lower thermal stack; it is also secured to the frame through another clamp on the opposite end. The lower thermal stack is mounted on the top of the shaft; it is actuated to raise up and meet the tool, which is mounted at a fixed height on the ceiling of the frame. The

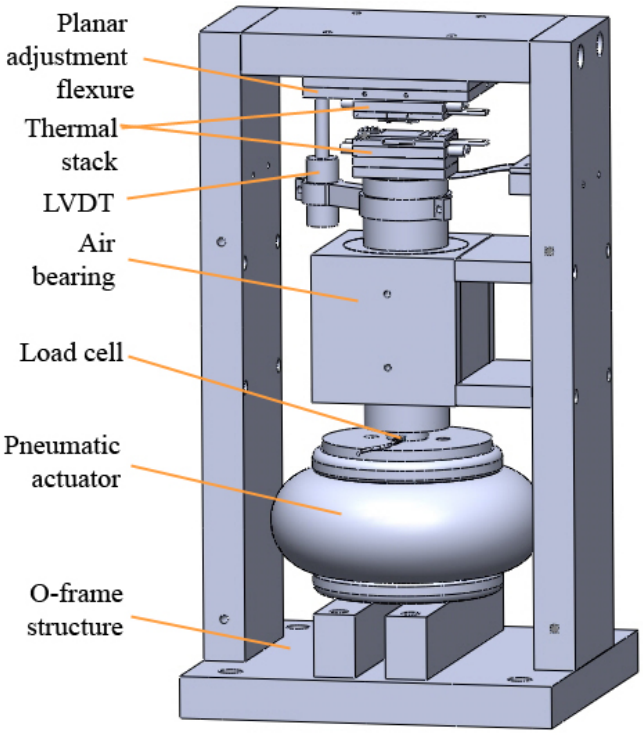

Figure 4-9: Model of Completed Hardware: This is a solid model of the finalized hardware with key components labeled.

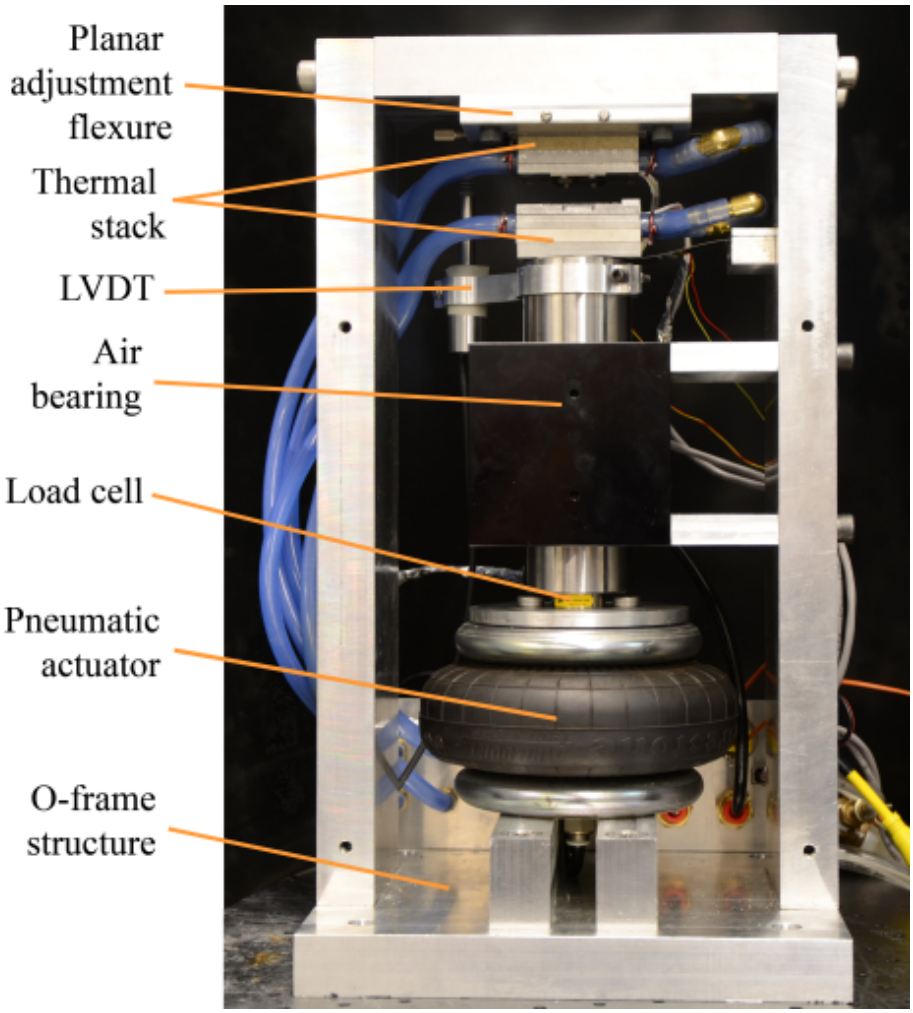

Figure 4-10: Photograph of Completed Hardware: In this photograph, the actual physical hardware, with key components labeled, is shown.

tool rests on the bottom edge of the top thermal stack, which is bolted to the planar adjustment flexure. The load path is then from the actuator through the shaft, active thermal stacks, and into the O-frame structure.

Several other features have been incorporated in the equipment design. A high-impact polystyrene shield applied to the front of the machine (not shown in Figure 4-10) both prevents access to pinch points as well as protects operators from possible catastrophic failure of the pneumatic actuator. On the rear face of the equipment, a custom-designed panel provides access ports so that cables may be easily removed and reattached to facilitate relocation and rearrangement. The full size of the equipment, disregarding any separate subsystems required for pneumatic, hydraulic, or electronic support, is contained within a 25cm by 25cm footprint, with a total height of some 44cm, making it compact and easily transported. This particular iteration of the equipment was designed to be a right-size machine, specifically engineered to handle the approximately $6cm^2$ area of the test devices used to study the hot embossing process. However, in industry, there is interest in the capability to emboss larger areas and produce larger devices, such as the size of a 3in by 1in microscope slide, a standard credit card, or a 4 inch wafer. The design of this equipment was intentionally made to be perfectly scalable; simply by increasing the rigidity and spatial capacity of the structure and the force capability of the actuator, larger areas could be embossed. The greatest design challenge in embossing larger areas is to ensure parallelism between the upper and lower platens. Over larger areas, it becomes more and more difficult to ensure that even a surface that has been machined flat is, in fact, precisely flat to a level that has no ill effect on the final product. The researcher anticipates that passive systems to promote and ensure parallelism but that are still capable of withstanding load will be an area of research interest should this design for precision equipment be propagated. More details on the scalability of this design are presented in Chapter 6.

4.4 Control System Design

After establishing sufficient precision of the linear motion involved in the compression step, development of closed-loop feedback control to allow for precise input matching in force and temperature was the next step. The thermal control was accomplished using Watlow SD6C model heater controllers. Using a PID control scheme, these two controllers could be set independently to account for any physical differences in heater output or in thermal behavior of the system. This loop runs independently and accepts setpoints from the main control software, and is indicated in a black dashed boxed in Figure 4-12.

The force control was accomplished using a loop consisting of a Futek LTH-300 load cell capable of measuring a maximum 500lb load; the stiction-free pneumatic actuator; and a voltage-controlled electronic pressure regulator, a ControlAir T550X. The voltage signal from the load cell is hardware-filtered to remove high-frequency noise and crosstalk. The hardware filter is constructed of a 100kΩ resistor and a 0.1μF capacitor, which give the filter a time constant of 10ms. The signal is then software-filtered with a low pass filter with a time constant of 50ms; this was determined experimentally to be necessary to prevent any noise disturbances from causing the system to over-respond or track into instability. Additionally, the force reference value is low-pass filtered with a time constant of 50msto remove any sharp steps generated by the software. After subtracting the filtered measured force from the filtered reference, the error is passed through a PI controller and summed with a feedforward of the filtered reference value. All computation is done in units of force, and is at the end converted to units of voltage and commanded to the electronic pressure regulator. This force control loop is shown in the green dashed box in Figure 4-12.

Originally, it was thought that an open-loop pressure regulator would be sufficient. However, after testing this regulator, it was discovered that it exhibited strongly nonlinear behavior, and increased pressure at a faster rate than it released pressure, and that this effect varied with the magnitude of the commanded pressure. The

result of this nonlinear behavior was to destabilize any linear control efforts; only by severely detuning the controller to a level of low performance could experimental stability be achieved. In addition, this pressure regulator was inconsistent in achieving and maintaining setpoints, and exhibited low repeatability of pressure output for a given voltage input, varying by up to 10%. To solve this problem, the ControlAir T550X was replaced with a ControlAir T900X, which featured internal electronic feedback to maintain a pressure setpoint. The replacement pressure regulator not only exhibited symmetric pressure increase and decrease behavior, but also was able to maintain its setpoint accurately.

To design the controller, the system was identified by measuring a step response from a voltage commanded to the actuator to the force measured by the actuator. The plant then consisted of the output of the data acquisition device, the voltage-controlled pressure regulator, the pneumatic actuator, the mechanical response of the embossing machine, and the load cell. Though some of these components were known, the T900X regulator in particular was treated as a black box. Due to early empirical experiments with the device, it was determined that the feedback controller plus the physical system were such that the system had an order 2 or greater and could be made to overshoot and oscillate on step commands.

The step response from the system, from voltage command into the pressure controller to voltage output from the load cell, is shown in Figure 4-11. From this response, the transfer function was estimated to be first order, and described as

$$G_{plant}(s) = \frac{0.937}{0.575s + 1} \tag{4.4}$$

Given that the system is predominantly first-order and well-behaved for the command scenarios realistic to embossing operation, the logical choice for a controller was proportional-integral, to improve transient performance and to remove steady-state error. Based on analysis conducted using root locus, the system was observed to have two poles: one slow pole (the actuator response pole) and one fast pole (the filtered measurement pole). The hardware filtering was of sufficiently small time con-

stant to be neglected. Because oscillation was more undesirable than slow response, to prevent it from occuring, the zero of the PI controller was placed between the origin (where the integrator would be placed) and the fast pole, creating a slow but controllable dominant real zero. Then, the resulting system behavior was a very fast but small magnitude oscillation, and a slow but large magnitude real response. Estimates for appropriate PI constants were recorded with the intention of tuning them on the physical system.

Then, because the dominant real pole was relatively slow (time constant $\tau \approx 2.5$s), feedfoward control was added. The filtered reference signal was passed forward with a gain of 1 and summed with the output of the PI controller. This served to improve the performance of the response without needing to increase the gain and induce overshoot, in practice "speeding up" the system's effective time constant. At this point, the estimated constants from the initial PI design were tuned, and appropriate gains were found to be $K_p = 2.5$ and $K_i = 1$.

Antiwindup was also implemented on the integrator, with limits of $\pm$400N. Antiwindup is critical in this application because of the nonlinearity of the blade flexure. As the embosser traverses from the fully open position to make contact between the platens, it must push against the weight of the structure, and it also encounters the stiffness of the blade flexure. However, the "zero force" point is taken just before compression starts—that is, the measurement of interest is not what the load cell sees, but rather the force that is applied to form the substrate, not to overcome any resistance forces in traversing to that point. Thus, the load cell measures a "negative" force (that is, subtracting the offset measured at the point of contact gives a force less than zero) when it is in the fully open position. Leaving the embosser in this fully open position while commanding a force of 0N causes the integrator to accumulate a great deal of error during idle periods. To limit that error, stragetic integrator resets were employed, as well as the antiwindup cap.

Figure 4-12 shows the implementation of the hot embosser's control loop, with feedforward and PI control, in the context of the entire process control loop.

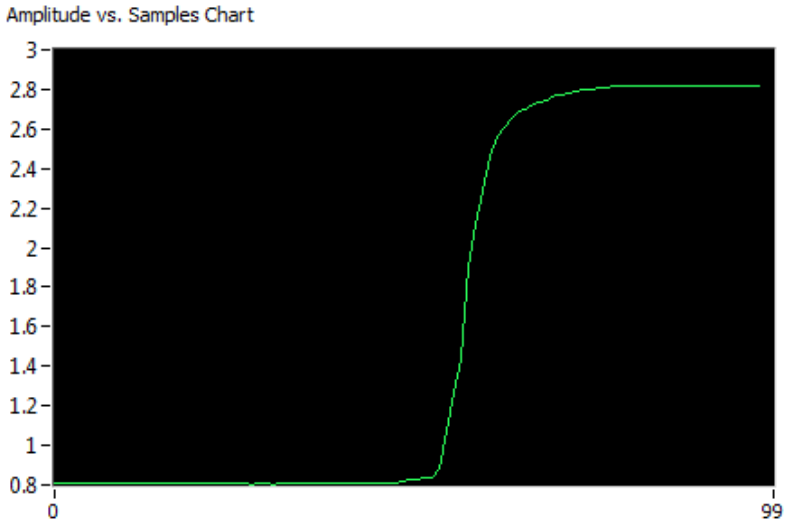

Figure 4-11: Step Response for the Actuation System: The step response looks dominantly first order. The horizontal axis is listed in samples; the sampling rate was 1ksample/s. The vertical axis is labeled in volts output from the load cell.

4.5 Pneumatic and Coolant System Design

A pneumatic management system was also necessary to support the hot embossing process, as pneumatic actuation was employed. In this system, compressed air is first filtered and regulated to 80psi. This air is then split into several branches. One branch is further regulated to 60psi, and provides airflow for the air bushing. Another branch is passed to the electronic pressure regulator, the ControlAir T900X. The output of the regulator then passes to a three-way solenoid valve. This valve either funnels air pressure into the actuator, or opens the actuator to the atmosphere to exhaust it. This was necessary in the initial design using the T550X, as it had a minimum output pressure of some 2psi, sufficiently closing the gap between the platens such that substrate insertion was difficult. However, this feature was retained for the T900X, which is a zero-range pressure controller, as a safety feature.

The coolant management system interacts with the third branch of the input air. This branch is regulated to 10psi and is passed through a two-port solenoid valve and a check valve into a junction with the water coolant system. This coolant is a water-glycerol mixture, maintained at room temperature using a VWR Recirculator chiller. The chiller is left open-tank so that when activated, air can be passed through

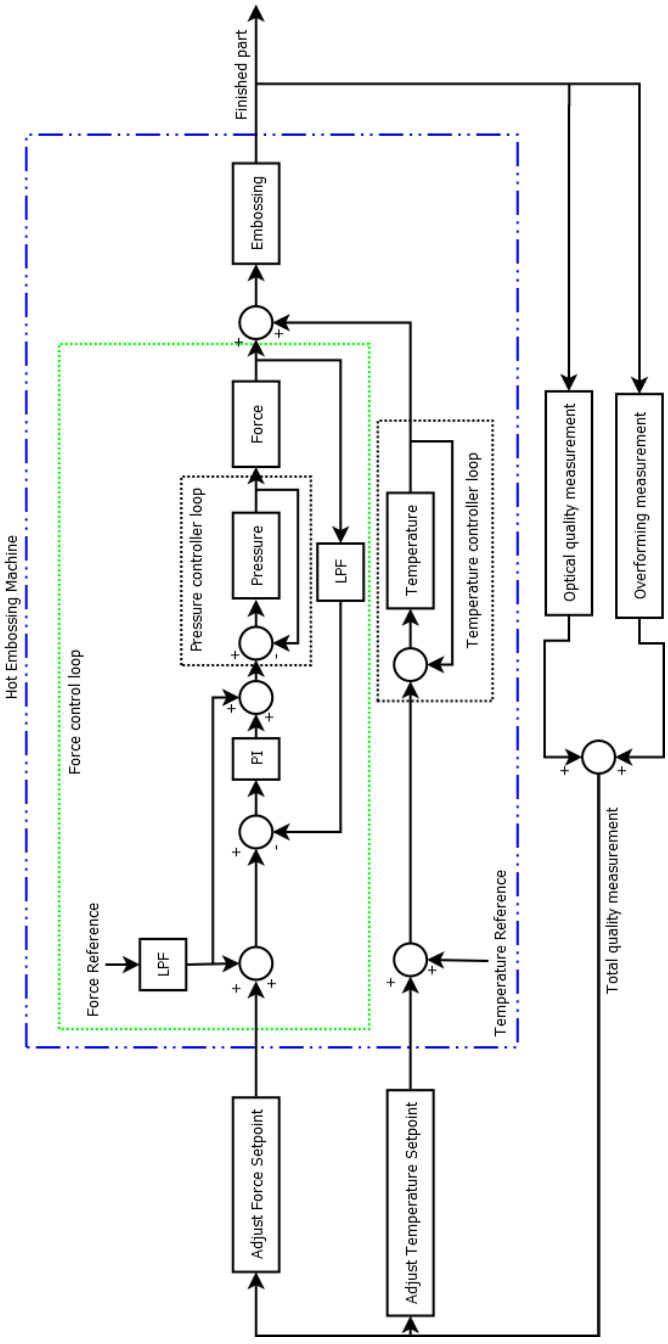

Figure 4-12: Microfactory Control Loop: Shown in the context of the entire microfactory loop, the loop relevant to the hot embosser is shown in the broken blue box. The structure of the force control loop is shown in the green dashed box. The two black dashed boxes indicate subsystems that have internally applied controls.

the embossers cooling system to force any coolant out of the cooling block to promote heating; the open tank is required for flow to be maintained instead of pressure built up in a closed tank. In addition, due to the low head pressure on the chiller's pump, air pressure is used to assist coolant flow into the hot embosser during the cooling process. An additional 3-way solenoid valve provides a bypass for the coolant flow to cycle it either through the hot embosser during cooling or to route it back through the chiller during heating and forming. The flow was routed back to the chiller because experiments determined that merely blocking the flow could cause enough pressure to build up in the line downstream of the chiller's magnetic drive pump that the pump would slip and the chiller would shut down in an error mode.

A diagram of the pneumatic and coolant systems is shown in Figure 4-13.

4.6 Tooling

The current tool used on the embossing machine was produced by Hennan, by embossing bulk metallic glass. First, a negative was etched into crystalline silicon. Bulk metallic glass was then heated to its glass transition temperature, and the crystalline negative was embossed into its surface. The metallic glass was then cooled, and the temperature profile carefully controlled. Finally the crystalline silicon was etched away [16]. This tool has proven to be extremely robust and durable, and has produced an estimated 1000 parts in its lifetime without showing any signs of wear measureable with a white light interferometer. This tool is shown in a photograph in Figure 4-14.

However, in the past, other tooling materials have been used, such as micromachined aluminum tools. The downside of the micromachined aluminum tools is their lower durability, and their relatively poor surface finish due to machining marks [33]. Hard resin tools have also been investigated, though it was found that selecting a resin that was both tough and rigid at high temperatures was difficult. Finally, soft tools constructed of PDMS have also been demonstrated to be effective, though these present somewhat different problems from rigid tools, and tend to exhibit more rounding of features during embossing.

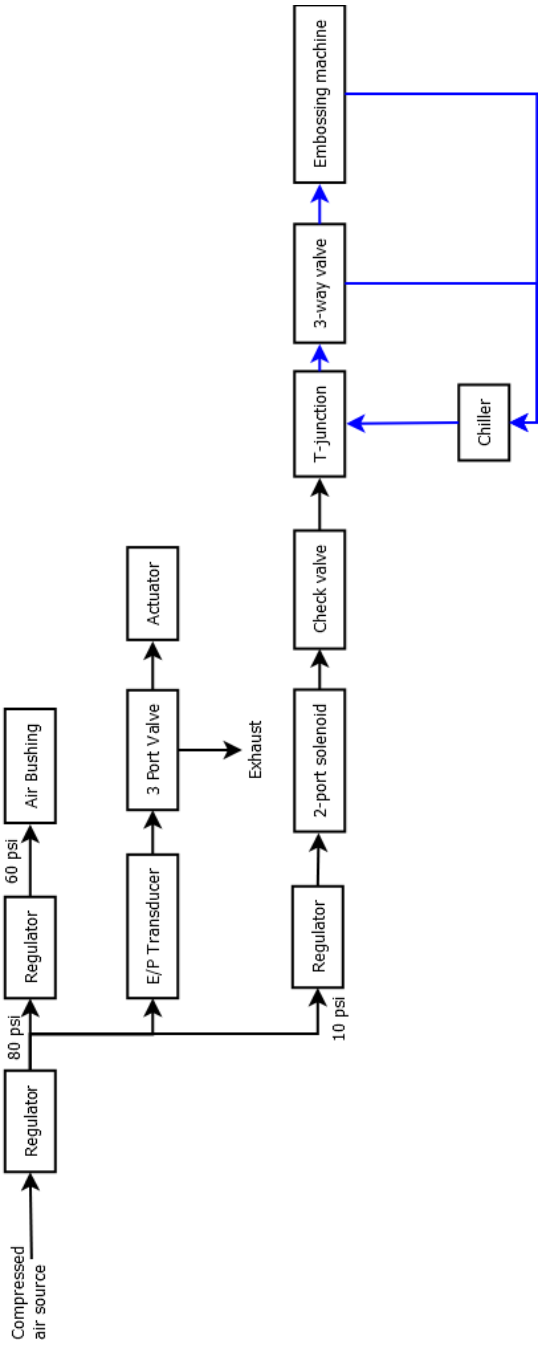

Figure 4-13: Schematic of the Coolant and Pneumatic System: This diagram indicates the flow path of the pneumatic and coolant inputs into the system. Black arrows indicate airflow only; blue arrows indicate the flow of coolant, potentially mixed with air.

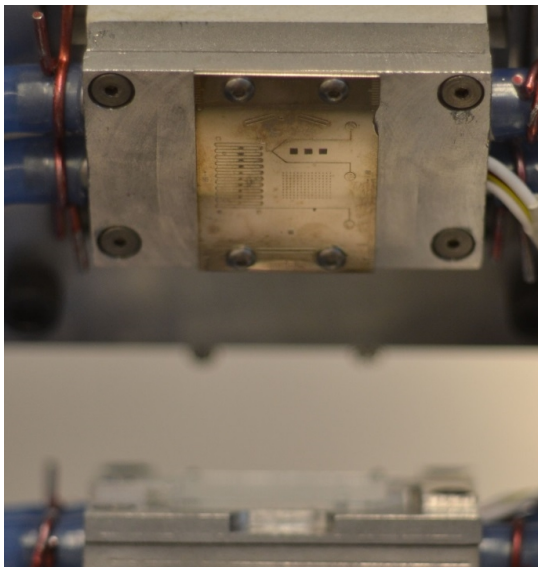

Figure 4-14: Bulk Metallic Glass Tool: Here the machine forming area is propped open in order to capture an image of the tool. The pattern on the tool is visible, as well as a blank substrate loaded onto the lower platen.

4.7 Performance of Precision Equipment

The final step is to quantify the performance of the machine. This takes the form of measuring the performance of the controlled parameters and comparing them to the desired values.

As for the thermal performance, both platens can be brought to within 3°C of a commanded temperature, but not at the same rate. This is because one heater is noticeably somewhat lower power than the other, measurable as an effective difference in resistance in an unpowered state; since the heater output power is controlled by switching a 120V AC power source on and off, at 100% duty cycle, the output power of one heater is given by:

$$P_{output} = \frac{V^2}{R} \Rightarrow P_{output} \propto \frac{1}{R} \tag{4.5}$$

The bottom heater was measured at 87Ω; the top was measured at 104Ω. This corresponds to a difference in power output of 16%, closely matching the approximately 20% slope difference in the linear temperature ramp-up shown in Figure 4-15. This asymmetry problem could be solved by acquiring more powerful heaters; the

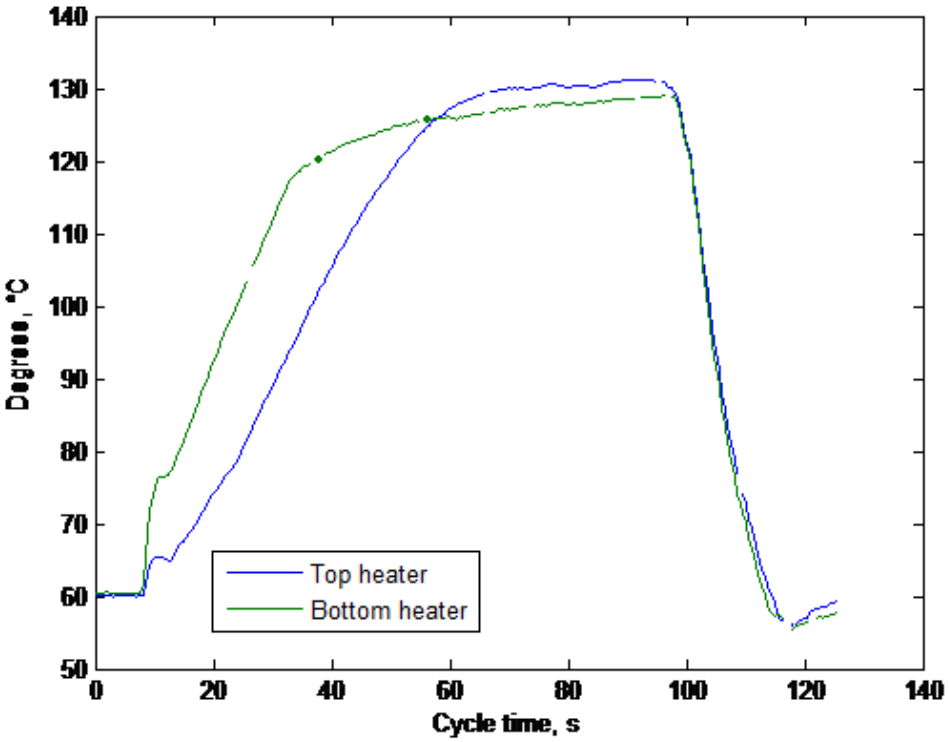

Figure 4-15: Heater Temperature Profiles During Production Cycle: One heater's temperature lags behind the other during ramp-up because of its lower maximum output power, but by the time forming begins at 60 seconds, the two heaters are within 3°C of each other.

heaters currently in use were chosen for their form factor, but were the lower-cost, lower-power option in that particular form factor. Additionally, utilizing more powerful heaters would allow for a faster temperature ramp-up, and reduce the primary contributor to cycle time, the heating stage. Another possible solution to improve symmetry is to constrain the power output to the bottom heater, but this has the downside of failing to decrease the time required to heat to forming temperature. Overall, despite design efforts to minimize asymmetries between the platens, at least some small thermal asymmetry remains; but, given enough time, both platens can be brought to symmetric forming temperatures.

The force command proved initially to be a difficult problem. Though the actuator was demonstrated to be highly linear in force output, the question remained if the actuator combined with all other electronic and mechanical system components would continue to have a linear output.

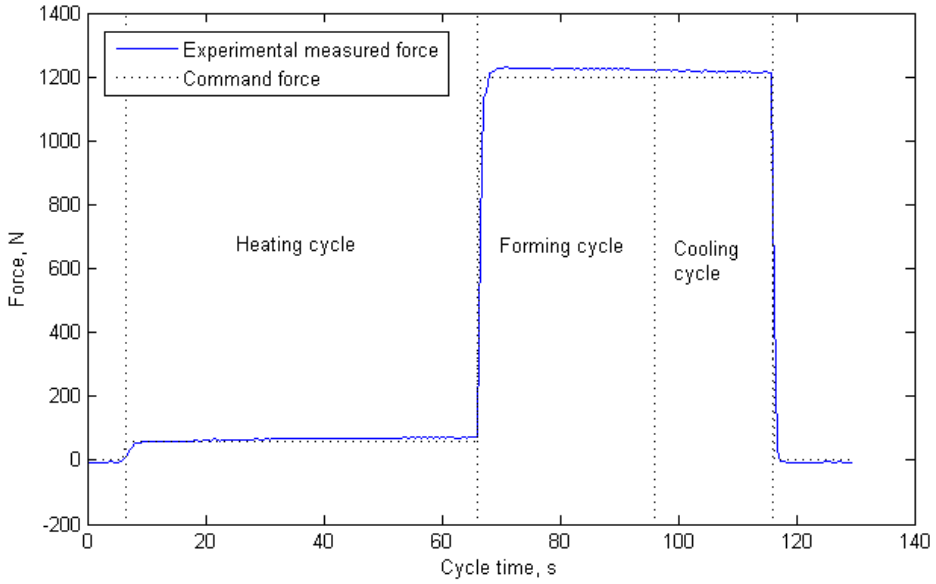

Figure 4-16: Measured Force Profile During Production Cycle: The force output follows the commanded force setpoint to within a few percent. The observed overshoot is possible due to several possible contributions, such as nonlinearities in the system, accumulated error in the integrator (capped by antiwindup), and unmodeled system behavior.

As shown in Figure 4-17, the output is highly linear after a certain point. Below this point, the guiding blade flexure makes a large contribution; as a beam constrained to be fixed at one end and to move in vertical motion at the other end, it a nonlinear stiffness in bending over large deformation, as determined by finite element simulations. As the platens close, the blade flexure moves into the neutral position and the small-deviation regime. In this regime finite element simulations show its stiffness contributions are small and relatively linear. Thus, to successfully utilize the actuator, it has been calibrated and designed to function in this linear regime of platen contact.

This force output has proven to be repeatable to within the minimum resolution of the load cell, approximately 2N. In addition the output has proven repeatable to within approximately 1% of the commanded setpoint under all environmental conditions, a significant improvement over pneumatic predecessors. The measured performance of the force application during a production cycle is shown in Figure 4-

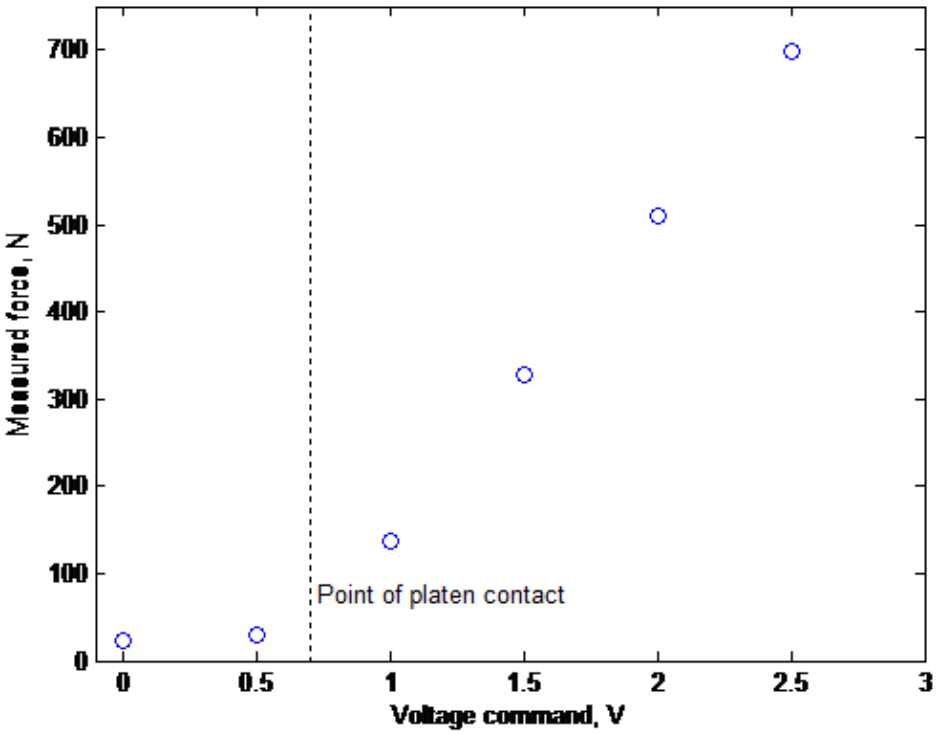

Figure 4-17: Measured Force for Voltage Command to Actuator: The actuator-sensor loop was designed and verified to be extremely linear in the regime in which it is in contact with the platens. However, before the platens make contact, nonlinearities in the system, such as the blade flexure at large displacements, give a nonlinear output.

16.

In summary, the machine performs at a high level, and is capable of meeting force setpoint commands to within 1%, and temperature setpoint commands to within 3°C. The actuator displays highly linear output behavior, and the process has been demonstrated to be in control even in nonideal circumstances. The equipment has been deemed sufficiently precise and well-controlled to be used as a platform to continue the study of the hot embossing process.

Chapter 5

In-Process Sensing

5.1 Possible In-Process Measurements and Relationship to Quality

During the course of the development of the precision hot embossing equipment in this thesis, it was noted that given that force measurement and temperature measurement were already implemented (and necessary for forming parameter control), the only other measurement required to be able to completely understand energy input into the process was a measure of displacement. Given force and displacement, the mechanical energy input into the system can be computed, as $W_{mech} = \int F dx$; and given temperature, the thermal energy input into the system can be determined, since $W_{therm} = \frac{mC_p\Delta T}{t}$. Thus, it was a logical decision to add a linear voltage displacement transducer (LVDT) sensor to the system in order to measure this quantity.

However, computing process input energy is not necessarily the most indicative measurement of the process to make. To wit, three measurements relevant to the process quality were identified and implemented.

The first is a measurement of the initial blank thickness. Since inconsistent material geometry is a large source of variation, as detailed in Chapter 1, knowing this measurement allows for future possibilities in optimizing the embossing process and controlling the temperature profile. (Because the force control is closed-loop, initial

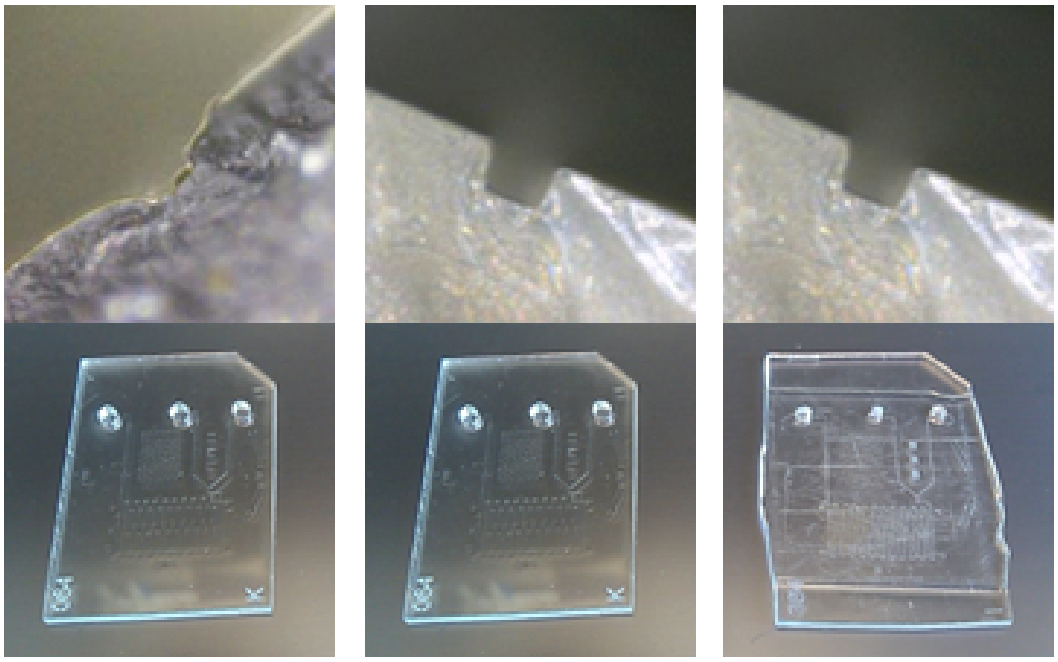

Figure 5-1: Underformed, Well-formed, and Overformed Devices: Shown here is an underformed device (left), in which the channels are not fully impressed into the substrate; a well-formed device (center); and an overformed device, in which the channels are well-formed but the macroscale appearance of the device is distorted and uneven [14].

blank thickness has no effect on the closed-loop force applied.) It also allows for an easy, automated means of collecting information on material variability, which is conceivably useful in finding or switching suppliers in a manufacturing environment.

The second is a measurement of the bulk deformation. The channel formation quality improves as pressure and temperature increase, as the degree of flow into the tool features increases, as explained in Chapter 2. However, this also causes flow outward on the devices unconstrained edges, creating large-scale deformation in a phenomenon deemed "overforming". The overformed devices have ragged, uneven edges, are difficult to register and seal with the adhesive tape cover, and are visually unattractive, as visible in Figure 5-1. Thus, it is important to optimize channel quality while preventing overforming from happening.

During embossing, large plastic deformations are incurred in the substrate. However, only a small portion of this deformation, approximately equal to the height of

the features on the tool, is the actual imprinting process of the features; the rest serves to squeeze bulk plastic flow out the sides of the substrate, and to stimulate flow into the fool features. The relationship between this area and the displacement of the platens is expected to be roughly quadratic, given the relationship

$$\frac{\Delta z}{z} = \frac{\Delta x}{x} = K\sqrt{\Delta A} \Rightarrow \Delta A \propto (\Delta z)^2 \tag{5.1}$$

where z is the compressed axis, x an unconstrained lateral axis, and K a resulting geometric constant. Thus, by measuring bulk deformation, an estimate of the degree of macroscale overforming can be made, and a second measure of quality contributing to the whole can be made. Though one could establish a continuum measure of overforming, it seems more practical to establish a binary threshold of "acceptable deformation" or "unacceptable deformation," based on visual inspection and registration testing of finished devices.

The third measurement of interest selected is the glass transition temperature. This is arguably one of the most important material parameters that could be detected: in order to ensure consistent material properties, the temperature setpoint is best made relative to the glass transition temperature rather than being absolute. As shown in Chapter 2, at the glass transition temperature, drastic changes in material properties, including sharp decreases in the elastic modulus and shear modulus, occur. Thus, if one of these properties, such as elastic modulus, is plotted versus temperature in-process, a sharp drop should be visible when the material reaches its glass transition.

Measurement of the elastic modulus would typically be performed by measuring the slope of a stress-strain plot during a compression or tension test; this removes any function of temperature and geometry from the results [29]. However, the forming cycle here is not an exact stand-in for a compression test: force and displacement are measured instead of stress and strain, and geometrical variations in specimens are not accounted for.

However, the elastic modulus is related to the measured quantities of force and

displacement, as well as the geometric quantities, in the relationship:

$$\frac{EA}{l} = K_{eff} = \frac{F}{\delta} \Rightarrow E \propto K = \frac{F}{\delta} \tag{5.2}$$

where E is the elastic modulus, A the area of compression, l the axial length beign compressed, and F and δ are force and displacement. Then, it is relatively straightforward to compute the stiffness at any point in time as F/δ, and plot it relative to the temperature at that point in time, to generate a stand-in curve for elastic modulus as a function of temperature. By detecting a precipitous drop in this plot of effective stiffnes versus temperature, the glass transition temperature can be estimated.

5.2 Hardware Implementation

The sensor package consists of an Omega LD500 LVDT and a Futek LTH300 load cell. The LVDT is attached to the moving shaft using a figure-8 shaped clamp. This clamp separates the LVDT from the active thermal area, preventing both thermal and electromagnetic interference from the high powered heaters, and providing spatial clearance for the device. The LVDT measures displacement between the shaft and the roof of the structure, as shown in Figure 5-2. Ideally the displacement measurement would be made directly between the two platens; however, due to space constraints and the high temperature fluctuation experienced by the platens, they serve as very unsuitable mounting points for any sensors. Thus, any displacement measured by the LDVT does include some machine thermal expansion and elastic deformation; however, these contributions are linear and easily predicted and removed from any data.

The load cell is a donut-shaped load cell with a through-hole. It rests on a button on a mounting plate on top of the pneumatic actuator, and on top of it rests the air bushing shaft. The load cell is not fastened to either of these surfaces, which prevents cross-loading on the system (as detailed in Chapter 4) and the load cell. The device is then capable only of measuring compressive forces; however, in this application, no

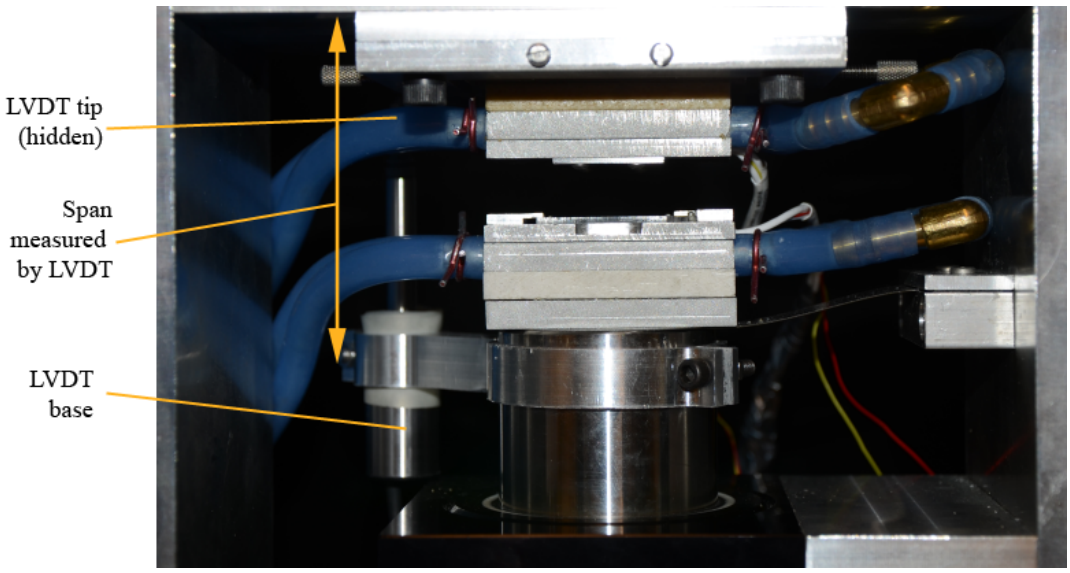

Figure 5-2: LVDT Contact Points: The orange arrow indicates the two points between which the LDVT measures displacement–i.e., the roof of the structure and the moving shaft. The two active thermal stacks and any deformation of the roof of the structure then are included in the total displacement measured by the LVDT. Note that because the clearance gap required for loading is larger than the LVDT's measured range, the LVDT is not in contact with the structure except for the final 1mm of its travel.

tensile forces are ever applied to substrates.

A Sola SDT-4-24-100RT 24V power supply provides a DC power signal for the sensors. The load cell is driven with 15V of power created using a voltage divider (maximum allowable 18V) [34], and the LVDT is driven with 24V (maximum allowable 30V) [35]. Driving with higher voltages increases the effective sensitivity of each measurement device, as the output gain of each device is proportional to the input voltage, and is thus desirable:

$$G = (V_{input}\text{V})\,(G_{native}\text{mV/V/N}) \Rightarrow G \propto V_{input} \tag{5.3}$$

The output signal from each sensor is passed into an AD620 instrumentation amplifier. The output of the amplifier is buffered using an LM324 operational amplifier to control impedance, as the AD620 is highly sensitive to impedance balance on its input and output pins, and then hardware low pass filtered using a 1kΩ resistor and a 0.1μF capacitor, to remove high-frequency electromagnetic interference absorbed by

the cables. These processed signals are then read by a National Instruments USB-6008 10-bit data acquisition device, and processed by the LabVIEW program that controls the machine.

5.3 LVDT Measurement Capability

The LVDT signal is amplified by 5.117 in the AD620, and at a 24V power signal the LVDT outputs 9.165mV/μm. The data acquisition device is capable of reliable resolving increments of approximately 5mV, so the LVDT is capable of measuring displacements down to approximately 0.5μm over a 1mm range. System noise measurements indicate the RMS noise to be approximately 0.2102μm.

The LVDT tip is not always in contact with the roof of the structure, however; due to the fact that a larger clearance than 1mm is required to insert blank substrates, the LVDT has a dead zone where it must travel through air before it makes contact with the roof and starts measuring displacement.

Figure 5-3 shows the measurement made by the LVDT during a production cycle. During the heating cycle, thermal expansion causes the LVDT to expand from its initial point of contact; then, as the material softens and the temperature stabilizes, the LVDT measures the platens beginning to close. During the forming cycle the step up in force creates a jump in displacement as well as a faster rate of deformation, visible as a steeper slope in the displacement curve. Finally, during the cooling cycle, the degree of thermal contraction of the machine plus the formed part is visible as the temperature drops to the demolding temperature level.

5.4 Force Measurement Capability

The instrumentation amplifier provides a gain of 225.5 to the load cell, which has an inherent output of 0.01497mV/N when driven with 15V, for a total output of 3.376mV/N. The detectible force range is approximately 2200N, with an output resolution of approximately 2N (again limited by the data acquisition device's resolution

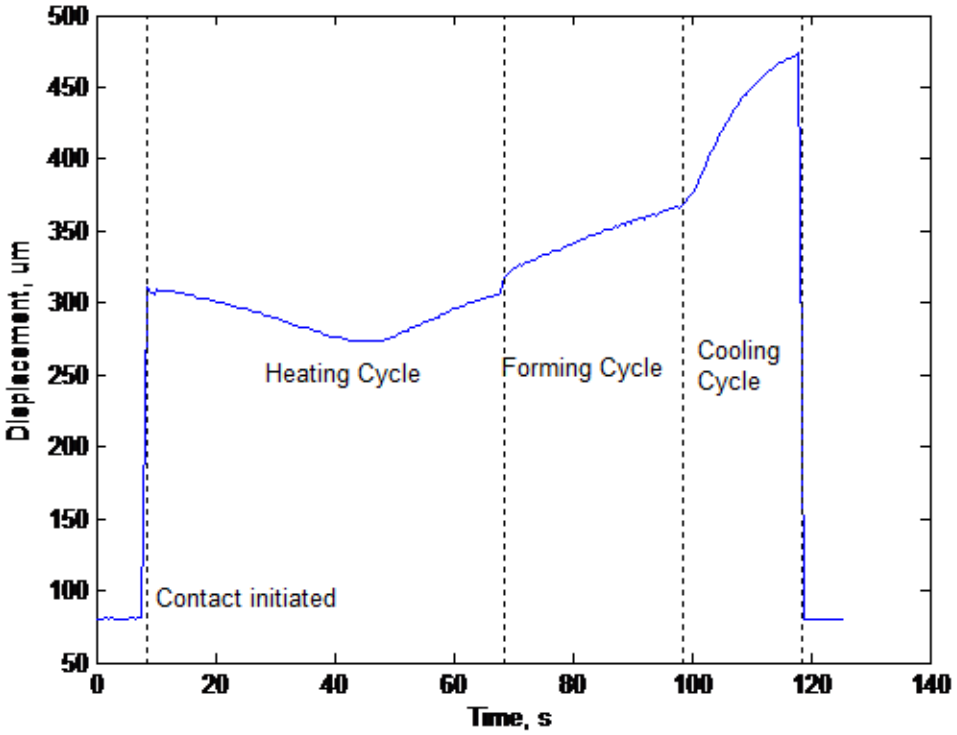

Figure 5-3: LVDT Output During Production Cycle: The LVDT provides a window into what is happening during the process. During the heating cycle, thermal expansion occurs, and then as the polymer reaches its glass transition temperature, imprinting begins; in the forming cycle, large deformations are imparted under high forces; and then in the cooling cycle, thermal contraction occurs.

of 5mV). Total system noise measurements indicate RMS noise levels to be equivalent to 0.8412N.

The load cell experiences some constant offset due to the weight under gravity of the components resting on it as well as due to resistive stiffness created by the blade flexure. The zero point from this offset is computed under gravity at the point where the flexure is at a neutral position but no force is applied to the platens; essentially, all non-forming forces are calibrated out. An example measurement made by the load cell during a production cycle is shown earlier in Figure 4-16.

5.5 Relevant Measurements and Data

By combining the measurements made from the LVDT, the load cell, and the thermocouples, the measurements listed in section 5.1 can be accomplished in-process with no additional steps required. This allows the cycle time to remain at its minimum, and for process physics to be measured without any disturbances being imparted to production.

5.5.1 Initial Blank Geometry

To measure the initial blank thickness, a simple algorithm is applied. As soon as a nonzero contact force between the platens is detected, the displacement measurement is made, i.e.:

$$\delta(t_{F>0}) - \delta_{offset} = \delta_{blank} \tag{5.4}$$

A known fixed offset between the tip of the LVDT and the machine structure (the dead zone) is subtracted, and the remainder is the blank thickness when the tool first makes light contact.

In practice, this measurement is limited by the sampling rate of the process. The initial electronic system design was not created with measurement in mind, so some components and processes, such as the heater controllers, impose rate limitations on

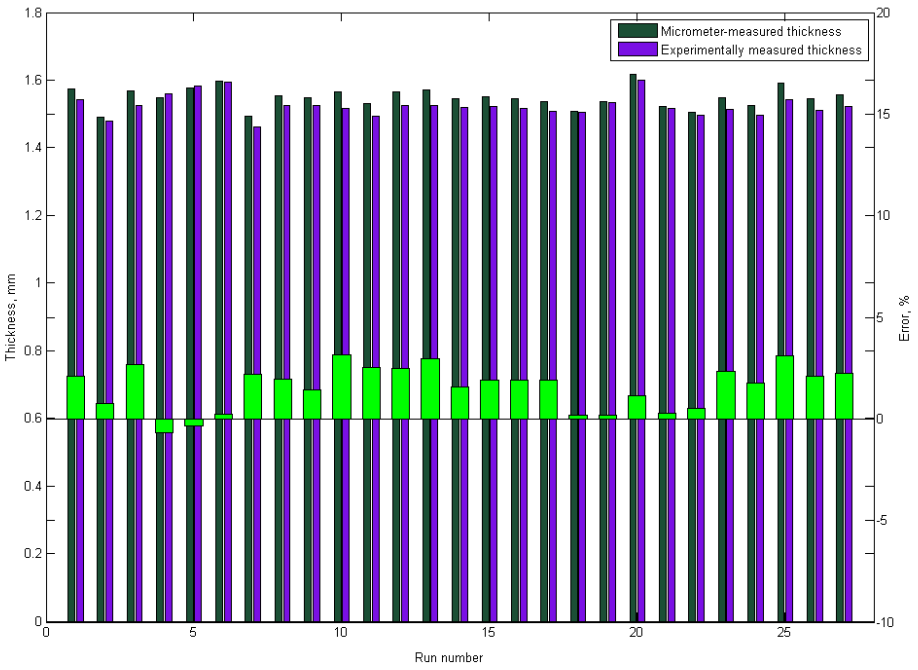

Figure 5-4: Accuracy of Initial Thickness Measurement: Here, automated measurements are compared to manual micrometer measurements (the dark green and purple bars and the left axis), while the percentage error is also displayed for each measurement (light green bars and the right axis).

how fast the measurement can be made. This means that the moment of initial contact tends to be missed, and a subsequent post-contact, light-compression displacement, smaller than expected, is detected instead. Even under these conditions, however, the measurement has been shown to be able to automatically detect the initial part thickness to within 4% error, as shown in the data in Figure 5-4. The fact that error is almost always positive (i.e. the initial thickness measured is smaller than expected) also supports the theory that the measurement is capturing a compressed thickness instead of an initial thickness. It is expected that with a faster sampling rate this error would decrease.

5.5.2 Bulk Deformation

The algorithm to measure bulk deformation is also relatively straightforward. Ideally, deformation from the first moment the tool contacts the substrate until demolding would be measured, to track both the initial imprinting deformation as well as excess deformation. However, first contact occurs during the heating stage, when the temperature is being ramped up, and the blank substrate as well as the thermal stack is experiencing significant thermal expansion (as visible in Figure 5-3 above). Since the LVDT measures the displacement outside the thermal stack, this expansion appears in its measurement along with any elastic deformation experienced by the machine structure. These effects mask the deformation of the part, and though they could be estimated and calibrated out of the measurement, the quality of this estimation is unlikely to be high.

Thus, the bulk deformation measurement is best conducted in a constant temperature environment; the force profile may however be arbitrary, as the resulting displacement is taken to be directly related to the overforming, without any dependence on the force profile. Fortunately, during the forming cycle, the temperature is held constant while a high forming force is applied. Thus, to gain some measure of overforming, the displacement over the forming cycle is monitored.

To experimentally validate the expected correlation, substrates were imaged before and after forming, and an image processes code implemented in LabVIEW was used to measure the area of the irregular shape. However, this measurement was somewhat noisy and highly dependent on the ambient lighting conditions, as is visible in Figure 5-5. Even so, the correlation is strong, exhibiting an R^2 value of 0.78, and validating the expected quadratic relationship.

It is thought that this correlation can be used to establish a binary threshold for acceptable or unacceptable levels of deformation by visually inspecting each formed device and essentially drawing a vertical line on the plot in Figure 5-6 to bound it into two regions. During forming, this limit could either serve as a stop—the forming cycle could be aborted at that point and transitioned into the cooling cycle—or it

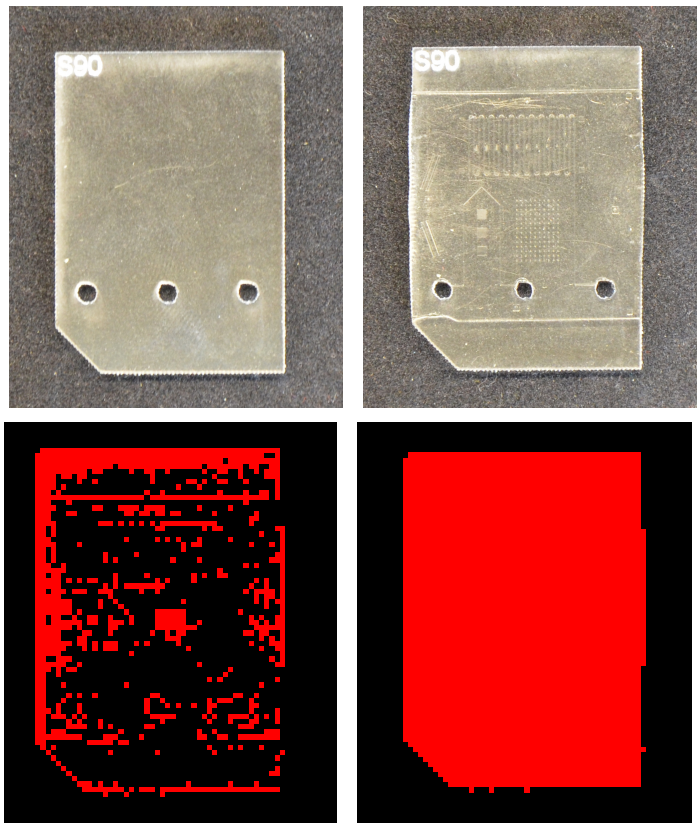

Figure 5-5: Images Taken for Optical Area Measurement: From left to right: an image of a blank substrate before forming; an image of the same substrate post-forming, with some overforming visible on the edges; an image of the substrate, thresholded; and a filled image of the substrate so area may be computed. The resulting area of the substrates is highly sensitive to the threshold level, down to even 2% changes in the level; any variations in light level make changing this threshold level necessary and induce noise.

could be a signal to switch to displacement control and hold displacement constant.

5.5.3 Glass Transition Temperature

Measuring glass transition temperature has proved the most complex of the three selected measurements. This is in part because the computation of effective stiffness does overlook some relevant quantities, i.e. that the geometry of the part is changing and that the force applied is not applied over a blank area but rather is an aggregate measure of force applied over a tool with raised features on its surface. Thus the effective stiffness computation is at best an estimate, made because it is quick, simple,

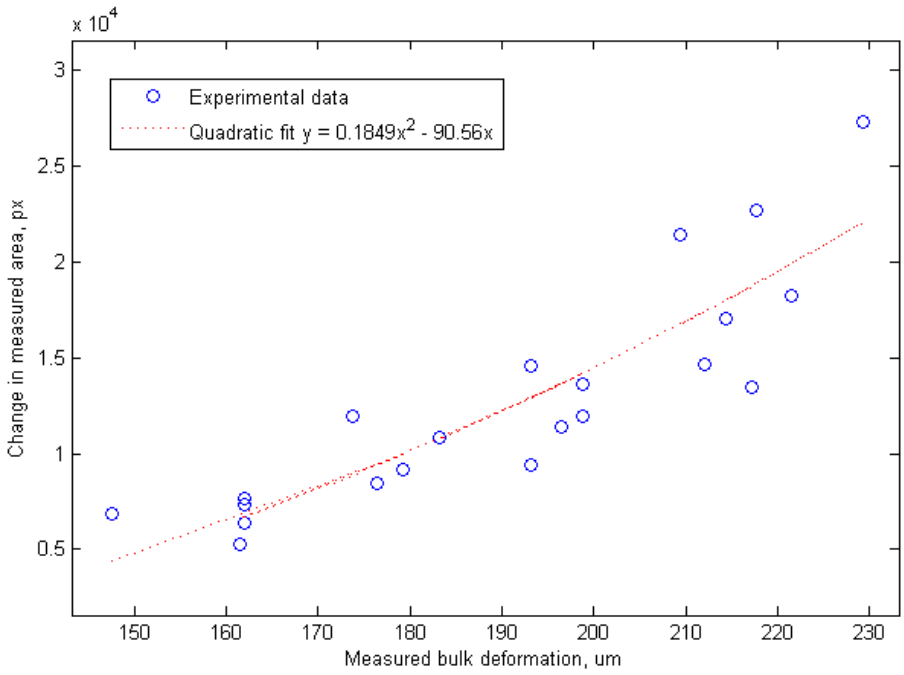

Figure 5-6: Correlation of Bulk Displacement Measurement with Area Measurement: The bulk deformation measurement matched the expected quadratic relationship fairly well.

and because its ingredients are available at hand.

Another issue with measuring the glass transition temperature is that it requires a ramping temperature profile. Again, fortunately, the conditions in the heat stage exactly match the necessary conditions: force is held constant, while temperature is ramped up from below to above the glass transition. However, the stiffness also relies on the displacement measurement, which is polluted by the measurement of thermal expansion and some small elastic deformation of the structure during the heating stage.

Even so, it was found that even with the uncertainty in the computation of effective stiffness, a visible sharp decrease was clearly visible at temperatures corresponding to the expected glass transition temperature in multiple experimental repetitions; one set of data is demonstrated in Figure 5-7. A positive slope before the inflection point provides a point of some debate, as for bulk material one would expect a downward slope at all points (the stiffness is always decreasing as temperature increases, as per

Figure 2-2). There are several possible contributors; one is that though the data were calibrated to remove thermal expansion offset, the estimate was not entirely accurate, and some remained. Another possibility is that during this process the polymer was softening, and the raised features were sinking into its surface; as more of the bulk of the surface contacted the flat plane of the tool beyond the raised features, the apparent stiffness of the material would rise, even as its material properties were changing to decrease that stiffness. Further investigation into this phenomenon is needed to better understand what processes are at work. In addition, determining an algorithm to automatically and accurately detect this inflection point is still in progress and has not been fully implemented.

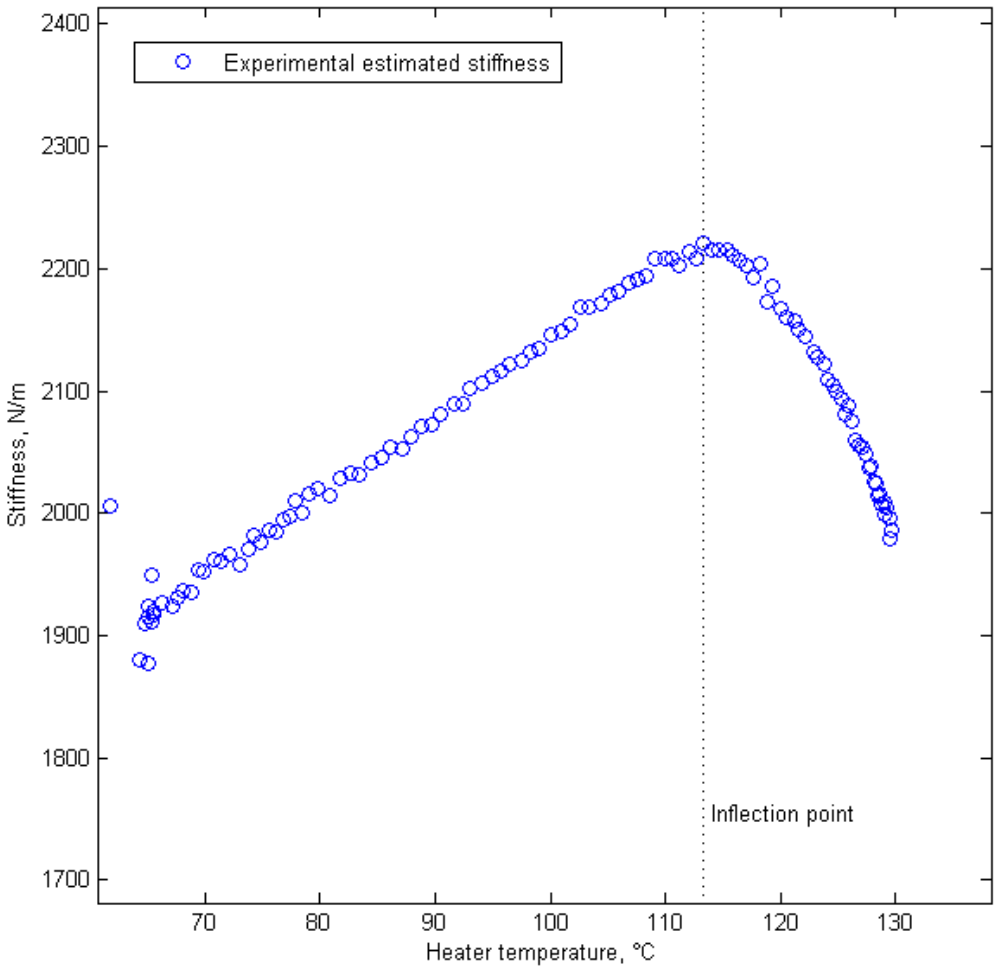

Figure 5-7: Experimental Data Measuring Effective Stiffness: The inflection point is clear in both the experimental data; the glass transition temperature is estimated at 115°C as indicated by the dashed vertical line.

Chapter 6

Conclusion

6.1 Thesis Contributions

The microfactory project set out to study the process of hot embossing as applied to microscale polymer fabrication in a manufacturing environment. To this end, precision equipment had to be developed that could support these efforts. This equipment needed to provide a high degree of repeatability, low machine variability, precise control of forming parameters, and a low cycle time for product formation. Building on the process knowledge developed by previous generations of hardware, one major contribution of this thesis was the design and construction of a new generation of precision embossing equipment. This equipment demonstrates superior parameter control and repeatability, and is the starting point for ensuing process control efforts.

An additional contribution of this thesis is the outfitting of the precision equipment with additional sensors. This allows for measurements of quantities and phenomena relevant to the process to be made in-process with no modifications to the cycle. These quantities can help define finished part quality, and provide further opportunities to explore process control and refine the embossing process.

6.2 Utility of Work

In conversations with industry representatives and microfluidics device designers, a frequent question is whether the design of this machine is scalable. The testbed design of only a 2.5cm by 2.5cm square area enforces space constraints on designs, and many designers seek to use emboss larger areas, either to make larger designs, or to make many devices in parallel.

One additional benefit of this design, as mentioned briefly in Chapter 4, is that it is completely scalable. The current design applies up to 2000N force over an area of some 6.25cm^2, for an averaged pressure of 3.2×10^6Pa. Though force is the controlled parameter, since it is applied over a fixed area, pressure is essentially directly controlled, and is more fundamental to the forming process (which depends on stresses). Thus, to achieve the same pressure capability (and thus the same forming quality) over the area of a microscope slide (approximately 19cm^2), one would need to be able to exert approximately 6.2kN of force. Similarly, for a credit-card sized area (approximately 46cm^2), one would need to exert approximately 14.8kN.

The work detailed in this thesis was designed for a 2kN maximum load. To be able to form these larger areas which are desirable for industrial production, the machine would need to be scaled. Fortunately, all aspects of the mechanical design are scalable:

1. The current selected actuator, the Firestone Airstroke 131, has a maximum force output of 6kN; however, it is one of the smallest available models. For example, the Firestone Airstroke 115 has a maximum force output under the same conditions of 15.8kN. Other Airstroke models have force capabilities of up to 3.5MN, far exceeding any foreseen actuation demands [36].

2. The force sensor was selected to match the required force output range; load cells with capabilities up to 90kN and beyond are commercially available to match the upgrade in actuator capabilities [37].

3. The air bushing and shaft diameters were chosen for their stiffness and for the

large mounting area on the top of the shaft. Given that the design is intended to prevent transmission of cross-loading to the shaft, there should be no reason even at higher actuator forces to need to upgrade the stiffness of the shaft; however, larger air bushings are also commercially available, with corresponding increases in stiffness [38], if larger cross-loads were to be anticipated. The addition of a simple adapter on the top could make the forming area as large as necessary.

4. The machine structure, an O-frame, is also scalable. Because the deformation of the O-frame, which consists of tensile stretching of the legs and 3-point bending of the crossbar, is completely symmetric around the forming region, the magnitude of the deformation is not important provided it is small enough to avoid excessive stresses in the structure and to avoid confounding any displacement data measured. By making the members thicker, or by constructing them out of a stiffer metal such as steel, the stiffness could be increased against the larger force load and kept in this regime of "small enough," and the maximum deformation of approximately 10μm could be maintained as the device was scaled.

5. For an increase in platen size and thus heater power needs, larger and higher-power heating units are available on the market, such as the 2kW Watlow CER-1-01-0006 model [22]. These slim-profile heaters could also be tiled to cover an even larger area if necessary.

6. If a larger platen were required to be cooled, the incoming coolant could be branched and passed through multiple U-bends, keeping the local cooling profile identical to that demonstrated in finite element simulations in Chapter 4.

7. No changes to the LVDT sensor should be necessary unless a larger displacement range must be measured; in that case, commercial solutions with larger sensor ranges are available, such at the Omega Engineering LD640-150, which features a 150mm range [39].

The greatest difficulty in scalability is parallelism of the platens. In this design, parallelism was achieved by using CNC-machined flat surfaces, and a planarizing

layer of epoxy. Over the small forming area in this design, the flatness achieved by CNC-machined surfaces was sufficient to minimize the force disparity between any two imperfectly parallel formed edges. However, as the area increases, any small tilt or deviation in machined surfaces propagates, and magnifies the force disparity between two edges. The author speculates that should this design be scaled even up to credit-card size, innovations in achieving and maintaining parallelism either passively or actively would be necessary.

6.3 Future Work

Possible transfer or expansion of this design to industry is one avenue of future work to be addressed. Interest has been demonstrated by some industry groups for the niche in their product lines that this machine fills.

The main task of the future work involving this system is to integrate it into the microfactory and fully automate the embossing process. In the final version of the factory, each step in the production of a part will involve a separate autonomous module: a dispenser for blank substrates; the embossing machine; a machine that applies and trims tape; and finally a machine that images and functionally tests finished devices. An Epson commercial robot will perform materials handling, and transfer the parts between each step. A central controller computer will receive signals from each module and trigger events in the cycle as needed. This module will also read in quality measurements from the testing device, and pass along adjustments to the forming parameters to the embossing machine. In this way closed-loop cycle-to-cycle control will be established.

Additional work to accomplish this objective will necessitate analysis of variance for each system component. Additionally, the relationship between forming parameters and quality measurement parameters will need to be established and quantified, in order to implement a mathematical or logical control algorithm to maintain quality. Once these steps are complete, tests demonstrating disturbance rejection and maintenance of part quality under varying conditions can be performed, and the goal

of achieving and demonstrating closed-loop cycle-to-cycle control can be completed.

Appendix A

System Circuit Diagrams

Below in Figure A, the circuit conditioning the sensor signals is diagrammed. This circuit was enclosed separately from other subsystems. Two AD620 instrumentation amplifiers are used to amplify the signal, and LM324 operational amplifiers are used to control impedance on the bias adjustment and output pins of the instrumentation amplifiers. An additional buffer controls impedance for the LVDT power supply. Conditioned signals are then routed into the National Instruments USB-6008 data acquisition device.

In Figure A, the circuit providing power to all system components and the instrumentation circuit is diagrammed. This circuit was also enclosed separately from other subsystems. 120V AC power is converted to a 24V DC signal. This signal is used as a power source for LM324 operational amplifiers which invert and offset the switched DC signal created by the heater controllers. Additionally, a noninverting operational amplifier configured to have a gain of 2 converts the 0-5V output signal from the data acquisition device to the range of 0-10V required by the E/P transducer. Power for the solid state relay board is provided by the power output on the data acquisition device.

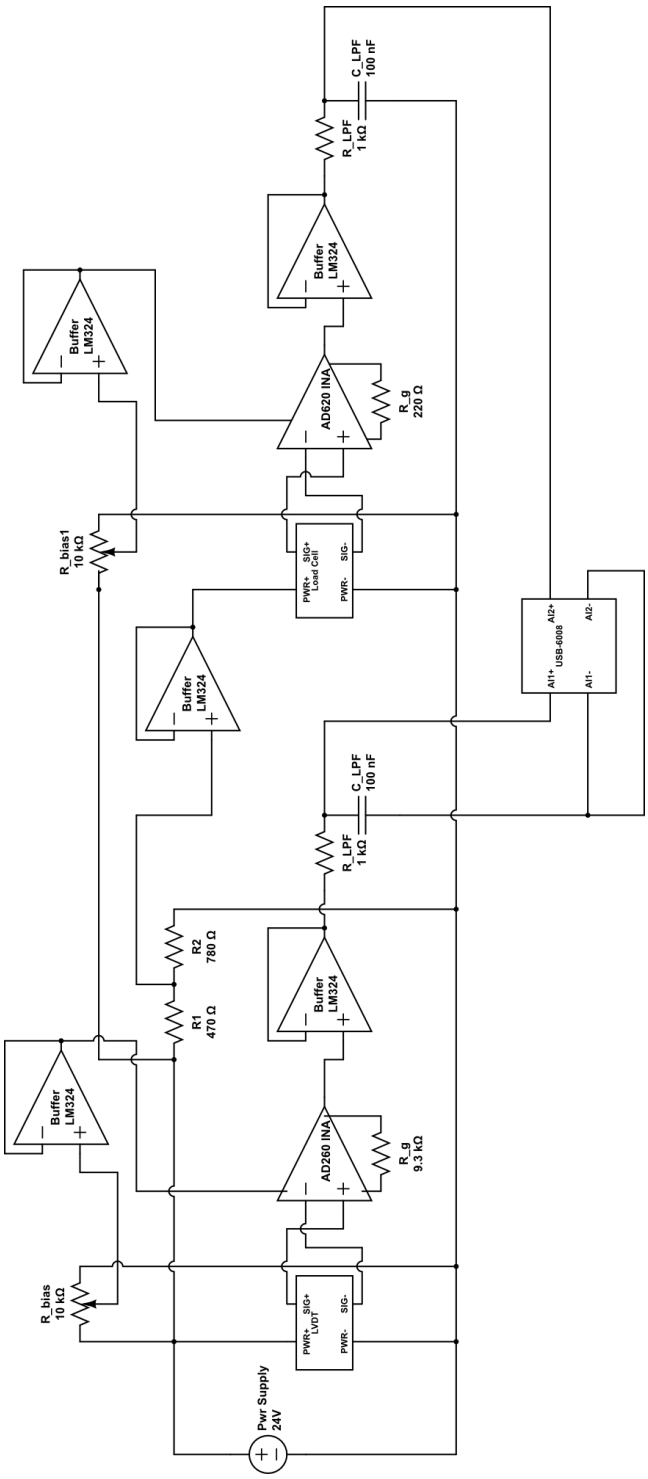

Figure A-1: Instrumentation Circuit Diagram: This diagram shows the implementation of the circuit linking the sensors to the data acquisition device. The circuit signals are amplified, filtered, and then passed to a data acquisition device.

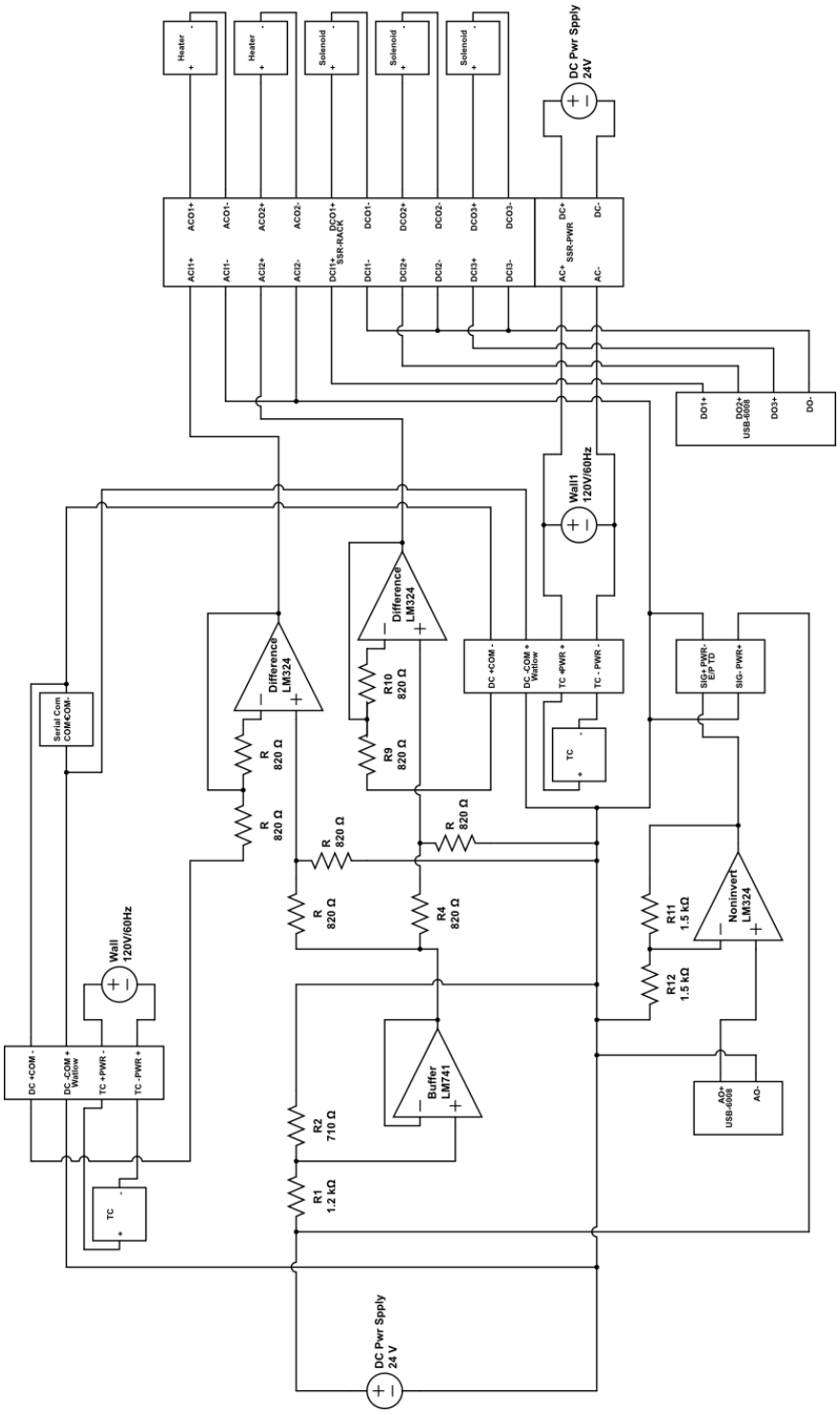

Figure A-2: Power Electronics Circuit Diagram: This diagram shows the implementation of the circuit providing power to all system components as well as the instrumentation circuit. 120V AC and 24V DC signals are used as main power lines. Signals from the data acqusition device and the heater controllers are conditioned and passed to solid-state relays to control hardware components.

Appendix B

System Diagram

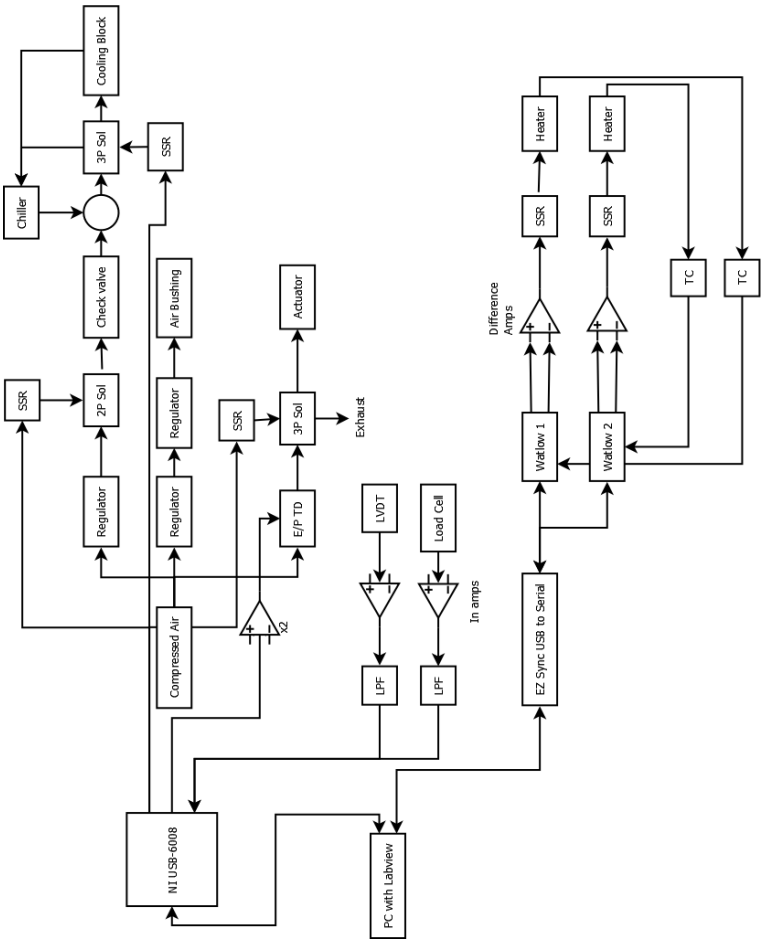

Figure B-1: Schematic of Complete System: Here the entire system is diagrammed, showing connections between the pneumatic, coolant, electronic, and mechanical components.

Appendix C

Engineering Drawings

Following are included engineering drawings for all components fabricated by the author. Components that were not fabricated by the author are:

1. The insulation blocks; as they required diamond tooling, Jaco Products was contracted to fabricate them.
2. The 2in diameter shaft was only post machined.
3. The air bushing and mounting block were not fabricated.
4. All sensors and actuators were purchased components.

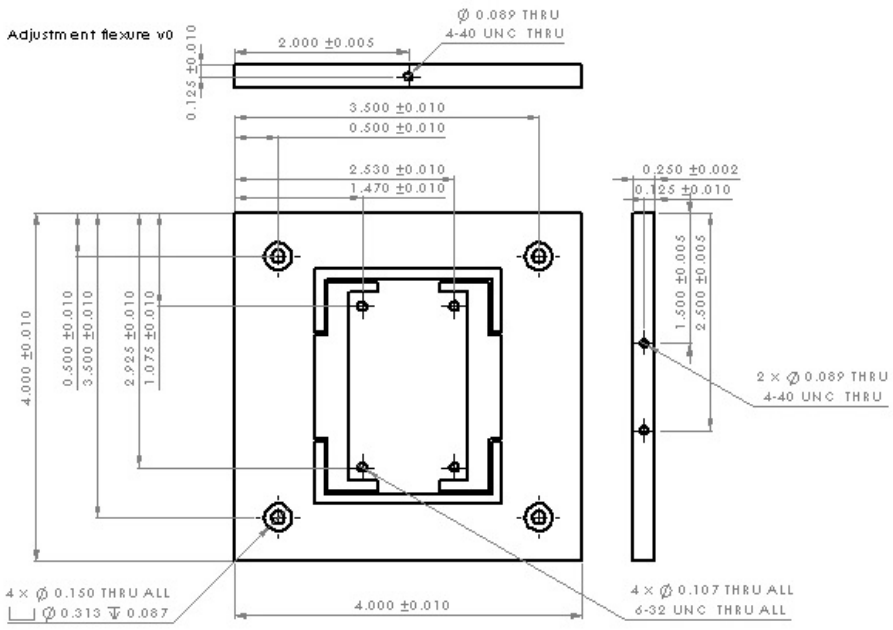

Figure C-1: Planar adjustment flexure.

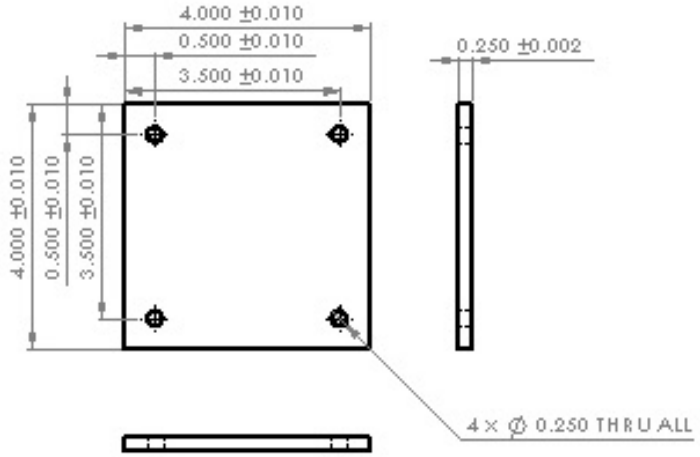

Figure C-2: Structural spacer plate mounted on the ceiling of the O-frame.

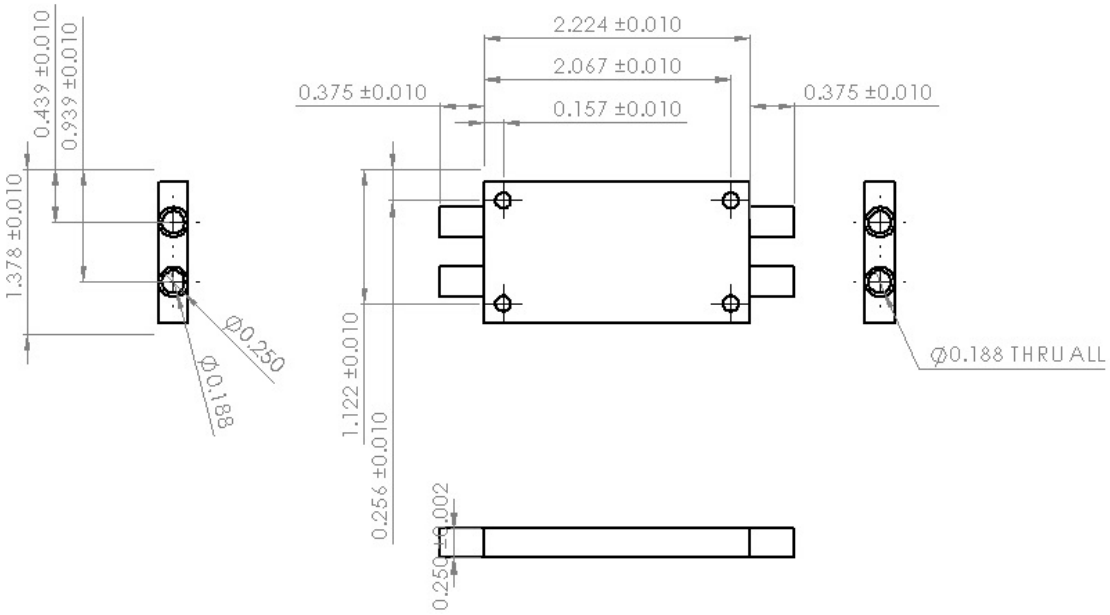

Figure C-3: Bottom cooling block.

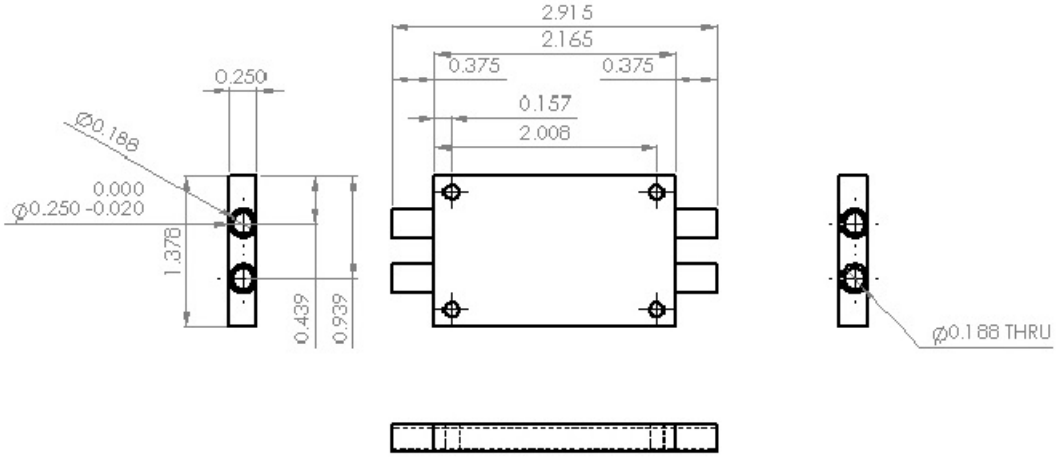

Figure C-4: Top cooling block.

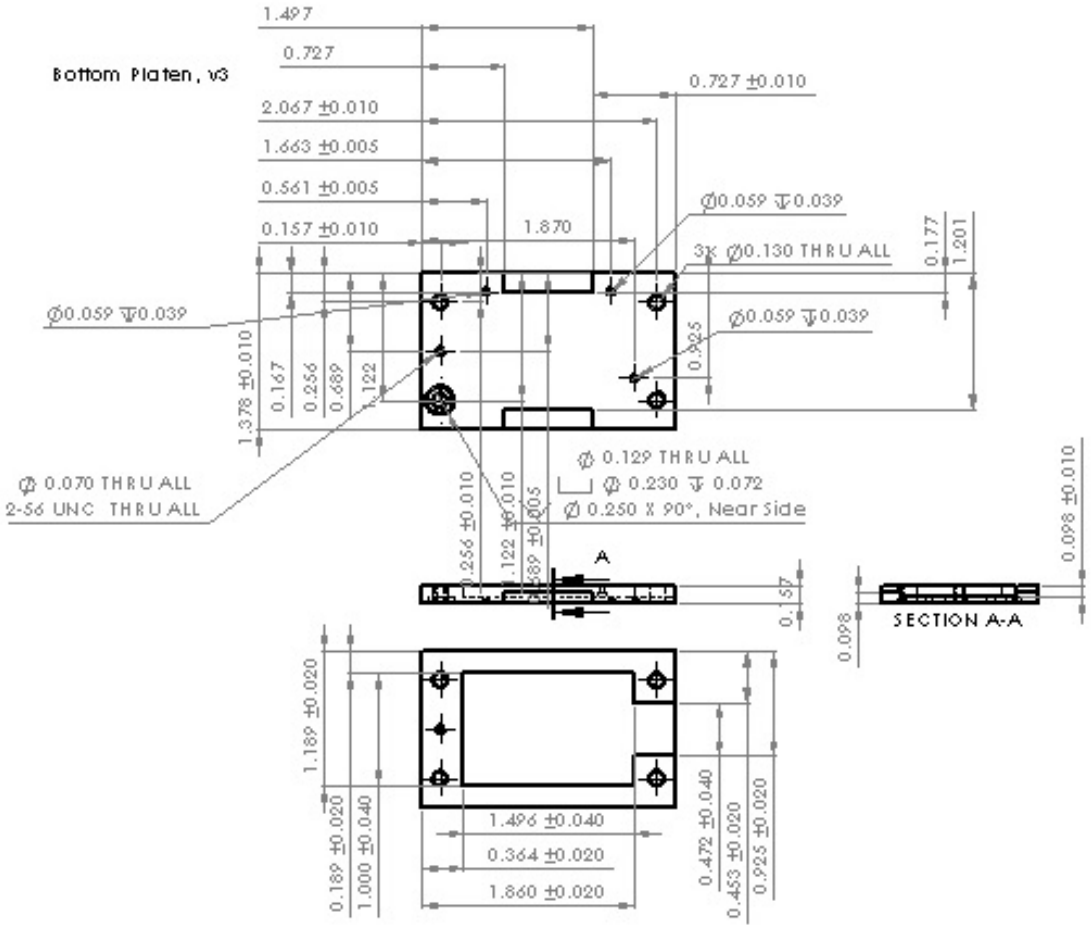

Figure C-5: Bottom platen.

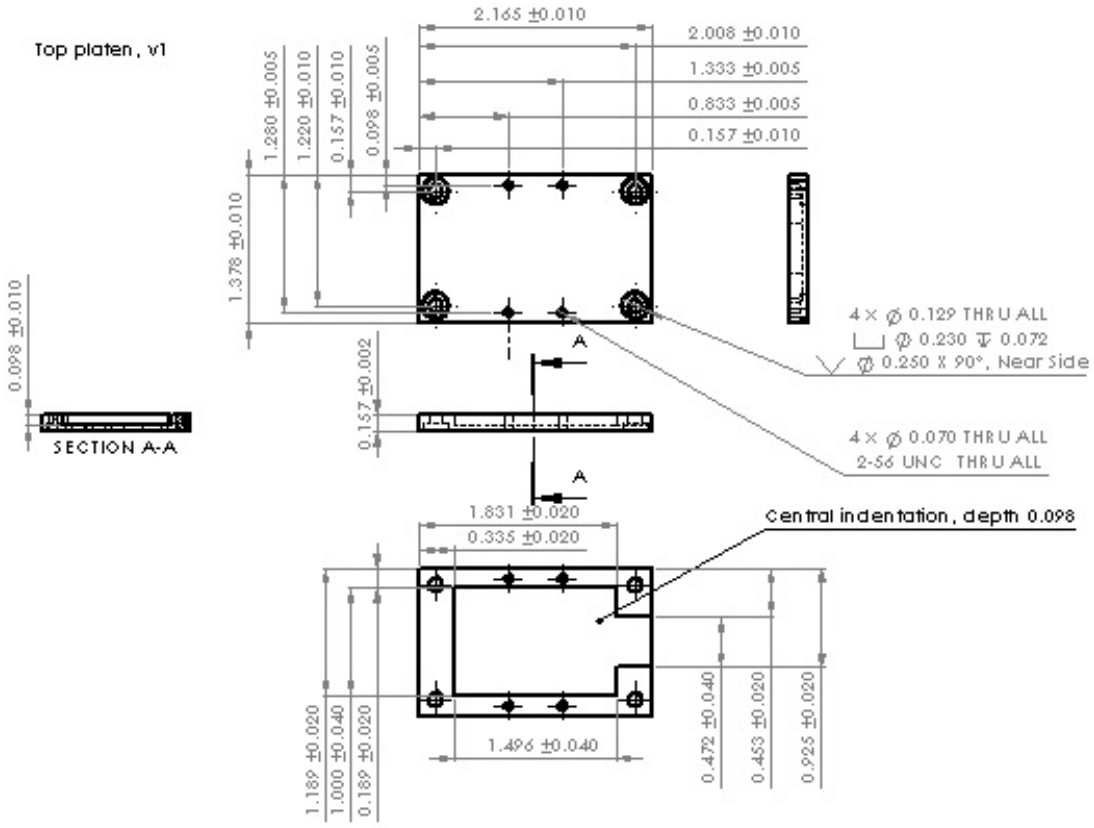

Figure C-6: Top platen.

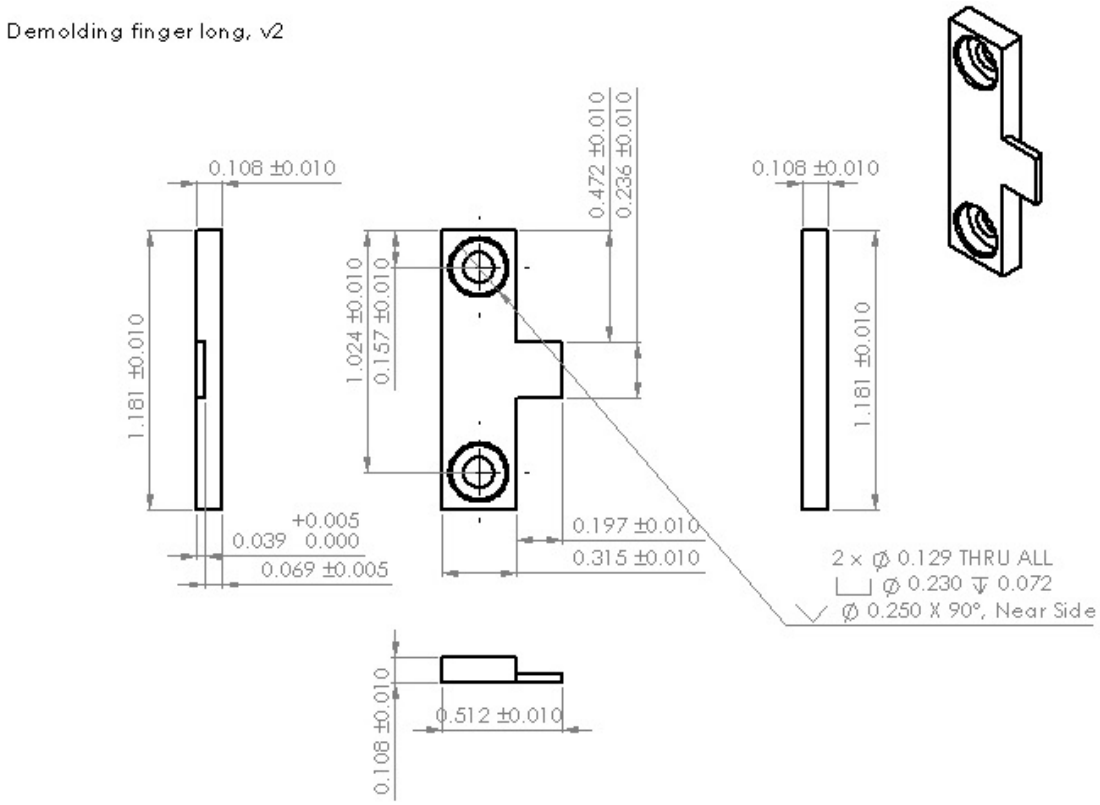

Figure C-7: One of the two demolding tabs.

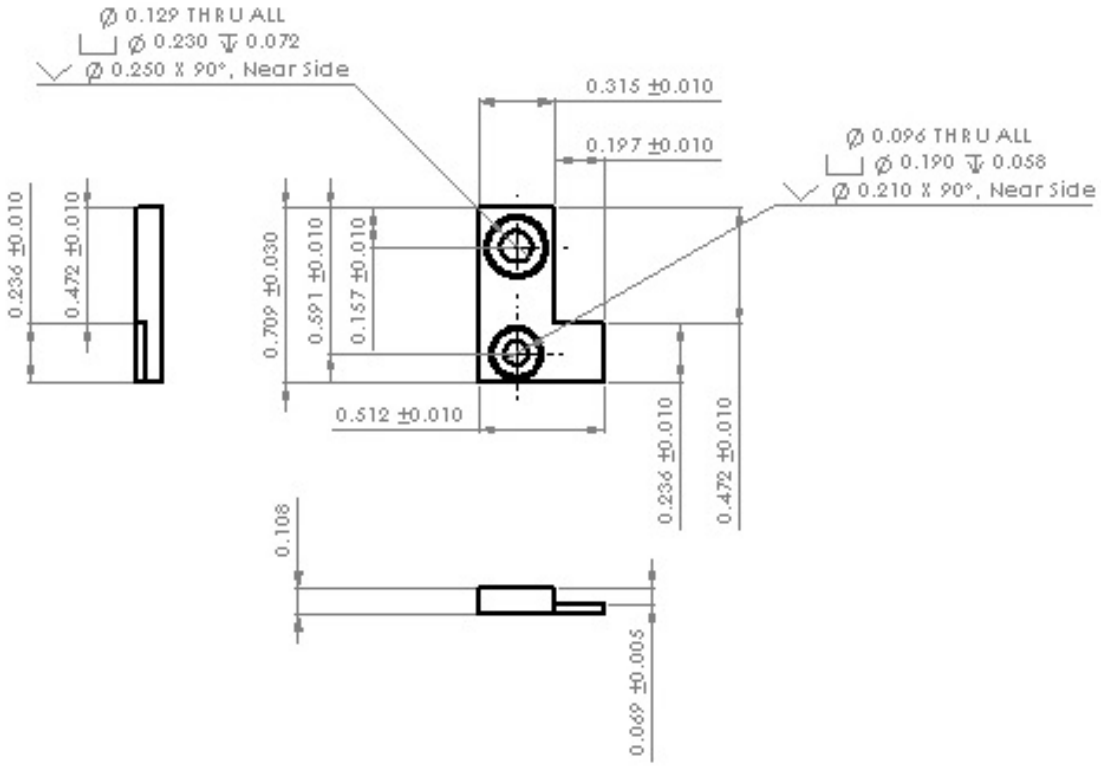

Figure C-8: The second of the two demolding tabs.

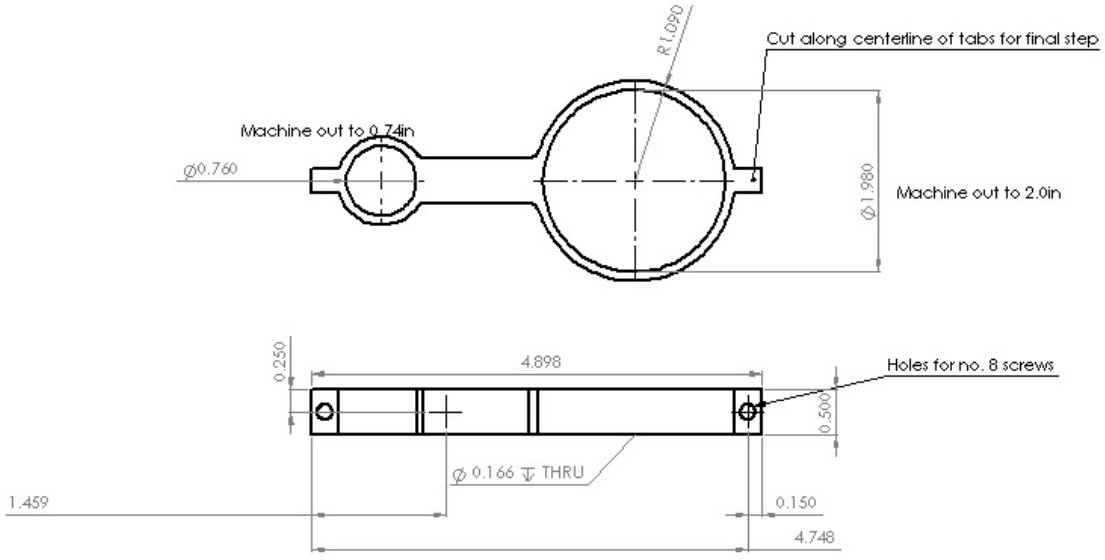

Figure C-9: Figure 8 shaped LVDT clamp.

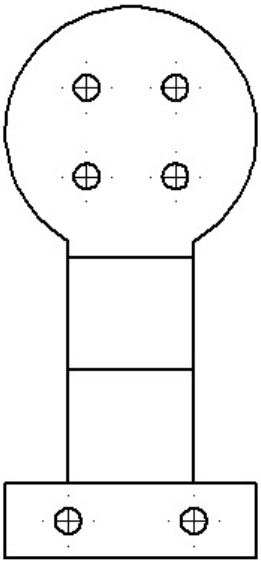

Figure C-10: Guiding blade flexure that prevents axial rotation of the shaft.

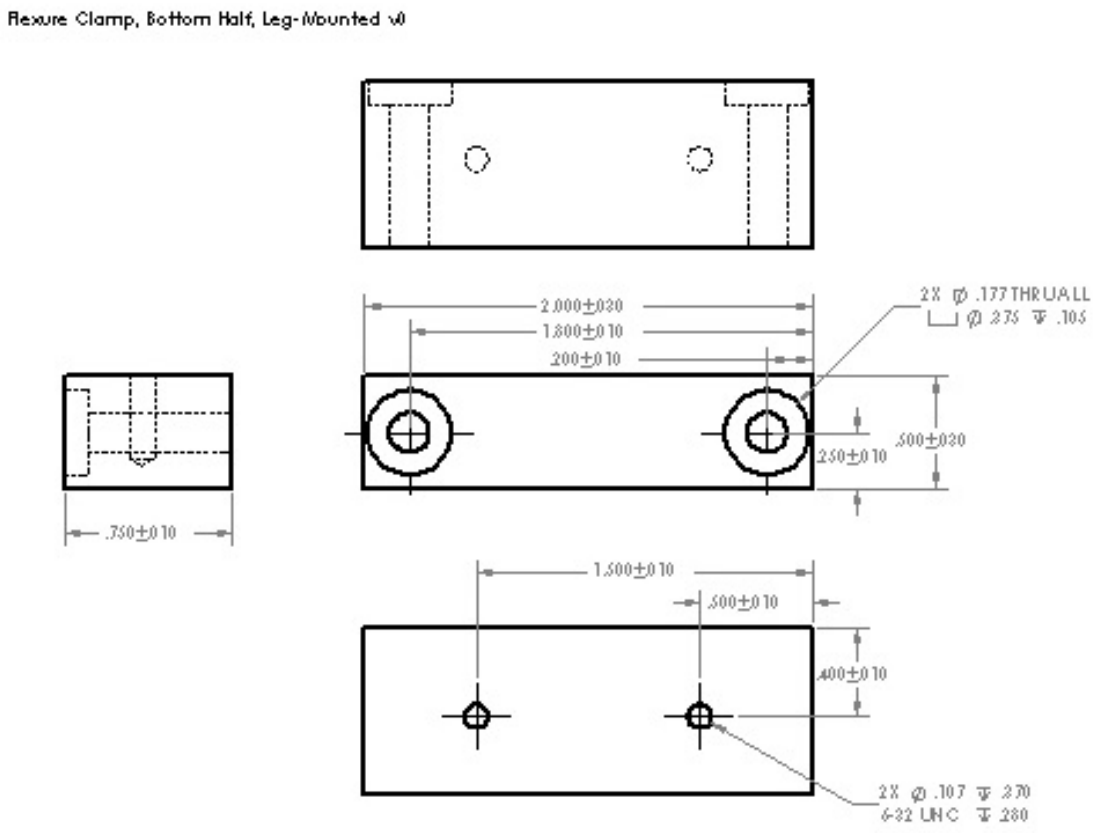

Figure C-11: The bottom piece clamping the blade flexure to the O-frame.

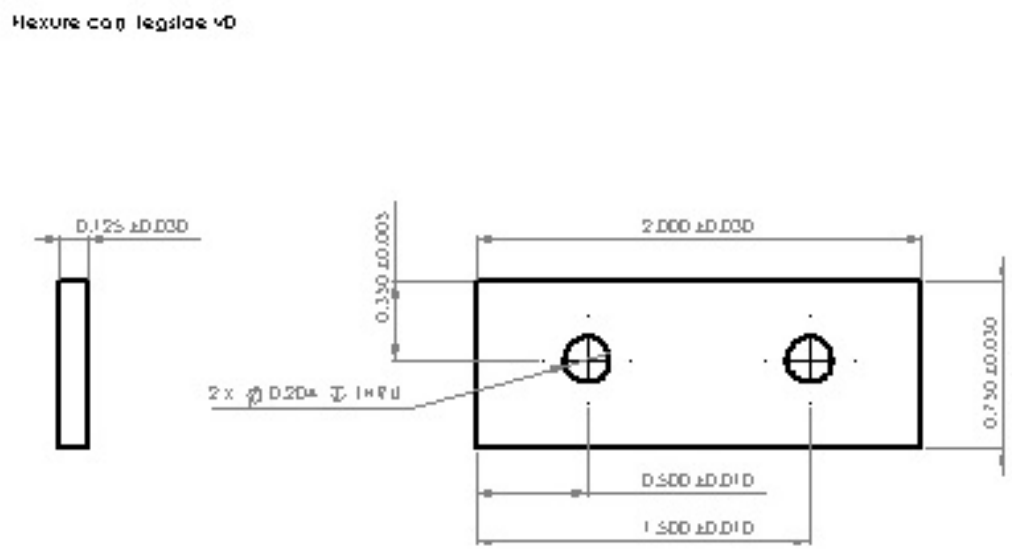

Figure C-12: The top piece clamping the blade flexure to the O-frame.

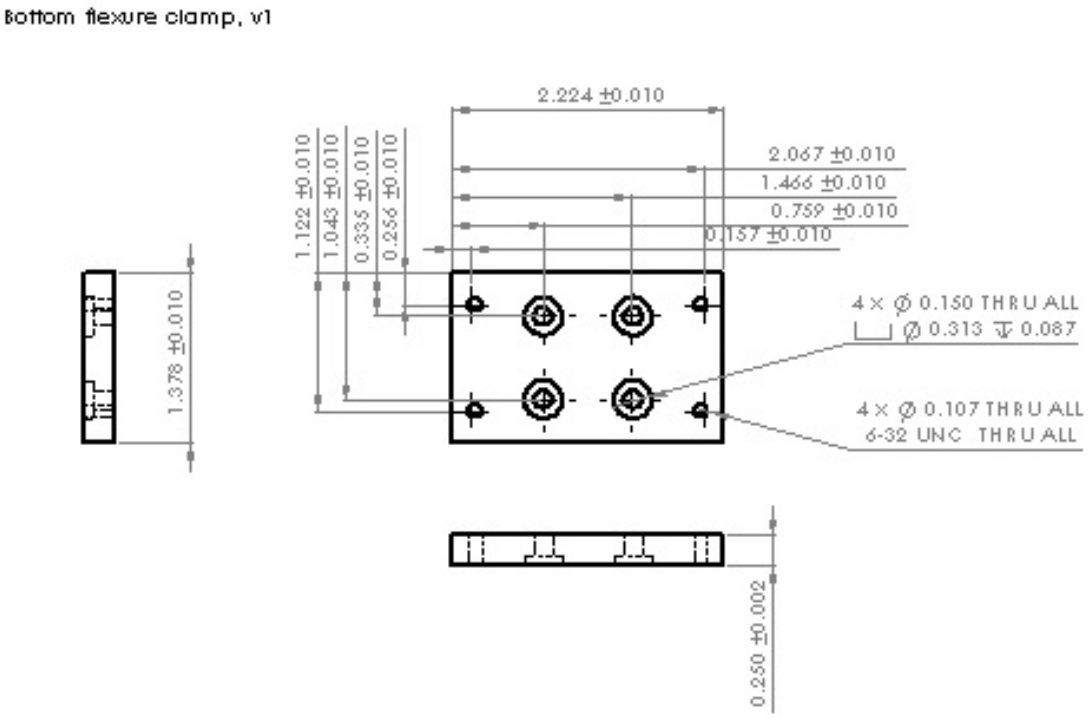

Figure C-13: The structural piece clamping the flexure between the bottom thermal stack and the shaft.

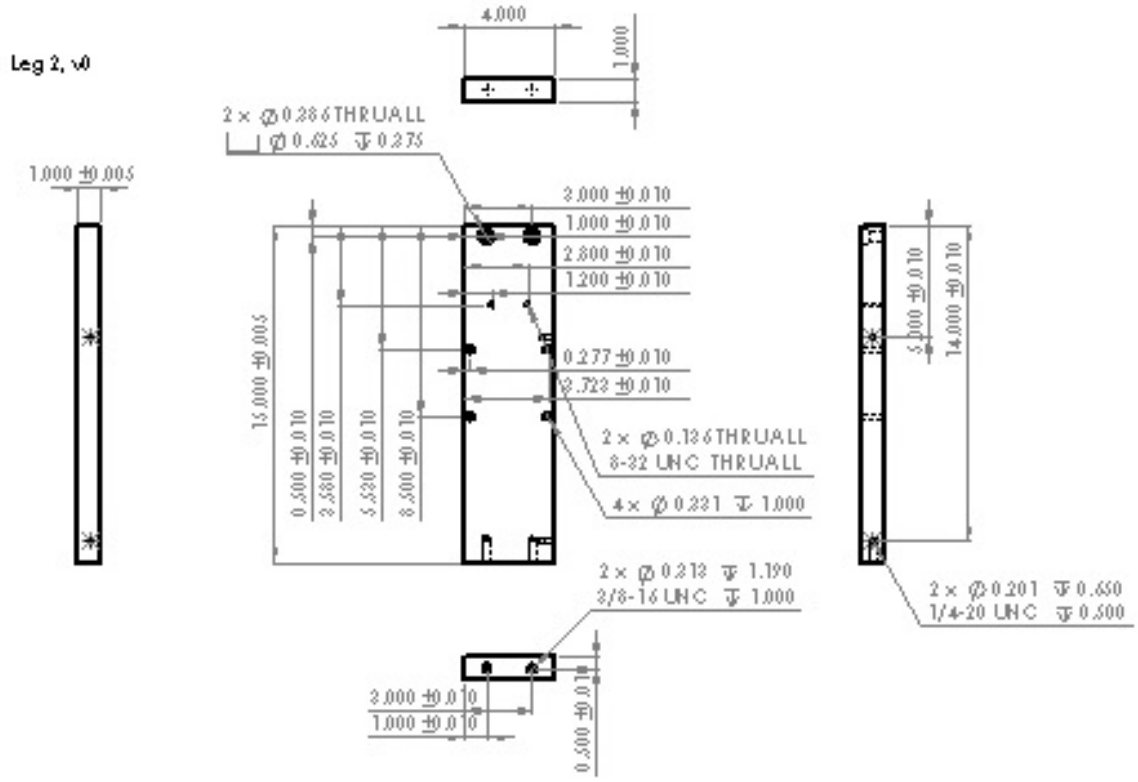

Figure C-14: The O-frame legs. Note that on one the two smallest holes are not featured.

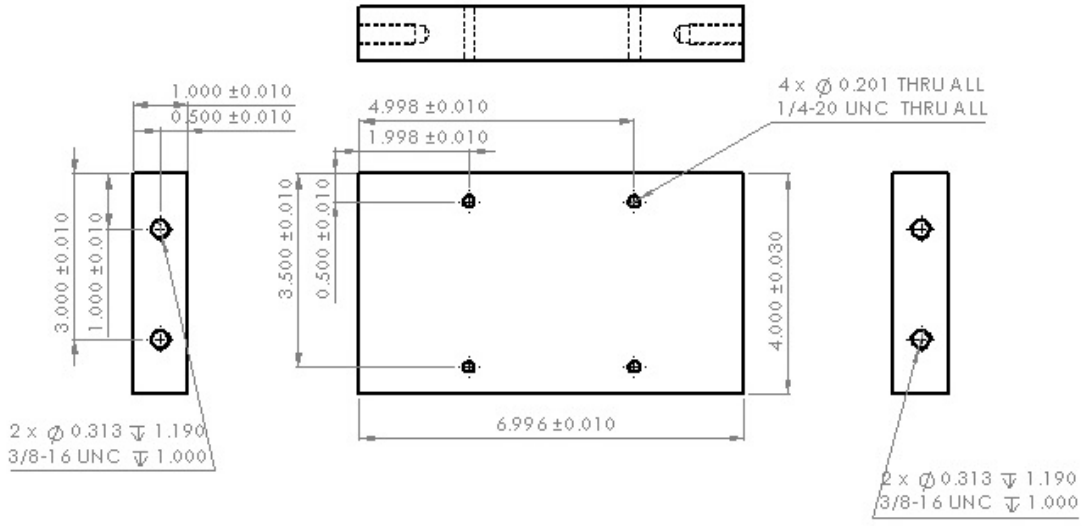

Figure C-15: The top crossbeam of the O-frame.

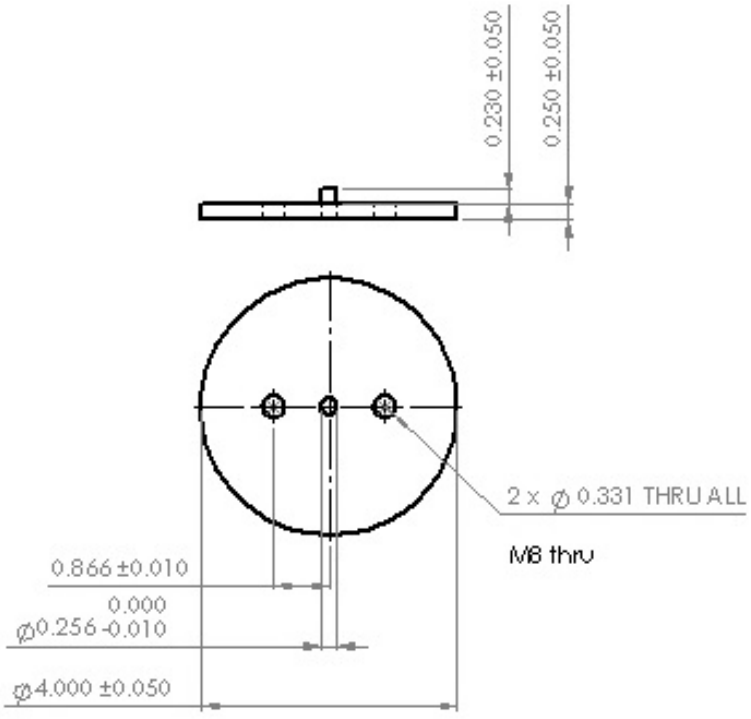

Figure C-16: Cap for Firestone Airstroke actuator.

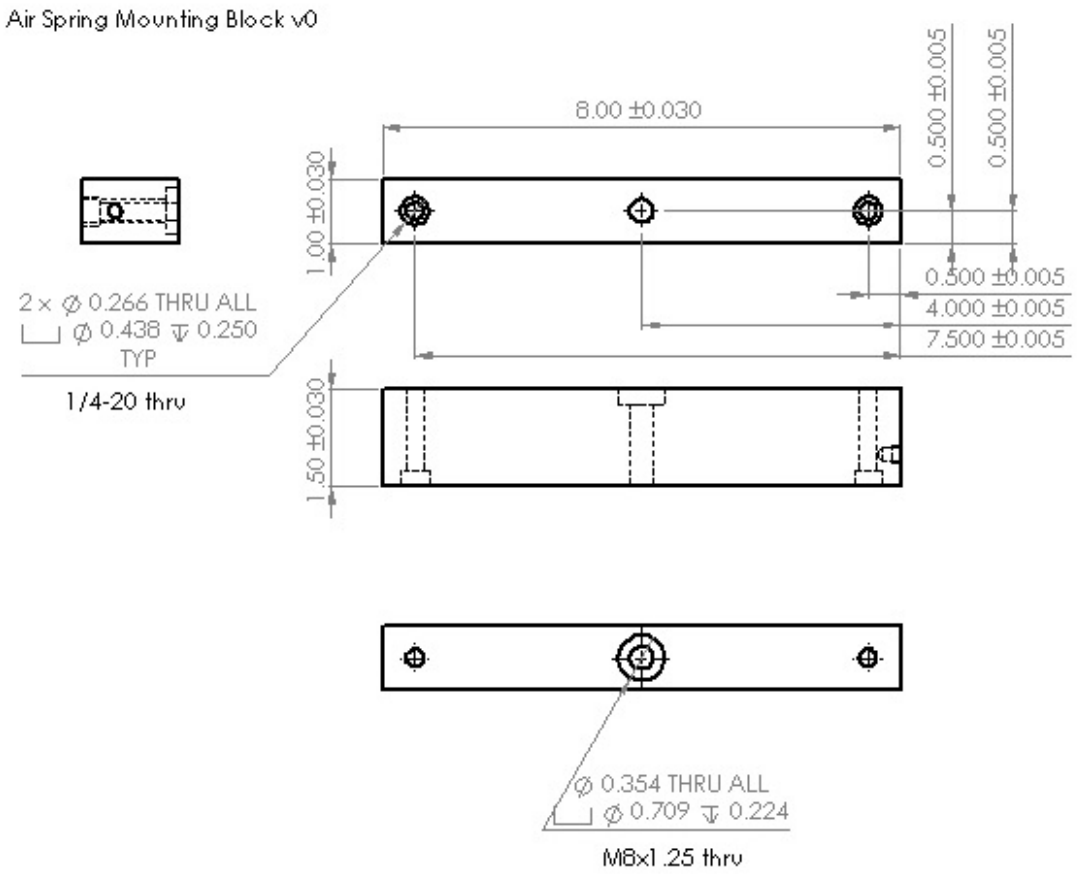

Figure C-17: Block on which Firestone Airstroke is mounted.

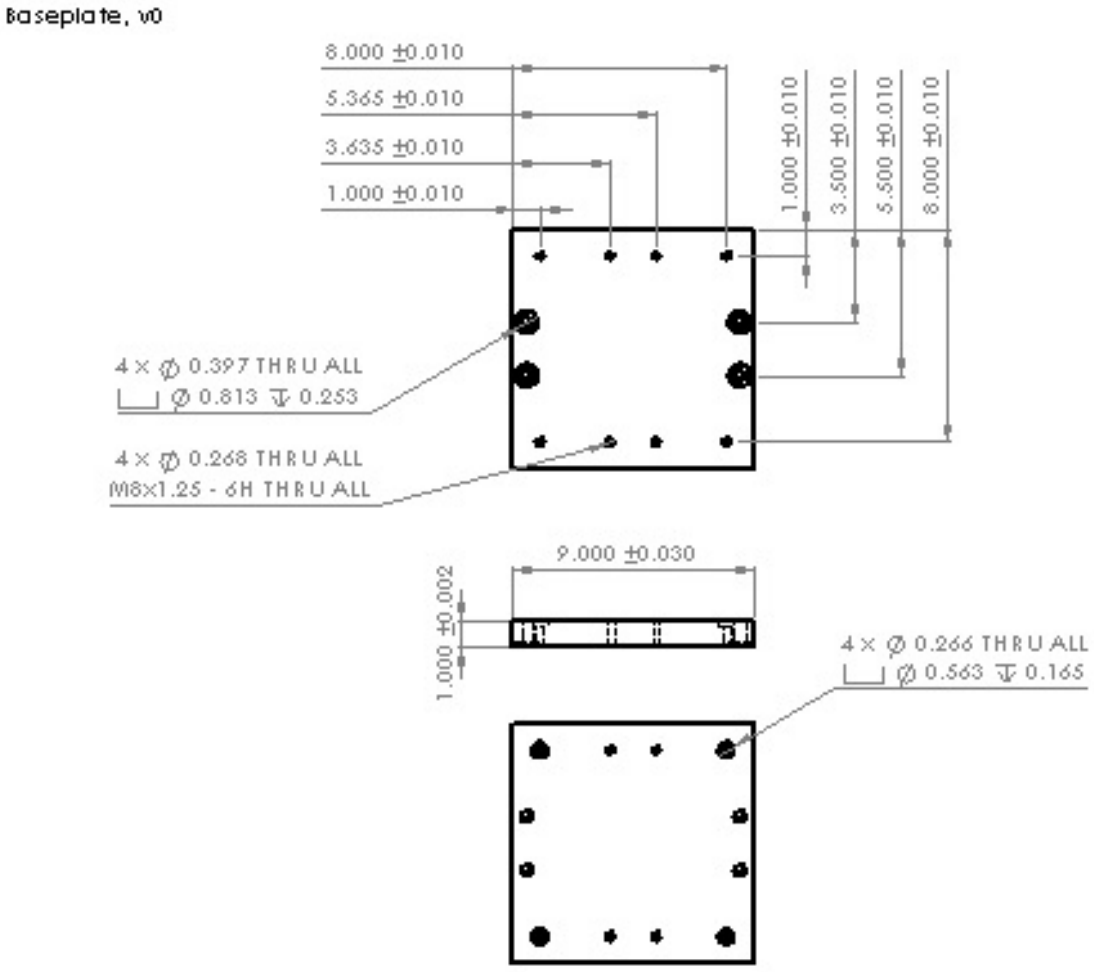

Figure C-18: Blaseplate of O frame structure.

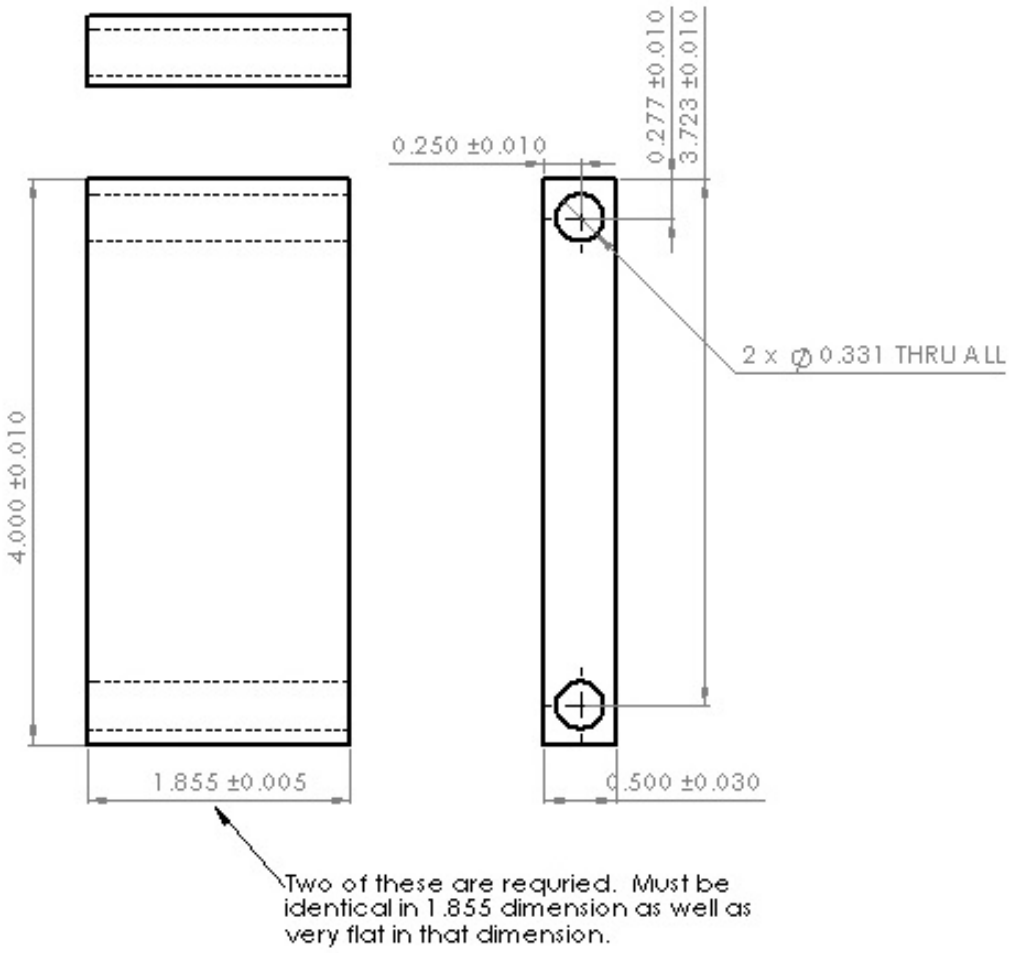

Figure C-19: Structural elements used to mount and position the air bushing pillow block.

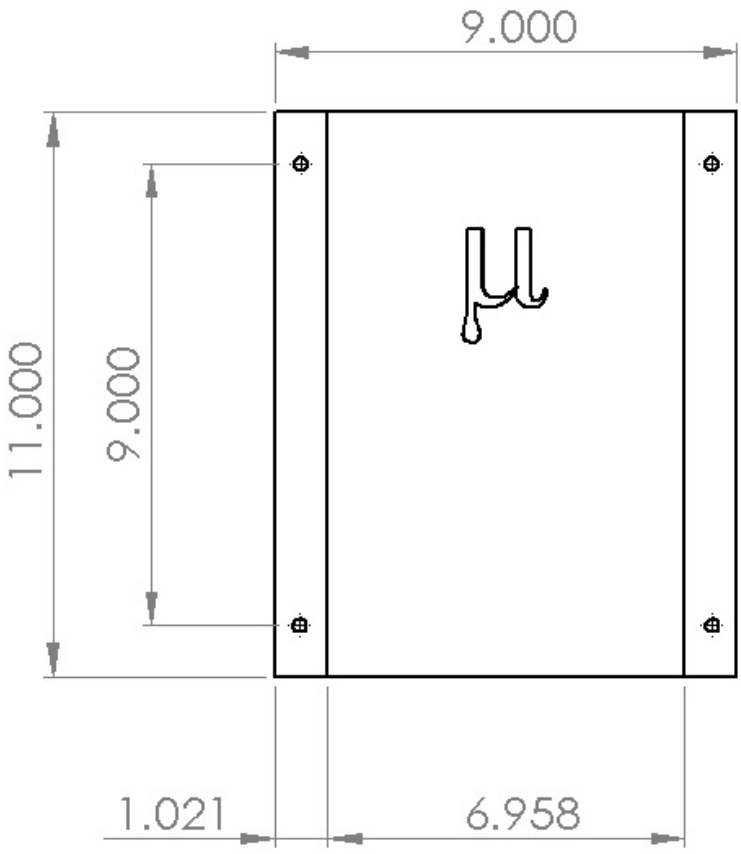

Figure C-20: The template for the HIPS safety shield mold, before bending and thermoforming.

Bibliography

[1] Whitesides, G. M. "The origins and the future of microfluidics." *Nature* 442 (2006) 368-373.

[2] Kang, Shinill. *Micro/Nano Replication: Processes and Applications.* New Jersey: John Wiley & Sons, Inc, 2012.

[3] Regehr, Keil J., et. al. "Biological implications of polydimethylsiloxane-based microfluidic cell culture." *Lab on a Chip* 9 (2009): 2132-2139.

[4] Park, S. H. et. al. "Injection molding micro patterns with high aspect ratio using a polymeric flexible stamper." *eXPRESS Polymer Letters* 5.11 : 950-958.

[5] Heckele M. and W. K. Schomburg. "Review on micro molding of thermoplastic polymers." *Journal of Micromechanics and Microengineering* 14 (2004): R1-R14.

[6] Gilles, Sandra et. al. "UV nanoimprint lithography with rigid polymer molds." *Microelectronic Engineering* 86 (2009): 661-664.

[7] EV Group. "Nanoimprint Lithography Systems." Web. Accessed May 2013.

[8] Jeon, Jessie S. et al. "Hot embossing for fabrication of a microfluidic 3D cell culture platform." Biomedical Microdevices 13.2 (2010): 325-333.

[9] Tsao, Chia-Wen and DeVoe, DonL. "Bonding of thermoplastic polymer microfluidics." *Microfluidics and Nanofluidics* 6.1 (2009): 1-16.

[10] Wang, Qi. "Process window and variation characterization of the micro embossing process." MS thesis. MIT, 2006.

[11] Ames, Nicoli M. et al. "A Thermo-mechanically Coupled Theory for Large Deformations of Amorphous Polymers. Part II: Applications." *International Journal of Plasticity* 25.8 (2009): 1495-1539.

[12] Srivastava, Vikas et al. "A Thermo-mechanically-coupled Large- deformation Theory for Amorphous Polymers in a Temperature Range Which Spans Their Glass Transition." *International Journal of Plasticity* 26.8 (2010) : 1138-1182.

[13] Hale, Melinda. "Development of a Low-Cost, Rapid-Cycle Hot Embossings System for Microscale Parts." MS thesis. MIT, 2009.

[14] Reyda, Caitlin. "Design of a Functional Testing System for Cycle-to-Cycle Process Control of Hot Embossed Microfluidic Devices." Poster session presented at: ASPE Topical Summit Spring 2013; 2013 April 22; Cambridge, MA.

[15] Zarrouati, Nadège. "A precision manipulation system for polymer microdevice production." MS thesis. MIT, 2010.

[16] Henann, David Lee. "A constitutive theory for the mechanical response of amorphous metals at high temperatures spanning the glass transition temperature: application to microscale thermoplastic forming of $Zr_{41.2}Ti_{13.8}Cu_{12.5}Ni_{10}Be_{22.5}$." MS thesis. MIT, 2008.

[17] Hassanin, H., A. Mohammadkhani, and K. Jiang. "Fabrication of hybrid nanostructured arrays using a PDMS/PDMS replication process." *Lab on a Chip* 20 (2012): 4160-4167.

[18] Dirckx, Matthew E. "Demolding of Hot Embossed Polymer Microstructures." PhD thesis. MIT, 2010.

[19] Dirckx, Matthew E. and David E. Hardt. "Analysis and characterization of demolding of hot embossed polymer microstructures." *Journal of Micromechanics and Microengineering* 21.8 (2011): 085024.

[20] Ganesan, Balamurugan. "Process Control for Micro Embossing: Initial Variable Study." MS thesis. MIT, 2004.

[21] Firestone Industrial Products Company. "131: Firestone Airstroke and Airmount Datasheet." Accessed September 2011.

[22] Watlow Electric Manufacturing Company. "ULTRAMIC (TM) 600 Advanced Ceramic Heater." Datasheet. Accessed May 2013.

[23] New Way Air Bearings. "Air Bushing – English: 2.00 Inch Inside Diameter." Datashseet. Accessed September 2011.

[24] Stamprite Machine Company. "The VT-Series Hot Stamp Press." Web. May 2013.

[25] Pelzer, Rainer, et al. "Nanoimprint Lithography – Full Wafer Replication of Nanometer Features."

[26] Ede, James. "Price Request for EVG 520HE Hot Embossing System (ID# 2904) & EVG 520 Wafer Bonder (ID# 2610)." Message to the author. 12 June 2012. E-mail.

[27] Hardt, David et al. "Process Control in Micro-Embossing: A Review." *Innovation in Manufacturing Systems and Technology* 01-2004.

[28] Chou, Stephen Y., Peter R. Krauss, and Preston J. Renstrom. "Imprint Lithography with 25-Nanometer Resolution." *Science* 272 (1996): 85-87.

[29] Ashby, Michael F. *Materials Selection in Mechanical Design.* 3rd ed. Elsevier Butterworth-Heinemann, Oxford: 2005.

[30] Culpepper, Martin. "2.72 Elements of Mechanical Design: Lecture 09: Flexures." *2.72 Course Materials website.* Electronic presentation. May 2013.

[31] Matweb, LLC. "Aluminum 6061-T6; 6061-T651." Web. May 2013.

[32] Jaco Products. "Glastherm HT Insulation." Datasheet. Accessed September 2011.

[33] Wong, Eehern J. "Modeling and Control of Rapid Cure in Polydimethylsiloxane (PDMS) for Microfluidic Device Applications." PhD thesis. MIT, 2010.

[34] Futek Advanced Sensor Technology, Inc. "Futek Model LTH300: Donut/Thru Hold Load Cell." Datasheet. Accessed September 2011.

[35] Omega Engineering. "Precision DC Gaging Transducers for Quality Control or Automation Tooling." Datasheet. Accessed June 2012.

[36] Firestone Industrial Products Company. "Advantages of Airstroke Actuators." Accessed May 2013.

[37] Futek Advanced Sensor Technology, Inc. "Products and Services: Pancake Load Cell." Web. Accessed May 2013.

[38] New Way Air Bearings. "Air Bushings - English - 3.00 Inch ID." Web. Accessed May 2013.

[39] Omega Engineering Inc. "Digital Output LVDT Displacement Transducers." Web. Accessed May 2013.